

DUst Around NEarby Stars. The survey observational results $\star, \star \star$

C. Eiroa¹, J.P. Marshall¹, A. Mora², B. Montesinos³, O. Absil⁴, J. Ch. Augereau⁵, A. Bayo^{6,7}, G. Bryden⁸, W. Danchi⁹, C. del Burgo¹⁰, S. Ertel⁵, M. Fridlund¹¹, A. M. Heras¹¹, A. V. Krivov¹², R. Launhardt⁷, R. Liseau¹³, T. Löhne¹², J. Maldonado¹, G.L. Pilbratt¹¹, A. Roberge⁹, J. Rodmann¹⁴, J. Sanz-Forcada³, E. Solano³, K. Stapelfeldt⁹, P. Thébault¹⁵, S. Wolf¹⁶, D. Ardila¹⁷, M. Arévalo^{3,33}, C. Beichmann¹⁸, V. Faramaz⁵, B.M. González-García¹⁹, R. Gutiérrez³, J. Lebreton⁵, R. Martínez-Arnáiz²⁰, G. Meeus¹, D. Montes²⁰, G. Olofsson²¹, K.Y.L. Su²², G. J. White^{23,24}, D. Barrado^{3,25}, M. Fukagawa²⁶, E. Grün²⁷, I. Kamp²⁸, R. Lorente²⁹, A. Morbidelli³⁰, S. Müller¹², H. Mutschke¹², T. Nakagawa³¹, I. Ribas³², and H. Walker²⁴

(Affiliations can be found after the references)

Received , ; Accepted

ABSTRACT

Context. Debris discs are a consequence of the planet formation process and constitute the fingerprints of planetesimal systems. Their solar system's counterparts are the asteroid and Edgeworth-Kuiper belts.

Aims. The DUNES survey aims at detecting extra-solar analogues to the Edgeworth-Kuiper belt around solar-type stars, putting in this way the solar system into context. The survey allows us to address some questions related to the prevalence and properties of planetesimal systems.

Methods. We used *Herschel*/PACS to observe a sample of nearby FGK stars. Data at 100 and 160 μm were obtained, complemented in some cases with observations at 70 μm , and at 250, 350 and 500 μm using SPIRE. The observing strategy was to integrate as deep as possible at 100 μm to detect the stellar photosphere.

Results. Debris discs have been detected at a fractional luminosity level down to several times that of the Edgeworth-Kuiper belt. The incidence rate of discs around the DUNES stars is increased from a rate of $\sim 12.1\% \pm 5\%$ before *Herschel* to $\sim 20.2\% \pm 2\%$. A significant fraction ($\sim 52\%$) of the discs are resolved, which represents an enormous step ahead from the previously known resolved discs. Some stars are associated with faint far-IR excesses attributed to a new class of cold discs. Although it cannot be excluded that these excesses are produced by coincidental alignment of background galaxies, statistical arguments suggest that at least some of them are true debris discs. Some discs display peculiar SEDs with spectral indexes in the 70–160 μm range steeper than the Rayleigh-Jeans one. An analysis of the debris disc parameters suggests that a decrease might exist of the mean black body radius from the F-type to the K-type stars. In addition, a weak trend is suggested for a correlation of disc sizes and an anticorrelation of disc temperatures with the stellar age.

Key words. stars: circumstellar matter – stars: planetary systems – infrared: stars

1. Introduction

Circumstellar discs are formed around stars as a by-product required by angular momentum conservation. In their earliest phases, stars accrete a significant part of their masses from gas and dust in the discs. Meanwhile, those circumstellar accretion discs evolve from a gas-dominated protoplanetary phase to a gas-poor debris-disc phase where large planetesimals and full-sized planets may have formed, after primordial submicron-sized dust grains settle in the disc midplane and coagulate to form dust aggregates, pebbles, and larger rocky bodies. Most likely this is the formation pathway followed by the currently known exoplanets (close to one thousand) and our own solar system to form. However, it is not known which are the ultimate circumstances and physical conditions that make planet formation possible, and whether planet formation is nearly as universal during disc evolution as is the formation of discs during star

formation. This issue is central to understand the incidence of planetary systems in general, and consequently the formation of Earth-like planets.

In the solar system, the planets together with asteroids, comets, the zodiacal material and the Edgeworth-Kuiper Belt (EKB) are the fingerprints of such dynamical processes. Planet formation resulted in a nearly total depletion of planetesimals inside the orbit of Neptune, with the remarkable exception of the asteroid belt. Leftover planetesimals not incorporated into planets arranged to form the EKB, beyond the orbit of Neptune, dynamically sculpted and excited by the giant planets. Mutual collisions between EKB objects and erosion by interstellar dust grains release dust particles that spread over the EKB region (Jewitt et al. 2009). If the EKB could be observed from afar, it would appear as an extended (~ 50 AU) and very faint ($L_d/L_\odot \sim 10^{-7}$) emission with a temperature of 70–100 K (Backman et al. 1995; Vitense et al. 2010, 2012), with a huge central hole caused by the massive planets (Moro-Martín & Malhotra 2005).

The discovery of IR excesses in main-sequence stars such as Vega, Fomalhaut or β Pic was one of the most significant accomplishments of the IRAS satellite (Aumann et al. 1984). The observed excess was attributed to thermal emission from solid particles around the stars. Optical imaging of β Pic convincingly demonstrated that the dust was located in a flattened

Send offprint requests to: C. Eiroa
e-mail: carlos.eiroa@uam.es

* Herschel is an ESA space observatory with science instruments provided by European-led Principal Investigator consortia and with important participation from NASA.

** Tables are only available in the electronic version of the paper or at the CDS via anonymous ftp to cdsarc.u-strasbg.fr (130.79.128.5) or via http://cdsweb.u-strasbg.fr/cgi-bin/qcat?J/A+A/

circumstellar disc (Smith & Terrile 1984). Since lifetimes of dust grains against radiative/wind removal, Poynting–Robertson drag and collisional disruption are much shorter than the age of the stars, one must conclude that these dust particles are not remnants of the primordial discs, instead they are the result of ongoing processes. Nearly all modelling efforts explain “debris discs” dust production as a result of collisions of larger bodies (Wyatt 2008; Krivov 2010, and references therein). Given that debris discs survive over billions of years, there must be a large reservoir of leftover planetesimals and solid bodies that collide and are intimately related to the dust particles. Furthermore, dust particles respond in different ways to the gravity of planetary perturbers depending on their size distribution and can be used as a tracer of planets (Augereau et al. 2001; Quillen & Thorndike 2002; Moro-Martín et al. 2007; Mustill & Wyatt 2009; Thebault et al. 2012). Consequently, observations of debris discs sheds light onto the processes related to planet and planetesimal formation.

Much observational as well as modelling progress has occurred in the last two decades primarily from infrared (IR) and (sub)-millimetre facilities. The first debris discs were discovered by the InfraRed Astronomical Satellite (IRAS), mainly around A stars due to sensitivity limitations. The Infrared Space Observatory (ISO) extended the study of debris discs and added important information on the age distribution of debris discs (Habing et al. 2001). More recently, *Spitzer* added a wealth of new information in a variety of aspects. For example, the incidence rate was found to be larger for A stars and then it decreased with later spectral types up to M stars (Su et al. 2006; Gautier et al. 2007). An incident rate of $\sim 16\%$ was found around solar-type FGK stars (Trilling et al. 2008), not dependent on the stellar metallicity (Beichman et al. 2006), although a marginal trend might exist, as recently suggested by Maldonado et al. (2012). The presence of exoplanets is not necessarily a sign for a higher incidence of debris discs (Kóspál et al. 2009), although Wyatt et al. (2012) have recently claimed that the debris incidence rate is higher around stars with low mass planets, and there may be trends between some debris discs and planet properties when both simultaneously exist (Maldonado et al. 2012). *Spitzer* also found that typical debris discs around solar-type stars emit much stronger at $70\ \mu\text{m}$ than at $24\ \mu\text{m}$, with the detection rate for hot discs being very low. Spectral energy distributions (SEDs) imply the dust is located at several tens of AU and dust temperatures $\sim 50\text{--}150\ \text{K}$ (Trilling et al. 2008; Moór et al. 2011). However, the distance, dust mass and optical properties are degenerate with the (unknown) particle size distribution.

In spite of its remarkable contribution *Spitzer* suffered from two severe constraints. Firstly, its moderate sensitivity, $L_d/L_\star \sim 10^{-5}$ (Trilling et al. 2008), i.e., about two orders of magnitude above the EKB luminosity, and its wavelength coverage, in practice up to $70\ \mu\text{m}$, limited its ability to detect cold dust. Secondly, its moderate spatial resolution prevented detailed studies of the spatial structure in debris discs since it resolved only a few discs. Significantly higher spatial resolution is required in order to determine the location of the dust and its spatial distribution, which traces rings, warps, cavities, or asymmetries, and which can be used to infer the potential presence of planets (Mouillet et al. 1997; Lagrange et al. 2010). The ESA *Herschel* space telescope (Pilbratt et al. 2010) overcomes these limitations thanks to its larger mirror and instruments PACS (Poglitsch et al. 2010) and SPIRE (Griffin et al. 2010), which allow for a better sensitivity, wavelength coverage and higher spatial resolution.

In this paper we summarize the observational results obtained in the frame of the *Herschel* Open Time Key Programme

DUNES¹, *DUSt* around *NEArby* Stars, (KPOT_ceilroa_1 and SDP_ceilroa_3). This programme aims at detecting EKB analogues around nearby solar-type stars; putting in this manner the solar system into context. The content of this paper addresses the DUNES observational results presented as a whole. Detailed analysis or studies of individual sources or groups of objects are out of the scope of this work. For such more detailed and deeper studies we refer to some already published observational (Liseau et al. 2010; Eiroa et al. 2010; Marshall et al. 2011; Eiroa et al. 2011), and modelling papers (Ertel et al. 2012a; Löhne et al. 2012), as well as to forthcoming ones. The current paper is organized as follows: section 2 describes the scientific rationale and the observing strategy. Section 3 presents the sample of stars. Section 4 describes the *Herschel* PACS and SPIRE observations and data reduction, while the treatment of PACS noise and the results are presented in sections 5 and 6, respectively. The analysis of the data of the non-excess sources with the upper limits of the fractional luminosity of the dust are in Section 7.1. The detected debris discs are presented in Section 7.2, where the background contamination and some general properties and characteristics of the discs are described. Section 8 presents a discussion of disc properties and some stellar parameters. Finally, section 9 contains a summary and our conclusions. In addition, several appendixes give some fundamental parameters of the stars, the method used for the photospheric fits, and a short description of some spurious objects.

2. DUNES Scientific objectives: Survey rationale

The primary scientific objective of DUNES is the identification and characterization of faint exosolar analogues to the solar system EKB in an unbiased sample of nearby solar-type stars. Strictly speaking, the detection of such faint discs is a direct proof of the incidence of planetesimal systems and an indirect one of the presence planets. The survey design allows us to additionally address several fundamental, specific questions that help to evaluate the prevalence and properties of such planetesimal and planetary systems. These are: i) the fraction of solar-type stars with faint, EKB-like discs; ii) the collisional and dynamical evolution of EKB analogues; iii) the dust properties and size distribution; and iv) the incidence of EKB-like discs versus the presence of planets.

According to the recent EKB model of Vitense et al. (2012), the predicted infrared excess peaks at $\sim 50\ \mu\text{m}$ and the flux levels in the PACS bands would be between 0.1 and 0.4 mJy. This flux is about an order of magnitude lower than the expected photospheric fluxes from nearby solar-type stars (see appendix C), and few times lower than the predicted pre-launch sensitivity of PACS (PACS observer’s manual, version 1.3, 04/July/2007). Therefore, the challenge of detecting a faint infrared excess, which could be considered as an exo-EKB analogue, is the detection of a faint far-IR signal from a debris disc on top of a weak photospheric signal which is few times the expected measurement uncertainties.

The observing strategy is also modulated by the choice of the optimal wavelength. The equilibrium temperature of a dust grain depends on the stellar luminosity, the radial distance to the star, and dust properties (size, chemical composition, mineralogy). For distances of $\sim 30\text{--}100\ \text{AU}$, grains of about $10\ \mu\text{m}$ in size have temperatures in the range $\sim 30\text{--}50\ \text{K}$ (Krivov et al. 2008). At these temperatures, the bulk of the thermal re-emission is radiated in the far-IR covered by the PACS photometric bands

¹ <http://www.mpia-hd.mpg.de/DUNES/>

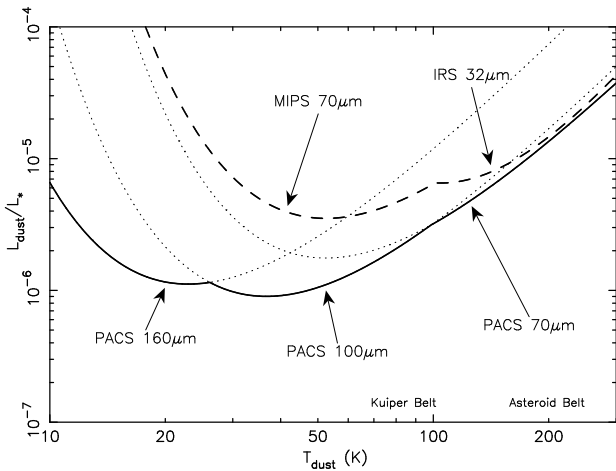


Fig. 1. Detection limits for a G2V star at 10 pc for the *Herschel* 70, 100, and 160 μm bands compared to the *Spitzer* instruments MIPS at 70 μm and IRS at 32 μm .

centered at 70, 100, and 160 μm . Figure 1 highlights the unique *Herschel* PACS discovery space compared to *Spitzer* MIPS and IRS. The limits in Figure 1 are calculated assuming PACS 1σ accuracies of 1.5, 1.5, and 3.5 mJy at 70, 100, and 160 μm , respectively. A systematic uncertainty of 5% is also included for calibration uncertainty. Note that these accuracies are larger than the typical uncertainties found in this survey (e.g. Table 12), and that the systematic uncertainty is larger than that reported in the PACS technical note PICC-ME-TN-037². *Spitzer*/MIPS limits are based on an assumed photometry accuracy of 3 mJy and a 10% systematic contribution (e.g. Bryden et al. 2009). *Spitzer*/IRS is limited to a 2% uncertainty at 32 μm (Lawler et al. 2009). The assumed photospheric uncertainty for both PACS and MIPS is 2%. The plot shows in particular that PACS 100 μm provides the most suitable range to detect very faint discs for dust temperatures in the range from ~ 20 to ~ 100 K. Further, with a detection limit of L_d/L_\star few times 10^{-7} , PACS 100 μm has the ability to reveal dust discs with emission levels close to the EKB. We note that although the PACS 70 μm band has a sensitivity similar to PACS 100 μm for EKB temperatures around 100 K, and is more competitive in terms of background confusion and stellar photospheric detection, 100 μm provides a better contrast ratio between the emission of cold dust and the stellar photosphere, and is in fact much more sensitive than PACS 70 μm for probing very faint, cold discs.

Given the above considerations concerning flux levels from the EKB analogues and the stars together with the optimal wavelength, the choice to fulfil the DUNES objectives was to integrate as deep as needed to achieve the estimated photospheric flux levels at 100 μm .

3. The stellar sample

The preliminary stellar sample was chosen from the *Hipparcos* catalogue (ESA 1997) following the sole criterion of selecting main-sequence, luminosity classes V-IV/V, stars closer than 25 pc without any further bias concerning any property of the stars. Since the *Herschel* observations were designed to detect the photosphere, the only restriction to build the final sample was that the stars could effectively be detected by PACS at 100 μm with a $S/N \geq 5$, i.e., the expected 100 μm photospheric flux should

Table 1. Summary of spectral types in the DUNES sample and the shared sources observed by DEBRIS.

Sample	F stars	G stars	K stars	Total
Solar-type stars observed by				
DUNES (the DUNES sample)	27	52	54	133
20 pc DUNES subsample	20	50	54	124
Shared solar-type stars				
observed by Debris	51	24	8	83
Shared 20 pc subsample	32	16	8	56

be significantly higher than the expected background as estimated by the *Herschel* HSPOT tool at that wavelength. Taking into account the total observing time finally allocated for the DUNES survey (140 hours) as well as the complementarity with the *Herschel* OTKP DEBRIS (Matthews et al. 2010), the stellar sample for this study was reduced to main-sequence FGK solar-type stars located at distances smaller than 20 pc. In addition, from the original sample we retained FGK stars between 20 and 25 pc hosting exoplanets (3 stars, 1 F-type and 2 G-type, at the time of the proposal writing) and previously known debris discs, mainly from the *Spitzer* space telescope (6 stars, all F-type). Thus, the final sample of stars directly observed by DUNES, formally called the DUNES sample in this paper, is formed by 133 stars, 27 out of which are F-type, 52 G-type, and 54 K-type stars. The 20 pc subsample is formed by 124 stars - 20 F-type, 50 G-type and 54 K-type. Table 1 summarizes the spectral type distribution of the samples.

The OTKP DEBRIS project was defined as a volume limited study of A through M stars selected from the “UNS” survey (Phillips et al. 2010), observing each star to an uniform depth, i.e., DEBRIS is a flux-limited survey. In order to optimize the results according to the DUNES and DEBRIS scientific goals, the complementarity of both surveys was achieved by dividing the common stars of both original samples considering if the stellar photosphere could be detected with the DEBRIS uniform integration time. Those stars were assigned to be observed by DEBRIS. In that way, the DUNES observational objective of detecting the stellar photosphere was satisfied. The few A-type and M-type stars common in both surveys were also assigned to DEBRIS.

The net result of this exercise was that 106 stars observed by DEBRIS satisfy the DUNES photospheric detection condition and are, therefore, shared targets. Specifically, this sample comprises 83 FGK stars - 51 F-type, 24 G-type and 8 K-type (the rest are A and M stars). Since the assignment to one of the teams was made on the basis of both DUNES and DEBRIS original samples, the number of shared targets located closer than 20 pc, i.e., the revised DUNES distance, are less: 56 FGK - 32 F-type, 16 G-type, and 8 K-type stars (see Table 1). Considering *Hipparcos* completeness, the total sample - DUNES stars plus the shared stars observed by DEBRIS - should be fairly complete (with the constraint that the photosphere is detected with a $S/N \geq 5$ at 100 μm) up to the distance of 20 pc for the F and G stars, while it is most likely incomplete for distances larger than around 15 pc for the K-type stars, particularly for the latest K spectral types. We point out that because of the imposed condition of a photospheric detection over the background with $S/N > 5$ the number of “rejected sources” sources according to the *Hipparcos* catalogue are 10 F-type, 43 G-type, and 213 K-type stars.

Table 2 provides some basic information on the 133 stars in the DUNES sample. Columns 1 and 2 give *Hipparcos* and HD

² Technical note in <http://herschel.esac.esa.int>

Table 2. The DUNES stellar sample. Columns correspond to the following: *Hipparcos* and HD numbers as well as usual stars' names; spectral types and ranges (see text); equatorial and galactic coordinates; parallaxes with errors and stars' distances. Only the first 5 lines of the table are presented here. The full version is available as online material.

HIP	HD	Name	SpT	SpT range	ICRS (2000)	Galactic	π (mas)	d(pc)
171	224930	HR 9088	G3V	G2V - G5V	00 02 10.156 +27 04 56.13	109.6056 -34.5113	82.17± 2.23	12.17
544	166	V439 And	K0V	G8V - K0V	00 06 36.785 +29 01 17.40	111.2636 -32.8326	73.15± 0.56	13.67
910	693	6 Cet	F5V	F5V - F8V	00 11 15.858 -15 28 04.73	082.2269 -75.0650	53.34± 0.64	18.75
2941	3443	HR 159	K1V+...	G7V - G8V	00 37 20.720 -24 46 02.18	068.8453 -86.0493	64.93± 1.85	15.40
3093	3651	54 Psc	K0V	K0V - K2V	00 39 21.806 +21 15 01.71	119.1726 -41.5331	90.42± 0.32	11.06

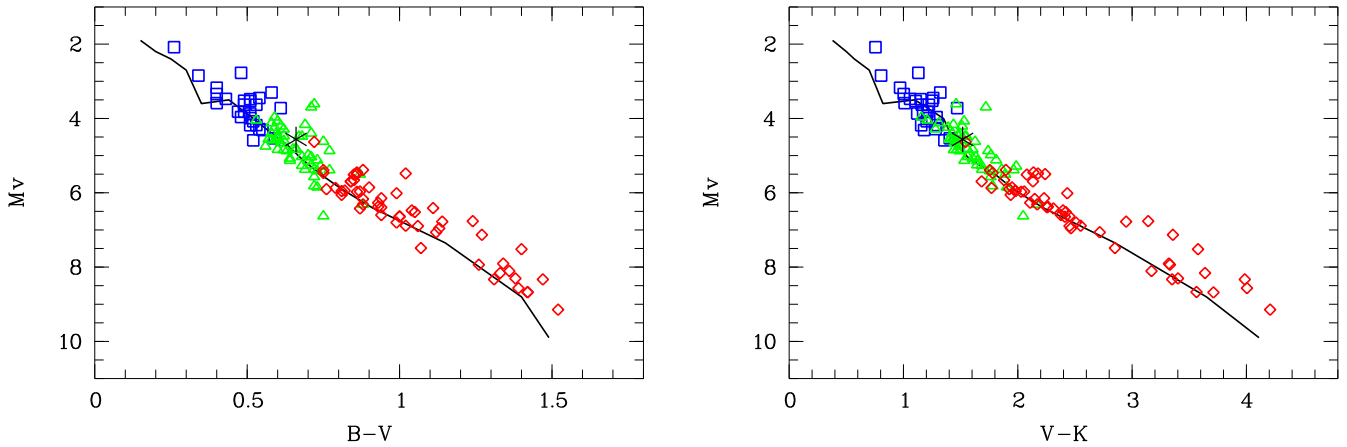


Fig. 2. Colour-absolute magnitude diagrams of the DUNES sources. Spectral types as in Table 1 are distinguished by symbols: blue squares (F-type), green triangles (G-type) and red diamonds (K-type). The solid line in both diagrams represents the main-sequence while the star symbol indicates the position of the Sun (Cox 2000).

Table 3. Photometric magnitudes and fluxes of the DUNES stars. Only the first 5 lines with the optical (Johnson and Strömgren) and 2MASS photometry are shown here (see appendixes B and C). The full version of the table including further near-IR data, AKARI, WISE, IRAS and *Spitzer* MIPS is available as online material.

HIP	V	B - V	V - I	b - y	m_1	c_1	J	H	K_s	Q
171	5.80	0.69	0.82	0.432	0.184	0.218	4.702±0.214	4.179± 0.198	4.068± 0.236	CCD
544	6.07	0.75	0.80	0.460	0.290	0.311	4.733±0.019	4.629± 0.144	4.314± 0.042	EBE
910	4.89	0.49	0.59	0.328	0.130	0.405	4.153±0.268	3.800± 0.208	3.821± 0.218	DCD
2941	5.57	0.72	0.78	0.435	0.254	0.287	4.437±0.266	3.976± 0.224	4.027± 0.210	DDC
3093	5.88	0.85	0.83	0.507	0.384	0.335	4.549±0.206	4.064± 0.240	3.999± 0.036	CDE

Table 4. Fundamental stellar parameters and some properties of the DUNES sources (see appendix B). Only the first 5 lines are shown. The full version of the table is available as online material.

HIP	SpT	T_{eff} (K)	$\log g$ (cm/s^2)	[Fe/H] (dex)	$v \sin i$ (km/s)	Lbol (L_{\odot})	Lx/Lbol (log)	AgeX (Gyr)	$\log R'_{\text{HK}}$	Age(Ca II) (Gyr)
171	G3V	5681	4.86	-0.52	1.8	0.614	-5.9	3.12	-4.851	3.96
544	K0V	5577	4.58	0.12	3.4	0.616	-4.4	0.32	-4.328	0.17
910	F5V	6160	4.01	-0.38	3.8	3.151	-7.6	12.53	-4.788	3.04
2941	K1V+...	5509	4.23	-0.14	1.6	1.258			-4.903	4.83
3093	K0V	5204	4.45	0.16	1.15	0.529	-6.0	4.53	-4.991	6.43

numbers, respectively, while column 3 gives the stars' names as provided by SIMBAD. *Hipparcos* spectral types are given in column 4; in order to check the consistency of these spectral types we have explored VIZIER using the DUNES discovery tool³ (Appendix A). Results of this exploration are summarized in column 5 which gives the spectral type range of each star taken into account SIMBAD, Gray et al. (2003, 2006), Wright et al.

(2003) and the compilation made by Skiff (2009). Typical spectral type range is 2-3 subtypes. Columns 6 and 7 give equatorial and galactic coordinates, respectively. Finally, columns 8 and 9 give parallaxes with errors and distances, respectively. These two latter columns are taken from the recent compilation given by van Leeuwen (2007, 2008). Parallax errors are typically less than 1 mas, although there are few stars with errors larger than 2 mas; those stars are either spectroscopic binaries or are listed in the Catalogue of the Components of Double and Multiple Stars

³ <http://sdc.cab.inta-csic.es/dunes/>

(CCDM) (Dommanget & Nys 2002) as orbit/astrometric binaries. There are 10 stars in Table 1 with distances between 20 and 25 pc. Those are the previously mentioned stars with known exoplanets (HIP 3497, HIP 25110 and HIP 109378), and with identified *Spitzer* debris discs (HIP 14954, HIP 51502, HIP 72603, HIP 73100, HIP 103389 and HIP 114948). In addition, the distance to HIP 36439 is 20.24 pc ($\pi = 49.41$ mas) after the revised *Hipparcos* catalogue (van Leeuwen 2008) but 19.90 pc ($\pi = 50.25$ mas) after the original one (ESA 1997). We also note that the distance to HIP 73100 is 25.11 pc ($\pi = 39.83$ mas) after van Leeuwen (2008), but 24.84 pc ($\pi = 40.25$ mas) after ESA (1997).

Tables 3 (a, b, c and d) give the optical, near-IR, AKARI, WISE, IRAS and *Spitzer* MIPS magnitudes and fluxes of the DUNES stars, while Table 4 gives various stellar parameters. Appendix B gives some details on how the stellar properties were collected. Figure 2 shows the $(B - V, M_V)$ and $(V - K, M_V)$ colour-magnitude diagrams of the sources where one can see how they spread across the stellar main-sequence. The K-type star located within the G-type locus is HIP 2941. This is likely a misclassification of *Hipparcos*; in fact, the range of spectral types in Skiff (2009) indicates an earlier type, G5V - G9V. This is also supported by the high effective temperature, $T_{\text{eff}} \sim 5500$ K (Table 4), too high for a K1 star. The main stellar parameters (T_{eff} , $\log g$ and $[\text{Fe}/\text{H}]$) were used to compute a set of synthetic spectra from the PHOENIX code for GAIA (Brott & Hauschildt 2005), which were later normalized to the observed SEDs of the stars in order to estimate the photospheric fluxes at the *Herschel* bands. The whole procedure is described in detail in Appendix C.

4. Herschel observations and data reduction

4.1. PACS observations

PACS scan map observations of all 133 DUNES targets (comprising 130 individual fields, due to close binaries allowing doubling up of sources in the cases of HIP 71382/4, HIP 71681/3 and HIP 104214/7) were taken with the 100/160 channel combination. Additional 70/160 observations were carried out for 47 stars, some of them with a *Spitzer* MIPS 70 μm excess. Following the recommended parameters laid out in the scan map release note⁴ each scan map consisted of 10 legs of 3' length, with a 4'' separation between legs, scanning at the medium slew speed (20'' per second). Each target was observed at two array orientation angles (70° and 110°) to improve noise suppression and to assist in the removal of low frequency ($1/f$) noise, instrumental artifacts and glitches from the images. A summary of the PACS observations can be found in Table 5 where the PACS bands, the observation identification number of each scan, and the on-source integration time are given.

4.2. SPIRE observations

SPIRE small map observations were taken of 20 DUNES targets selected because they were known as excess stars or as follow-up to the results of the PACS observations. Each SPIRE observation was composed of either two or five repeats (equivalent on-source time of either 74 or 185 s) of the small scan map mode⁵, producing a fully sampled map covering a region 4' around the target. A

Table 5. Summary of all DUNES PACS observations, including the 100/160 and 70/160 channel combinations. The Obs Ids of both cross-scans (columns 3rd and 4th) and on-source integration time are given. Only the first 5 lines of the table are presented here; the full version is available as online material.

HIP	PACS	Scan	X-Scan	On-source time [s]
171	100/160	1342212800	1342212801	900
544	100/160	1342213512	1342213513	1440
910	100/160	1342199875	1342199876	360
2941	100/160	1342212844	1342212845	540
3093	70/160	1342213242	1342213243	180

Table 6. Summary of DUNES SPIRE observations. Obs Ids and observing time are given.

HIP	Obs Id	Time [s]
544	1342213493	74
7978	1342195666	185
13402	1342213481	74
15371	1342198448	185
17439	1342214553	74
22263	1342203629	185
32480	1342204066	185
40843	1342219959	74
51502	1342214703	74
72603	1342213475	74
83389	1342198192	185
84862	1342203593	185
85235	1342213451	74
85295	1342203588	185
92043	1342204948	185
101997	1342206205	185
105312	1342209303	185
106696	1342206206	185
107649	1342209300	185
108870	1342206207	185

summary of the SPIRE observations, observation identification and on-source integration time, is presented in Table 6.

4.3. Data reduction

The PACS and SPIRE observations were reduced using the Herschel Interactive Processing Environment, HIPE (Ott 2010), user release version 7.2, PACS calibration version 32 and SPIRE calibration version 8.1. The individual PACS scans were processed with a high pass filter to remove background structure, using high pass filter radii of 15 frames at 70 μm , 20 frames at 100 μm and 25 frames at 160 μm , suppressing structure larger than 62'', 82'' and 102'' in the final images, respectively. For the filtering process, regions of the map where the pixel brightness exceeded a threshold defined as twice the standard deviation of the non-zero flux elements in the map were masked from inclusion in the high pass filter calculation. Deglitching was carried out using the second level spatial deglitching task, following issues with the clipping of the cores of bright sources using the MMT deglitching method. The two individual PACS scans were mosaicked to reduce sky noise and suppress $1/f$ stripping effects from the scanning. Final image scales were 1'' per pixel at 70 and 100 μm and 2'' per pixel at 160 μm compared to native instrument pixel sizes of 3''.2 and 6''.4. For the SPIRE observations, the small maps were created using the standard pipeline routine in HIPE, using the naive mapper option. Image scales of 6'', 10''

⁴ see: PICC-ME-TN-036 for details.

⁵ see: http://herschel.esac.esa.int/Docs/SPIRE/html/spire_om.pdf for details.

and $14''$ per pixel were used at $250 \mu\text{m}$, $350 \mu\text{m}$ and $500 \mu\text{m}$, respectively.

5. Noise analysis of the DUNES PACS images

The DUNES sample is mostly composed of faint targets in the far-IR. Their fluxes are negligible compared to the telescope thermal emission, which is the main contributor in the form of a large background. Confusion noise is also a concern for some very deep observations, particularly for the $160 \mu\text{m}$ band. The optimum S/N ratio is affected by the choice of the aperture to estimate the source flux and the background. Poisson statistics describe the energy collected from both noise sources: thermal emission and confusion.

The map noise properties can be studied using two different metrics: i) σ_{pix} is the dispersion of the background flux measured on regions sufficiently large to avoid small number statistics, and sufficiently small to avoid the effects of large scale sky inhomogeneities, e.g. cirrus. σ_{pix} is best estimated taking the median value of several such areas in the image. ii) σ_{sky} is the standard deviation of the flux collected by several apertures placed in clear areas in the central portion of the image.

In an ideal scenario with purely random high Poisson noise, both parameters would be related by:

$$\sigma_{\text{sky}} = \sigma_{\text{pix}} \alpha_{\text{corr}} \sqrt{N_{\text{pix}}^{\text{circ}}} \quad (1)$$

where $N_{\text{pix}}^{\text{circ}}$ is the total number of pixels in a circular aperture and α_{corr} is the noise correlation factor. However, the real far-IR sky is far from homogeneous, specially for wavelengths around $160 \mu\text{m}$. In addition, the reduction procedure is not perfect and some residual artificial structure appears superimposed. This ‘‘corrugated’’ noise usually makes σ_{sky} be larger than the expected value from Eq. 1.

Noise correlation is a feature of PACS scan maps that appears because the signal in a given output pixel partially depends on the values recorded in the neighborhood. Correlations appear due to three main reasons. First, the scan procedure entangles the output pixel counts via the signal recorded by the discrete bolometers at a given time. Second, the output maps have pixels much smaller than the real pixel size of the bolometers, which is done with the aim of providing better spatial resolution. Third, the $1/f$ noise introduced by small instabilities in the array temperature and electronics.

5.1. Signal to noise ratio and optimal aperture

Aperture photometry estimates the flux of a source integrating in a circle centered on it and containing a significant fraction of the flux. The flux is given by:

$$\text{Signal} = F_{\star} \text{EEF}(r) \quad (2)$$

where F_{\star} is the flux of the point source in the circle with radius r , and $\text{EEF}(r)$ is the enclosed energy fraction in the circular aperture. The radius is chosen to maximize the signal to noise ratio. The noise has two main contributions. The uncertainty in the flux inside the aperture, Noise_{\star} , and the uncertainty in the background, $\text{Noise}_{\text{back}}$. There are two ways to estimate the noise, based on the metrics σ_{pix} and σ_{sky} .

In terms of σ_{pix} , the aperture noise is given by:

$$\text{Noise}_{\star} = \sigma_{\text{pix}} \alpha_{\text{corr}} \sqrt{N_{\text{pix}}^{\text{circ}}} = \sigma_{\text{pix}} \alpha_{\text{corr}} \sqrt{\pi} r_{\text{pix}} \quad (3)$$

Table 7. Gaussian noise propagation in the absence of noise correlation. The RMS dispersion of the sky flux σ_{sky} in different windows is consistent with propagating the single pixel uncertainty σ_{pix} according to the window size in pixels N_{pix} .

Box size (pix)	σ_{pix}	σ_{sky}	$\sigma_{\text{pix}} \sqrt{N_{\text{pix}}}$
7	100	610	698
15	101	1310	1520
22	100	2290	2200

The background flux is typically determined using an annulus of inner r_i and r_o outer radii (pixel units). The flux coming from the point source at the location of the annulus due to the large extension of the PSF is assumed negligible compared to the noise, because the DUNES sources are typically faint. The background noise contribution can be estimated as:

$$\text{Noise}_{\text{back}} = \sigma_{\text{pix}} \alpha_{\text{corr}} N_{\text{pix}}^{\text{circ}} / \sqrt{N_{\text{pix}}^{\text{annulus}}} = \sigma_{\text{pix}} \alpha_{\text{corr}} \sqrt{\pi} r_{\text{pix}}^2 / \sqrt{r_o^2 - r_i^2} \quad (4)$$

The total noise is the quadratic sum of both the aperture and background contributions:

$$\text{Noise} = \sqrt{\text{Noise}_{\star}^2 + \text{Noise}_{\text{back}}^2} \quad (5)$$

Alternatively, in terms of σ_{sky} the sky background and the associated uncertainty can be estimated measuring the total flux in n_{sky} apertures with the same size used for the source. The apertures are located in clean fields, in order to avoid biasing the statistics, and as close as possible to the source, in order to get uniform exposure times. In this case, the noise is given by:

$$\text{Noise} = \sigma_{\text{sky}} \sqrt{1 + \frac{1}{n_{\text{sky}}}} \quad (6)$$

The $1/n_{\text{sky}}$ factor comes from the finite number of apertures used and quickly goes to zero. This approach has the advantage that no correlated noise factor is required for sufficiently large apertures. However, it provides a conservative estimate if the background is variable, due to sky inhomogeneities or $1/f$ noise filtering residuals, as it is the case for the DUNES observations.

In order to validate the consistency of both noise estimation procedures we have carried out several tests using both survey reduced images and synthetic noise frames. The theoretical relationship between σ_{sky} and σ_{pix} in Eq. 1 has been tested for small to moderately large box sizes, which is a way to verify the error propagation scheme under large Poisson noise conditions. For the synthetic noise frames, we have built an image of 200×200 pixels with an arbitrarily large sky level of 10000 photons and gaussian noise of 100 photons, since the Poisson distribution can be well approximated by a gaussian for high fluxes. This image simulates the noise introduced by the telescope emission, which is the dominant factor for DUNES - faint sources and broad band photometry. Multiple regions (25+) have been selected in the image with square box sizes of 7, 15 and 22 pixels per side. σ_{pix} and σ_{sky} have been estimated for these boxes, and the latter values have been compared to $\sigma_{\text{pix}} \sqrt{N_{\text{pix}}}$ (Table 7). The differences are below 15%, consistent with Poisson propagation noise. It has thus been verified that noise propagation works well for images not affected by correlated noise. In addition, small boxes can be used to provide reliable estimates.

Further, a comparison of both methods by the HSC team (B. Altieri, private communication) showed that the multiple apertures σ_{sky} method provides in general larger uncertainties than the error propagation of the σ_{pix} metrics. The values are typically consistent and smaller than a factor 2. The selection of one of them is subjective. Given that the aim of DUNES is the detection of very faint excesses, we have followed the conservative approach of taking the largest noise value for each individual DUNES source to assess the presence of an infrared excess.

Finally, when the sky value has been determined with high precision (using many apertures to improve the statistics), the signal to noise ratio can be estimated as:

$$\text{SNR}(r_{\text{pix}}) = \frac{F_{\star} \text{EEF}(r_{\text{pix}})}{\text{Noise}} \quad (7)$$

This equation shows that there is an optimum extraction radius providing the highest SNR possible. If it is too small, little signal will be collected, while if it is too large, the noise introduced by the aperture is considerable. Optimum values estimated by the *Herschel* team⁶ are 4", 5" and 7"-8" for 70, 100 and 160 μm , respectively. We have carried out the same exercise using a number of DUNES clean fields and the σ_{pix} metrics (σ_{sky} is comparatively more affected by sky inhomogeneities) and found essentially the same results.

5.2. Correlated noise

As pointed out before, the PACS scan map observations intrinsically suffer from correlated noise. Theoretical correlated noise factors α_{corr} were derived by Fruchter & Hook (2002) for the Drizzle algorithm, which combines multiple undersampled images (in terms of the Nyquist criterion). They showed that the correlated noise depends on the ratio r between the linear pixel fraction (the ratio between the drop and the natural pixel box sizes) and the linear output pixel scale factor (the ratio between the output and the natural pixel box sizes). This procedure, used by default in the *Herschel* PACS reduction pipeline, produces output images with typical smaller output pixel sizes, better spatial resolution than individual frames, but significant correlated noise.

The PACS calibration team has made extensive tests on the correlated noise measuring the noise properties of fields surrounding bright stars (see the mentioned technical note P1CC-ME-TN-037) and have estimated α_{corr} as a function of the output pixel size. The value for output pixel sizes of 1" (the size of our 100 μm reduced images) is $\alpha_{\text{corr}} = 2.322$, while for 2" (160 μm images) $\alpha_{\text{corr}} = 2.656$. However, these estimates are too optimistic because no correlated noise is assumed for output pixels with a size equal to the natural ones.

We have analysed the effect of the correlated noise on images with natural pixel sizes as it has a clear effect on the α_{corr} factor we have to apply for our reduced images. The approach we have made is the following.

As a first step, we have tried to validate the P1CC-ME-TN-037 predictions evaluating the noise properties of the PACS images of the DUNES stars HIP 103389, HIP107350 and HIP 114948. Reduced observations with both small (1"/pix, 70 and 100 μm and 2"/pix, 160 μm) and natural (3.2"/pix, 70 and 100 μm and 6.4"/pix, 160 μm) pixel sizes have been considered. Square box sizes of 22" and 44" have been used for 100 and 160 μm , respectively. These values, larger than the optimal aperture sizes, were used to prevent small number statistics for the

natural pixel size frames. Table 8 summarises the results, from which several conclusions can be drawn. i) The correlated noise effect can clearly be noticed comparing the $\sigma_{\text{pix}} \sqrt{N_{\text{pix}}}$ values, which are much smaller for the small size output pixels. This means that there is indeed significant correlated noise in the finer sampled output frames. ii) Similar statistical flux uncertainties $\Delta F_{\star} = \alpha_{\text{corr}} \sigma_{\text{pix}} \sqrt{N_{\text{pix}}}$ are obtained for aperture photometry if the correlation factors in P1CC-ME-TN-037 are used. The agreement is better for the blue detectors. This demonstrates that the P1CC-ME-TN-037 α_{corr} formulae provide good estimates of the differential increase in correlated noise between natural size and smaller output pixels. However, the amount of correlated noise for natural size output pixels is unknown. iii) The sky value, when averaged over a large area, is not affected by correlated noise. It can, nevertheless, be affected by large scale sky inhomogeneities due to residual $1/f$ noise or confusion (partially resolved background sources).

As a second step, the full correlated noise factors for small and natural pixel sizes have been estimated. Additional tests were carried out reducing the HIP 544 and HIP 99240 images with different output pixel sizes. These objects are in fields particularly clean of additional sources, which is critical to really estimate correlated noise factors and not confusion noise. The output pixel sizes range between the standard 1" and 2" for 100 and 160 μm , and twice the natural pixel size, respectively. The pixel fraction was always set to the default value of 1.0. For each image and pixel size, σ_{pix} was estimated on sky constant size boxes of $\approx 25''$ and $50''$ widths for the 100 and 160 μm channels, respectively. The results are presented in Table 9. It shows the median value σ_{pix} of each frame estimated as the median of several measurements ($\sim 6-8$) in boxes placed next to the central object, to minimise sky coverage border effects. Correlated noise factors in the table have been computed assuming no correlated noise for the images with output pixels twice the natural size ($r = 0.50$). This assumption is not strictly correct. However, larger output pixel sizes could not be studied because the box sizes required would have been too large compared to the high density coverage portion in the DUNES small scan maps. In addition, very large output pixel sizes make rejection of background sources increasingly difficult. We believe the small amount of correlated noise not considered for the very large pixels compensates with the additional background noise included in the box averages.

The correlated noise factors in Table 9 are roughly consistent with the predictions by Fruchter & Hook (2002). In particular, the values obtained for the fine pixel maps (1"/pix and 2"/pix for 100 and 160 μm) bracket the theoretical expectations. Taking into account all the tests carried out, the correlated noise factor that has been used for the analysis of the whole DUNES sample and all wavelengths is: $\alpha_{\text{corr,DUNES}} = 3.7$. It is the same for all 70, 100 and 160 μm because the ratio between natural to standard output pixel sizes is always 3.2.

6. Results

6.1. PACS

6.1.1. PACS Photometry

PACS photometry of the sources identified as the far-IR counterparts of the optical stars was carried out using two different methods. The first method consisted in estimating PACS fluxes primarily using circular aperture photometry with the optimal radii 4", 5", and 8" at 70 μm , 100 μm and 160 μm , respectively.

⁶ Technical Note P1CC-ME-TN-037 in <http://herschel.esac.esa.int>

Table 8. Image noise properties for small and natural output pixel sizes. σ_{sky} and σ_{pix} have been estimated for several fields using clean square areas of 22'' and 44'' sizes at 100 and 160 μm , respectively. The number after the stellar *Hipparcos* catalogue number is the wavelength: 70, 100 and 160 μm . Two different 160 μm images were available for HIP 103389. The correlated noise is clearly revealed by σ_{sky} being always larger than $\sigma_{\text{pix}} \sqrt{N_{\text{pix}}}$ for the small output pixels. The correlated factors included in PIC-ME-TN-037 have been used to compute the error ratios $\Delta F_{\star}^{\text{natural}} / \Delta F_{\star}^{\text{small}} = \alpha_{\text{corr}}^{\text{natural}} \sigma_{\text{pix}}^{\text{natural}} \sqrt{N_{\text{pix}}^{\text{natural}}} / \alpha_{\text{corr}}^{\text{small}} \sigma_{\text{pix}}^{\text{small}} \sqrt{N_{\text{pix}}^{\text{small}}}$. The ratios are always close to 1.0, which means that the factors in PIC-ME-TN-037 account for the difference in correlated noise between the natural and standard output pixel sizes. See text and Table 9 for more details on the correlated noise factor for natural output pixel sizes.

Unit: Jy Image	Small pix		Natural pix		Error Ratio $\Delta F_{\star}^{\text{natural}} / \Delta F_{\star}^{\text{small}}$
	σ_{sky}	$\sigma_{\text{pix}} \sqrt{N_{\text{pix}}}$	σ_{sky}	$\sigma_{\text{pix}} \sqrt{N_{\text{pix}}}$	
HIP 103389 70	3.32e-03	1.02e-03	3.84e-03	2.31e-03	1.01
HIP 103389 100	2.02e-03	3.62e-04	1.50e-03	8.64e-04	1.06
HIP 107350 100	1.34e-03	3.42e-04	1.46e-03	8.73e-04	1.14
HIP 114948 100	1.23e-03	3.48e-04	1.01e-03	8.18e-04	1.05
HIP 103389 160 a	1.08e-02	2.48e-03	6.18e-03	6.42e-03	1.23
HIP 103389 160 b	3.15e-03	1.17e-03	3.32e-03	2.94e-03	1.19
HIP 107350 160	5.76e-03	1.07e-03	4.40e-03	2.68e-03	1.19
HIP 114948 160	4.11e-03	1.18e-03	3.56e-03	3.11e-03	1.25

Table 9. Clean field correlated noise estimation. The correlated noise factors α_{corr} are estimated as the ratio between the σ_{pix} value obtained for the largest output image pixel size (twice the natural pixel size) and the size of interest. No correlation noise is assumed for the largest output image pixel size. The box size is approximately constant for all output pixel sizes: $\sim 25''$, $50''$ for 100 and 160 μm , respectively.

r	HIP 544 100 μm		HIP 544 160 μm		HIP 99240 100 μm		HIP 99240 160 μm	
	σ_{pix} (Jy)	α_{corr}	σ_{pix} (Jy)	α_{corr}	σ_{pix} (Jy)	α_{corr}	σ_{pix} (Jy)	α_{corr}
3.20	1.91e-05	3.88	5.91e-05	3.61	4.69e-05	3.36	1.14e-04	3.73
1.47	7.79e-05	2.07	2.50e-04	1.85	1.89e-04	1.81	5.05e-04	1.83
1.00	1.56e-04	1.53	5.13e-04	1.33	3.60e-04	1.40	1.05e-03	1.30
0.67	3.09e-04	1.15	8.84e-04	1.16	6.87e-04	1.10	1.97e-03	1.04
0.50	4.75e-04	1.00	1.36e-03	1.00	1.01e-03	1.00	2.73e-03	1.00

For extended sources, the beam radius was chosen large enough to cover the whole extended emission. The corresponding beam aperture correction as given in the technical note PICC-ME-TN-037 was taken into account. The reference background region was usually taken in a ring of width 10'' at a separation of 10'' from the circular aperture size. Nonetheless we took special care to choose the reference sky region for those objects where the “default” sky was or could be contaminated by background objects. In addition, we also carried out complete curve of growth measurements with increasing apertures and the corresponding skies. Sky noise for each PACS band was calculated from the rms pixel variance of ten sky apertures of the same size as the source aperture and randomly distributed across the uniformly covered part of the image (pixel sky noise from the curves of growth are essentially identical). Final error estimates take into account the correlated noise factor estimated by us (see previous section) and aperture correction factors. Figure 3 (top) shows a plot of the mean sky noise value at 100 μm obtained for all images with the same on-source integration time versus the on-source integration time. Error bars are the rms standard deviation of the sky noise values measured in the images taken with the same on-source time; we note that the number of images is not the same for each integration time, so that those error bars are only indicative of the noise behaviour. The plot also shows a curve of the noise assuming that the S/N ratio varies with the square root of the time. The curve is normalized to the mean sky noise value of the images with the shortest integration time, 360 sec, showing that the PACS 100 μm images are essentially background limited. Figure 3 (bottom) is the same plot at 160 μm ; the curve is also normalized to the shortest on-source integration time. The 160 μm noise

behaviour is flatter than the $S/N \propto t^{1/2}$ curve, suggesting that it is influenced by structured background diffuse emission, and that is confusion limited for integration times longer than around 900 seconds. With the second method we carried out photometry using rectangular boxes with areas equivalent to the default circular apertures; in this case, we chose box sizes large enough to cover the whole emission for extended sources. Sky level and sky rms noise from this method were estimated from measurements in ten fields, selected as clean as possible by the eye, of the same size as the photometric source boxes. Photometric values and errors take into account beam correction factors. The estimated fluxes from both methods, circular and rectangular aperture photometry, agree within the errors. PSF photometry of point sources using the DAOPHOT software package was also carried out for those cases where a nearby object is present and prevents us from using any of the two methods above. The fluxes using aperture photometry and DAOPHOT are consistent within the uncertainties for point sources in non-crowded fields. However, the errors provided by DAOPHOT are too optimistic by a typical factor of an order of magnitude. This is a consequence of correlated noise, which cannot easily be handled by DAOPHOT. Using $\alpha_{\text{corr}} \sigma_{\text{pix}}$ as the flux uncertainty for each pixel does not solve the problem. The errors for DAOPHOT photometry have thus been estimated using the formulae derived for standard DUNES aperture photometry. The noise introduced by source crowding is considered negligible as compared to the other major contributors: thermal noise background, stellar flux determination and PACS absolute photometric calibration uncertainties. The absolute uncertainties in this version of HIPE are

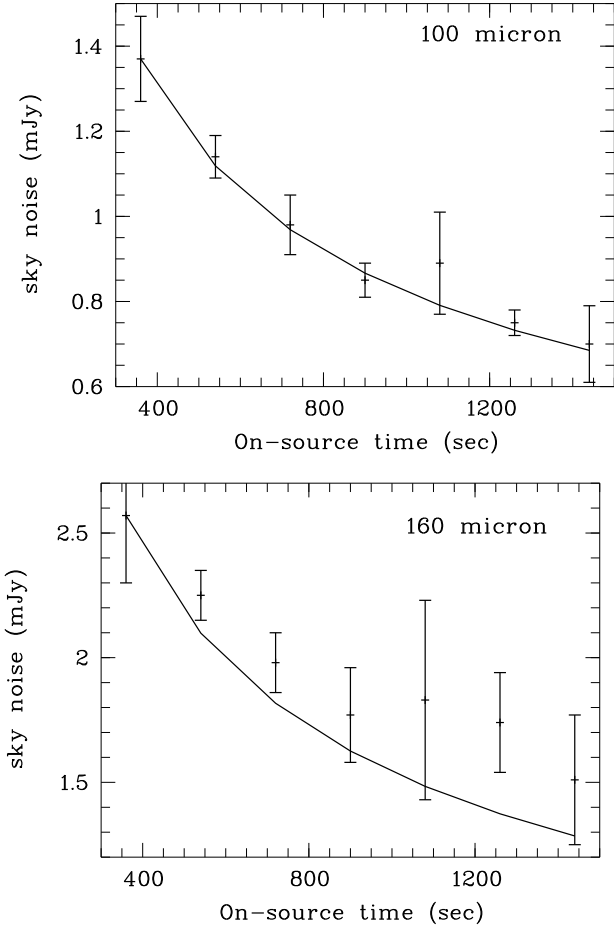


Fig. 3. Top: mean value of the sky noise estimates at 100 μm versus on-source integration time. Error bars are the rms standard deviation of the sky noise in the images taken with the same on-source observing time. The solid curve represents the noise behaviour assuming that the S/N ratio varies as the square root of the time, normalized by the mean value of the images with an on-source exposure time of 360 sec. Bottom: the same for the 160 μm images.

2.64% (70 μm), 2.75% (100 μm) and 4.15% (160 μm), as indicated in the cited technical note.

6.1.2. Pointing: excess/non-excess sources

PACS at 100 and 160 μm are very sensitive to background objects, usually red galaxies and, therefore, there is a non-negligible chance of contamination (Section 7.2.1). Thus, it is necessary to check the agreement between the optical position of the stars and the one of the objects identified as their *Herschel* counterparts - as well as in the cases of non-excess sources the agreement between the measured PACS fluxes and the predicted photospheric levels (Section 7.1). Table 10 gives the J2000.0 optical equatorial coordinates and the PACS positions at 100 μm , corrected from the proper motions of the stars as given by van Leeuwen (2008). Figure 4 shows histograms of the positional offset between the optical and PACS 100 μm positions for all the stars, as well as separately for the non-excess (including here the spurious sources, see below) and excess sources. In all three stellar samples $\sim 65\%$ of the stars have offsets less than $2''.4$, which

Table 10. Optical and PACS 100 μm equatorial positions (J2000) of the DUNES stars together with the positional offset between both nominal positions. Only the first 5 objects of the sample are presented here; the full version of the table is available as online material.

HIP	ICRS(2000)	PACS100	Offset (arcsec)
171	00 02 10.16 +27 04 56.1	00 02 10.57 +27 04 56.0	5.5
544	00 06 36.78 +29 01 17.4	00 06 36.79 +29 01 15.8	1.6
910	00 11 15.86 -15 28 04.7	00 11 15.88 -15 28 03.4	1.3
2941	00 37 20.70 -24 46 02.2	00 37 20.54 -24 46 03.9	2.8
3093	00 39 21.81 +21 15 01.7	00 39 21.84 +21 14 58.9	2.8

is the expected *Herschel* pointing accuracy⁷, while there are 5 non-excess stars and only one excess star with positional offsets $> 2\sigma$. In this respect we note that based on a grid of known 24 μm sources, Berta et al. (2010) found absolute astrometric offsets in the GOODS-N field as high as $5''$.

The non-excess sources with offsets $> 2\sigma$ are: HIP 28442, HIP 34065, HIP 54646, HIP 57939 and HIP 71681 (α CenB - HIP 71683 is α CenA and has an offset of $4''.2$). These non-excess sources, excluding α Cen, are faint with no or dubious (the case of HIP 34065) 160 μm detection, but their estimated 100 μm fluxes agree well with the photospheric predictions, $|F_{\text{PACS}100} - F_{\text{star}}| < 1.6$ mJy. HIP 57939 has an extremely high proper motion; the rest are multiple stars. HIP 28442, which shows a very large offset, the largest one, is an outlier. However, it has a very large parallax error (21 mas) and is a member of a quadruple star, CCDM J06003-3103ABC; its optical and 2MASS coordinates differ around $6''$ - in fact, the offset between the PACS 100 μm and 2MASS coordinates is only of $\sim 4''$. Further, the accuracy of its proper motion is somehow dubious. After the proper motion values as given in the LHS catalogue (Luyten 1979) the offset between the optical and *Herschel* positions would just be $\approx 4''$, but the revised version of that catalogue (Bakos et al. 2002) presents proper motions similar to those of *Hipparcos*. Thus, the real offset remains unsolved. In the case of α Cen the offset values in Table 10 do not take into account its orbital motion. Correcting from that orbital motion we find an offset for α Cen A relative to the pointed position of $1''.7$ at 100 μm , i.e., well below the 1σ pointing accuracy (Wiegert et al. in preparation). We do not have orbital motion information for the rest of the multiple sources. Finally, the offset between the nominal optical position and the 100 μm peak of the star HIP 40843 (Figure D.1) is $7''.1$, but this result most likely reflects a case of coincidental alignment (see section 7.2.1 and Appendix D).

The excess-source with offset $> 2\sigma$ is HIP 171. Again this object is a binary with a separation between components of $0''.83$, the component B being a binary itself (Bach et al. 2009). We do not have information on the orbital motion so that the PACS 100 μm position cannot be corrected, but its 100 μm flux is very well in agreement with the photospheric prediction of the multiple system, $|F_{\text{PACS}100} - F_{\text{star}}| < 1.0$ mJy (Section 7.2).

6.2. SPIRE

The method of flux measurement in the SPIRE maps was dependent on the expected source brightness and extent (compared to the instrument PSF) in each band, following the recommendations of the SPIRE data reduction guide⁸ (see SPIRE DRG Fig 5.57, Section 5.7). In the case of extended sources (HIP 7978, HIP 32480 and HIP 107649), flux measurement was made via

⁷ <http://herschel.esac.esa.int/twiki/bin/view/Public/SummaryPointing>

⁸ <http://herschel.esac.esa.int/hcss-doc-9.0>

Table 11. SPIRE fluxes (F_λ) with 1σ errors, together with the photospheric predictions (S_λ). The significance at each band is given. Figures without errors in the SPIRE columns give 3σ upper limits for the corresponding stars.

HIP	F250 (mJy)	S250 (mJy)	χ_{250}	F350 (mJy)	S350 (mJy)	χ_{350}	F500 (mJy)	S500 (mJy)	χ_{500}
544	<22.5	1.20±0.03		<24.3	0.61±0.02		<9.2	0.30±0.01	
7978	312.30 ± 25.60	1.37±0.08	12.15	179.90 ± 14.60	0.70±0.04	12.27	78.40 ± 9.80	0.34±0.02	7.97
13402	<23.1	1.63±0.03		<23.1	0.83±0.02		<9.4	0.41±0.01	
15371	59.72 ± 6.70	2.03±0.03	8.61	24.68 ± 6.89	1.04±0.02	3.43	20.29 ± 7.66	0.51±0.01	2.58
17439	53.00 ± 10.40	0.68±0.01	5.03	32.20 ± 8.90	0.35±0.01	3.58	<7.2	0.17±0.01	
22263	23.21 ± 6.81	1.66±0.03	3.16	14.14 ± 6.87	0.85±0.02	1.93	<9.6	0.42±0.01	
32480	90.00 ± 15.00	1.75±0.02	5.88	25.00 ± 8.00	0.89±0.01	3.01	<24.0	0.44±0.01	
40843	<24.0	1.77±0.01		<23.7	0.90±0.01		<26.4	0.44±0.01	
51502	49.65 ± 8.29	1.30±0.02	5.83	41.01 ± 8.15	0.66±0.01	4.95	23.10 ± 9.41	0.33±0.01	2.42
72603	<24.0	1.43±0.01		<24.3	0.73±0.01		<30.9	0.36±0.01	
83389	<20.1	0.64±0.01		<21.0	0.33±0.01		<24.0	0.16±0.01	
84862	<20.1	1.95±0.02		<21.0	0.99±0.01		<24.3	0.49±0.01	
85235	<22.2	1.00±0.02		<23.1	0.51±0.01		<29.4	0.25±0.01	
85295	<19.8	1.66±0.04		<21.0	0.85±0.02		<24.0	0.42±0.01	
92043	12.12 ± 6.57	3.85±0.05	1.26	<21.9	1.96±0.03		<24.3	0.96±0.01	
101997	<19.5	0.91±0.02		<21.0	0.46±0.01		<24.6	0.23±0.01	
105312	<19.8	0.93±0.05		<20.7	0.47±0.03		<24.0	0.23±0.01	
106696	<19.5	0.65±0.01		<20.7	0.33±0.01		<24.9	0.16±0.01	
107649	113.00 ± 18.00	1.44±0.02	6.20	44.30 ± 9.00	0.73±0.01	4.84	25.90 ± 8.00	0.36±0.01	3.19
108870	<19.8	9.86±0.23		<21.0	5.03±0.12		<23.4	2.47±0.06	

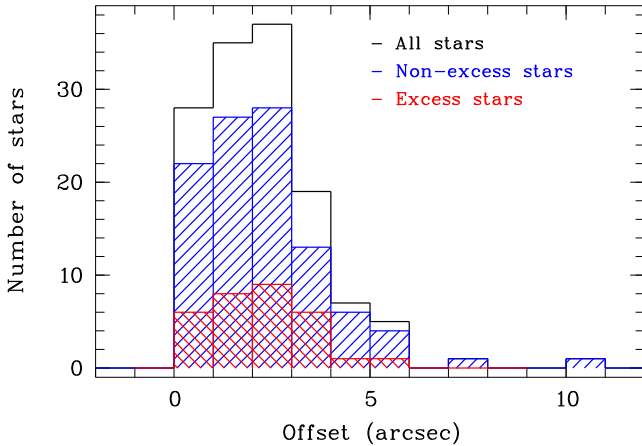


Fig. 4. Histograms of the offset position between the optical and the PACS $100\ \mu\text{m}$ coordinates. Histograms are shown for the whole DUNES sample of stars, the non-excess stars and excess star candidates. The spurious sources (see section 7.1) are included as non-excess stars in this figure.

aperture photometry with aperture radii large enough to cover the source and a sky annulus of $60''$ – $90''$. In the case of point sources brighter than 30 mJy (HIP 544, HIP 13402, HIP 17439 and HIP 22263), the timeline fitter task was used to estimate the photometry using aperture radii of $22''$ at $250\ \mu\text{m}$, $30''$ at $350\ \mu\text{m}$ and $42''$ at $500\ \mu\text{m}$ with a background annulus of $60''$ – $90''$ for all three bands. Finally, in the case of sources fainter than 30 mJy or non-detections, the SUSSEXtractor tool was used to estimate the flux or $3\text{-}\sigma$ upper limits from the sky background and rms, as appropriate. A summary of the SPIRE photometry is presented in Table 11 and the flux values are plotted in Figure E.1.

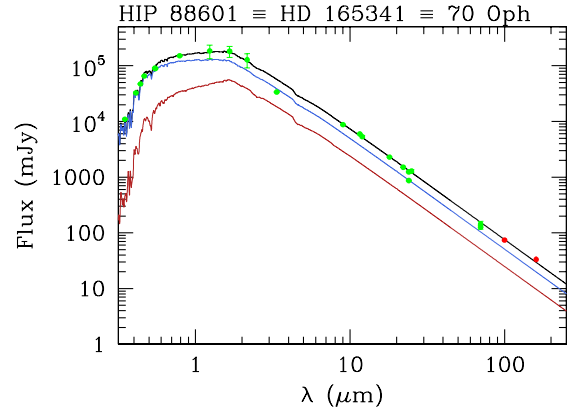


Fig. 5. Spectral energy distribution of the non-excess star HIP 88601. Plotted are optical, near-IR, WISE, and *Spitzer* MIPS (green symbols), as well as the PACS $100\ \mu\text{m}$ and $160\ \mu\text{m}$ (red symbols) fluxes. The photospheric fits of each individual component together with the added contribution of both stars (black) are shown as continuous lines.

7. Analysis

7.1. Non-excess sources

We consider that a star has an infrared excess at any PACS wavelength when the significance, $\chi_\lambda = (\text{PACS}_\lambda - S_\lambda)/\sigma$, is larger than 3, where PACS_λ is the measured flux, S_λ is the predicted photospheric flux and σ is the total error. The predicted fluxes are based on a Rayleigh-Jeans extrapolation from the $40\ \mu\text{m}$ fluxes estimated from the PHOENIX/GAIA LTE atmospheric models (see Appendix C). The sources for which no clear excesses are detected at any of the *Herschel* PACS bands are listed in Table 12, where the PACS fluxes, photospheric predictions, and significance of the detections at each PACS band are given. Figures without errors in the PACS160 column give 3σ upper limits. Errors of the PACS fluxes are the quadratic sum of the photometric errors and the absolute calibration uncertainties; for

Table 12. PACS fluxes with 1σ errors of non-excess sources, together with the photospheric predictions (S_λ). The significance at each band is given. Figures without errors in the PACS160 column give 3σ upper limits. Figures in the column L_d/L_\star give upper limits of the fractional luminosity of the dust. The last column gives *Spitzer* fluxes at $70\ \mu\text{m}$. Units for fluxes and photospheric predictions are mJy. Only the first 5 lines of the table are given here. The full version is available as online material.

HIP	SpT	PACS70	S70	χ_{70}	PACS100	S100	χ_{100}	PACS160	S160	χ_{160}	L_d/L_\star	MIPS70
910	F5V		29.51±0.19		17.66± 1.38	14.46±0.09	2.32	<7.5	5.61± 0.04		8.9e-07	37.50±4.48
2941	K1V+...		24.09±0.43		11.20± 1.82	11.80±0.21	-0.33	<5.7	4.61± 0.08		2.0e-06	25.80±11.93
3093	K0V	21.93 ±1.69	22.50±0.34	-0.33	8.21± 1.23	11.02±0.17	-2.26	3.76± 3.43	4.31± 0.07	-0.16	1.7e-06	14.90±5.69
3497	G3V	7.97 ±0.95	8.72±0.10	-0.78	5.23± 1.01	4.27±0.05	0.95	<4.8	1.67± 0.02		2.8e-06	5.20±4.41
3821	G0V SB		131.05±2.06		60.80± 2.04	64.21±1.01	-1.50	15.75± 2.66	25.08± 0.39	-3.47	3.3e-07	122.3±10.74

the photometric errors, we have taken the conservative approach of choosing the largest error values estimated either from the circular (σ_{pix} metric) or from the rectangular aperture photometry (σ_{sky} metric). Errors of the predicted fluxes are estimated by means of the least reduced χ^2 procedure described in Appendix C. The significance values in Table 12 are estimated taking as the total error the quadratic sum of the PACS and predicted flux errors. *Spitzer* $70\ \mu\text{m}$ MIPS fluxes estimated again for this work are given in the last column of the table. The total number of the non-excess sources are 95 out of 133 ($\sim 71\%$). The spectral type distribution of this type of objects (see Table 13) is 16 F-type stars ($\sim 59\%$ of the total DUNES F-type stellar sample), 37 G-type stars ($\sim 71\%$ of the G-type) and 42 K-type stars ($\sim 78\%$ of the K-type). As an example of the photospheric fits, Figure 5 shows the observed SED of the binary star HIP 88601 (V 2391 Oph, 70 Oph AB), where the fit takes into account the contribution of both components (Eggenberger et al. 2008). A histogram of the significance χ_{100} of the non-excess sources is shown in Figure 6. The median value of χ_{100} is -0.44 , and the mean value is -0.50 with a standard deviation of 1.18. A gaussian curve with this σ value is also plotted. If we directly consider the differences between observed and predicted fluxes, we obtain a mean value of the $100\ \mu\text{m}$ flux offset of -0.54 mJy with a standard deviation of 1.40 mJy (α Cen is not included); the median value is -0.60 mJy. We note that the standard deviation of the $100\ \mu\text{m}$ flux offsets is approximately of the same order as the corresponding sky noise value. The difference in flux suggests that we might be detecting a small far-IR deficit between the observed and predicted fluxes. This trend, if real, might be reflecting the fact that the extrapolation of the photospheric fits (based on atmospheric models) to the PACS bands does not take into account that in solar-type stars the brightness temperature decreases with the wavelength as the free-free opacity of H^- increases. In the Sun the origin of the far-IR radiation moves to higher regions in the photosphere, the so-called temperature minimum region (Avrett 2003). The apparent weak far-IR deficit we observe in the DUNES sample might at least partly be due to this temperature minimum effect in solar-type stars. In fact, an in-depth analysis of α Cen A using the DUNES *Herschel* data strongly argues for the first measurement of this temperature minimum effect in a star other the Sun (Liseau et al. 2013).

Two stars in Table 12, HIP 40693 and HIP 72603, have *Spitzer* fluxes in excess of the photospheric emission. HIP 40693 (HD 69830) has a well characterized warm debris disc, as shown by the MIPS IRS excess between 8 and $35\ \mu\text{m}$ but no excess at $70\ \mu\text{m}$ (Beichman et al. 2005, 2011); we do not detect any 100 or $160\ \mu\text{m}$ excess with PACS. The *Spitzer* MIPS $70\ \mu\text{m}$ of HIP 72603 (Table 12) suggests the presence of a far-IR excess; however, this is clearly not supported by the *Herschel* data since the observed PACS $70\ \mu\text{m}$ is in very good agreement with the predicted photospheric fluxes, as well the PACS 100 and $160\ \mu\text{m}$ results. The $100\ \mu\text{m}$ aperture photometry flux of HIP 82860 given

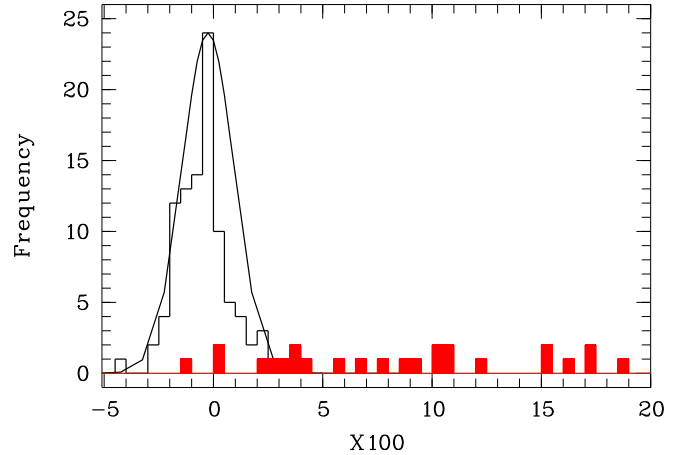


Fig. 6. Histogram of the $100\ \mu\text{m}$ significance for the non-excess (empty histogram) and excess (red filled histogram) sources. The continuous line is a gaussian with $\sigma = 1.18$, which is the standard deviation of the χ_{100} values of non-excess sources. Excess sources with $\chi_{100} < 3$ are cold disc candidates (see section 7.2.4).

in Table 12 presents a marginal excess ($\chi_{100} = 2.7$) but it is most likely contaminated by a bright nearby galaxy. PSF photometry gives 13.2 mJy. Both HIP 82860 and the nearby bright background galaxy cannot spatially be resolved at $160\ \mu\text{m}$. A similar situation is found with HIP 40843 (see Appendix D and Table D.1), whose apparent excesses with *Spitzer* and PACS are most likely due to contamination by a nearby galaxy.

There are 7 stars (Table D.1) with $160\ \mu\text{m}$ significance $\chi_{160} > 3.0$; 2 of them also have $100\ \mu\text{m}$ significance $\chi_{100} > 3.0$. However, the genuineness of those excesses are questionable since there are extended, background structures or nearby bright objects which impact on the reliability of the $160\ \mu\text{m}$ estimates. A description of these objects with contourplots and images is given in Appendix D. Summarizing these two last paragraphs, the stars HIP 40693, HIP 72603, and HIP 82860 are listed in Table 12 as non-excess stars with *Herschel*, while the 7 stars in Table D.1 (included the mentioned HIP 40843) are neither considered excess stars because their χ values larger than 3 are questionable.

7.1.1. Dust luminosity upper limits of non-excess sources

Upper limits of the dust fractional luminosities, L_d/L_\star , of the non-excess sources are given in Table 12. Those values have been estimated from the 3σ statistical uncertainty of the $100\ \mu\text{m}$ flux using the expression (4) by Beichman et al. (2006) and assuming a black body temperature of 50 K, which is a representative value for $100\ \mu\text{m}$. Figure 7 presents a histogram of the L_{dust}/L_\star upper limits. The mean and median values of these up-

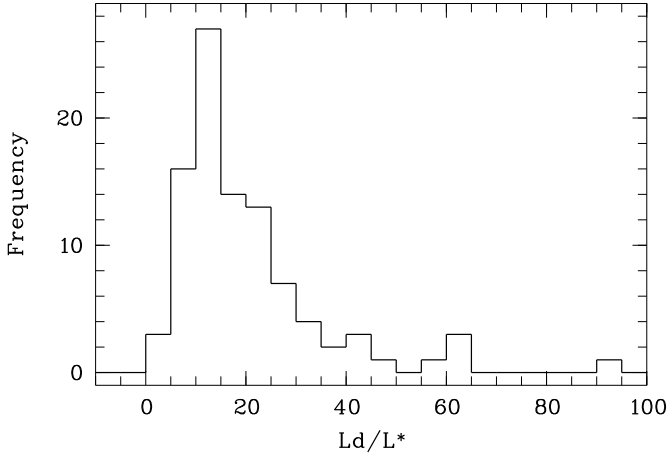


Fig. 7. Histogram of the upper limit of the fractional luminosity of the dust of the non-excess sources. Units: 10^{-7}

per limits are 2.0×10^{-6} and 1.6×10^{-6} , respectively. There are 19 stars (8 F-type, 6 G-type, and 5 K-type) out of the 95 non-excess stars with $L_d/L_\star < 10^{-6}$, i.e., a few times the EKB luminosity. The two stars with the lowest upper limits, $L/L_\star < 5.0 \times 10^{-7}$, are located at distances less than 6.1 pc, i.e. they are very nearby stars (HIP 3821 and HIP 99240). These upper limits represent an increase in the sensitivity of around one order of magnitude with respect to the detection limit with *Spitzer* at different spectral ranges (e.g. Trilling et al. 2008; Lawler et al. 2009; Tanner et al. 2009).

Figure 8 presents the L_d/L_\star upper limits as a function of the effective temperature of the stars, i.e., spectral types (top plot) and of the distance to the stars (middle plot). Similar plots have been presented by Trilling et al. (2008) and Bryden et al. (2009). Our plots show that while the L_d/L_\star upper limits tend to increase for the later K-type stars, the closer stars have low upper limit values, irrespectively of their temperatures. The bottom plot of Figure 8 reflects that the flux contrast between the stellar photosphere and a potentially existing debris disc is determined by the bias introduced simultaneously by the distances and spectral types.

7.2. Excess sources

A total of 31 out of the 133 DUNES targets show excess above the photospheric predictions: 9 F-type, 12 G-type and 10 K-type stars (Table 13). The excess sources with the estimated PACS fluxes, the photospheric predictions and the significance of the excess at each PACS band are listed in Table 14. We also include the MIPS70 μm flux of each object. In general PACS70 and MIPS70 fluxes are in good agreement, although in the case of HIP 4148 the larger MIPS excess is likely due to contamination by nearby objects. Figure 6 shows χ_{100} and χ_{160} histograms of the excess sources (up to the value of 20). Stars with $\chi_{100} < 3.0$ correspond to the cold disc candidates (see below section 7.2.4), while stars with $\chi_{160} < 3.0$ correspond to the steep SED sources (see below section 7.2.5). Figure E.1 shows the observed SEDs of the stars. The number of excess sources detected with *Herschel* data reflects an increase of 10 sources with respect to the number of previously known 70 μm MIPS *Spitzer* excess sources (HIP 72603 is excluded since it does not have a 70 μm excess with *Herschel*). We note again that HIP 40693 is a 24 μm warm excess, but without 70 μm excess; this

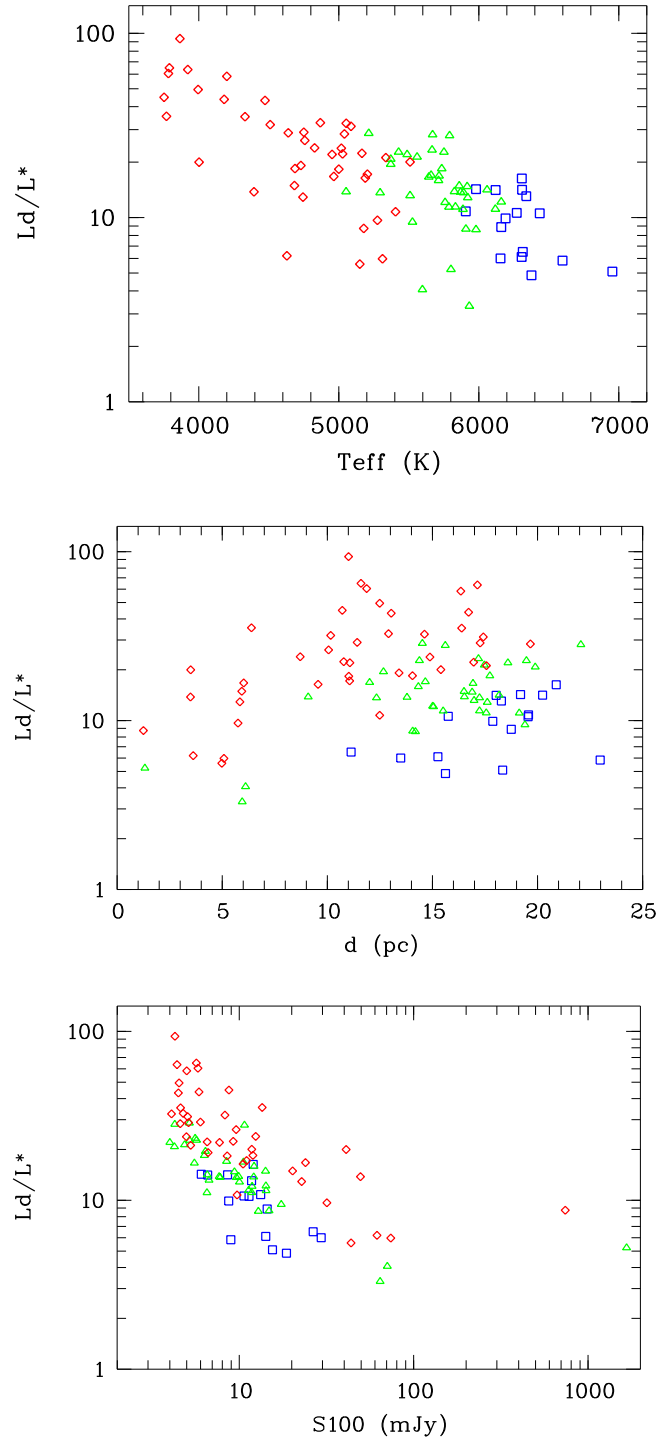


Fig. 8. Upper limit of the fractional luminosity of the dust (units: 10^{-7}) for the non-excess sources versus effective temperature of the stars (top), distance (middle) and stellar flux (bottom). Blue squares: F-type stars; green triangles: G-type stars; red diamonds: K-type stars.

object is not listed in Table 14. HIP 171 has been reported as having an excess at 24 μm but no 70 μm MIPS excess (Koerner et al. 2010); in this case, we consider it as a new detection. We note that most of the new excess sources are K-type stars; this trend clearly reflects the higher sensitivity of *Herschel* to detect lower contrast ratios between the stellar and dust-disc fluxes, particularly at 100 and 160 μm .

Table 13. Overall description of the DUNES sample and summary results. Percentages in parenthesis refer to the amount of stars in the corresponding spectral types or the whole samples. Single numbers in parenthesis refer to the number of new debris disc stars identified in this survey.

Sample	F stars	G stars	K stars	Total
Solar-type stars observed by DUNES (the DUNES sample)	27	52	54	133
20 pc DUNES subsample	20	50	54	124
Non-excess stars in the whole DUNES sample	16(59%)	37(71%)	42(78%)	95(71%)
Affected by field contamination	2	3	2	7
Excess stars in the whole DUNES sample	9(2)	12(3)	10(5)	31(10)
Excess stars in the 20 pc subsample	4(20%)	11(22%)	10(18.5%)	25(20.2%)
Resolved debris discs	5(4)	6(4)	5(5)	16 (13)

In order to cleanly assess the increase of the incidence rate provided by *Herschel* with respect to *Spitzer*, we note that the figures of the previous paragraph are biased since we selectively included 9 stars between 20 and 25 pc with planets and/or *Spitzer* debris discs in the 133 DUNES sample (see section 3). Correcting the figures from this bias, i.e., considering the 20 pc DUNES sample of 124 stars, and also taking into account that the *Spitzer* excess of HIP 72603 is not supported by our PACS data, the number of previously known stars with *Spitzer* excesses at 70 μm is 15, while the total number of *Herschel* excess sources, either at 100 and/or 160 μm , are 25. This represents an increase of the incidence rate from the *Spitzer* $12.1\% \pm 5\%$ to the *Herschel* $20.2\% \pm 2\%$ rate, i.e., around 1.7 times larger. The gain in the debris disc incidence rate varies very much with the spectral type. The 20 pc DUNES sample is formed by 20 F-type stars, 50 G-type stars and 54 K-type stars. According to spectral types, the *Spitzer* discs are surrounding 2 F-type stars ($\sim 10.0\%$), 9 G-type stars ($\sim 18.0\%$) and 5 K-type stars ($\sim 9.3\%$). The same values for *Herschel* are: 4 (20.0 %) for the F-type stars, 11 (22%) for the G-type stars and 10 (18.5 %) for the K-type stars (Table 14). We note that the fraction of stars with *Spitzer* excesses in our sample is a bit lower than what has been found in different FGK star programmes specifically focused to detect debris discs with the *Spitzer*/MIPS photometer (e.g. Trilling et al. 2008; Hillenbrand et al. 2008). This is possibly due to the highest spatial resolution of our *Herschel* images, which partly avoids the contamination suffered by the largest *Spitzer* beam.

The results described in the previous paragraph point to an incidence rate of debris discs around main-sequence, solar-type stars of around 20 %, irrespectively of spectral type. This result can be considered as a lower limit to the true number of such discs and it must be taken very cautiously since it is affected by different sorts of biases, as well the previous ones with *Spitzer* were. We have shown in section 7.1.1 how the L_d/L_\star upper limit depends on the combined effect of the stars' spectral types and distances. This is a strong bias clearly penalizing late type stars at distances larger than around 10 pc (see Figure 8). In addition, our 20 pc sample is not complete for K-type stars for distances larger than around 15 pc due to *Hipparcos* completeness. If we restrict the DUNES sample up to 15 pc to avoid this incompleteness, our incidence rate is strongly affected, mainly with respect to the F-type stars. The reason is that most of the nearby F-type stars are bright enough to detect the stellar photosphere with the shallower DEBRIS integration time and, according to the DUNES/DEBRIS agreement, those stars have been observed by that *Herschel* OTKP.

7.2.1. Background contamination and coincidental alignment.

Some of the PACS images reveal large scale field structures denoting the presence of interstellar cirrus. Good examples are some stars located close to the galactic plane like HIP 71683/81 (α Cen A/B), HIP 124104/07 (61 Cygni A/B) or HIP 71908 (α Cir). These structures make it difficult to estimate reliable PACS fluxes and even can mimic an excess over the predicted photospheric flux (see Appendix D for some examples).

In addition, as indicated before, the PACS 100 and 160 μm images are very sensitive to background objects. Therefore, the possibility of coincidental alignment of such sources with our stars, hindering a reliable flux measurement or artificially introducing an excess, cannot be excluded. To assess this potential contamination one needs to take into account the correlation between the optical and *Herschel* positions, the photospheric predictions at the different wavelengths and the *Herschel* observed fluxes, as well as the density of extragalactic sources. HIP 82860 is a concrete example of such a case of contamination. The estimated 100 μm flux agrees well with the predicted photospheric flux (Table 12) but we cannot reliably measure the 160 μm flux due to the presence of a bright, red background galaxy (42.2 and 56.0 mJy at 100 and 160 μm , respectively) located at a distance of $\sim 10''$ from the star (Figure 9). That distance and the 160 μm ratio between the star and the galaxy (the 160 μm predicted flux of HIP 82860 is 5.5 mJy) prevent us from resolving both objects, even using deconvolution techniques. Further examples of such potential contamination by extended structures or background galaxies are presented in Appendix D, where PACS images of seven objects with significances $\chi_{160} > 3$ (some cases also with $\chi_{100} > 3$) are described. We remark that none of those objects are identified as excess sources in this work.

Nonetheless, we need to evaluate the impact of contamination by coincidental alignment in our identified debris disc stars. In the following we make some probabilistic estimates to quantitatively assess the chances of misidentifications of background objects with debris discs. We follow the results obtained by Berta et al. (2011), who studied the cosmic infrared background in a few large areas of the sky and carried out number counts, i.e., source densities, in the PACS bands and flux range from ~ 1 mJy to few hundreds mJy. This is the range of interest for our observations. We base our estimates on Figure 7 of Berta et al. (2011), which provides differential number counts per square degree for the PACS bands in the GOODS-S field. We firstly note that many of our identified *Herschel* debris discs have very large excesses, several tens of mJy in the PACS bands, and that some of them even show IR excess emission over the photosphere in the mid-IR wavelength range of the *Spitzer* IRS instrument (see Figure E.1). In those cases, the probability of confusion due to background objects is practically negligible. The problem-

atic misidentifications arise for those with low excesses at $160\ \mu\text{m}$, of the order of few mJy, with small χ_{160} values and very low or non-excess at $100\ \mu\text{m}$. Specifically we identify 6 objects (Table 14): HIP 171, HIP 27887, HIP 29271, HIP 49908, HIP 92043, and HIP 109378. The $160\ \mu\text{m}$ differential number counts for sources with flux level $\sim 5\text{-}6\ \text{mJy}$ from Figure 7 of Berta et al. (2011) is ~ 2000 sources per square degree and mJy, while for fluxes $\sim 12\text{-}13\ \text{mJy}$ is ~ 400 sources per square degree and mJy. This flux range recovers the observed excesses of the above objects. The size of the sky area to estimate the density of sources is taken as the one for which two different objects can be resolved. In this respect, we note that $\alpha\ \text{Cen A}$ and B with flux ratio of about 2 and a separation of $\sim 3''.1$ on the PACS $100\ \mu\text{m}$ images can clearly be distinguished, but not at $160\ \mu\text{m}$. In parallel, we have introduced two fake objects with the same flux, $7\ \text{mJy}$, at different angular separations in the PACS $100\ \mu\text{m}$ and $160\ \mu\text{m}$ images of one of our fields. Using a 2D gaussian treatment we could recover both fake objects at angular distances of $3''$ and $5''$ at 100 and $160\ \mu\text{m}$, respectively. These figures are consistent with the $\alpha\ \text{Cen}$ observational result and slightly smaller than the *Herschel* beam sizes. Thus, taking the conservative approach of the source density for the lowest excess, 0.0121 is the number of $160\ \mu\text{m}$ sources in a field of area corresponding to the estimated angular separation, which implies that the probability of a coincidental alignment of a background galaxy is $1.2\ \%$. Considering the 133 DUNES stars, the binomial probability that all six objects mentioned above are background galaxies is just 0.4% , however the chance that one is a false disc detection is 32% .

and false alarms, although some observational perspectives can be traced (Krivov et al. 2013, submitted). On the other hand, a detailed analysis of the number counts and the source density in the DUNES fields as a function of flux levels, colours and the galactic latitude will be published in a forthcoming paper (del Burgo et al. in preparation).

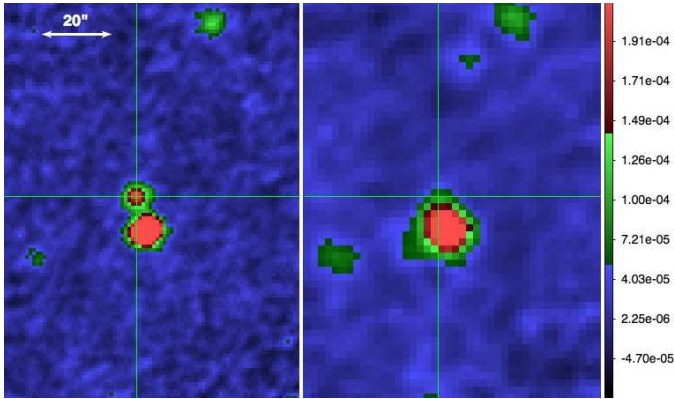


Fig. 9. PACS $100\ \mu\text{m}$ (left) and $160\ \mu\text{m}$ (right) images of HIP 82860. The crosshair denotes the position of the $100\ \mu\text{m}$ flux peak. The angular scale is shown in the $100\ \mu\text{m}$ image by a $20''$ segment. Flux scale units are Jy/pixel. North is up and East to the left.

We note that the estimated probabilities depend on a number of assumptions. The main one is to assume that all DUNES fields have equal source densities as the GOODS-S field. This is simply not true since the number counts change significantly from field to field. However, Sibthorpe et al. (2012) have found no statistically significant cosmic variance based on $100\ \mu\text{m}$ data from the DEBRIS survey; further, assuming that this result is also valid at $160\ \mu\text{m}$ and flux levels below the DEBRIS detection limit, they estimate a confusion probability based on the Berta et al. (2011) $160\ \mu\text{m}$ data which is in excellent agreement with our own estimate above. Thus, we conclude that the probability that all faint debris discs in Table 14 are background galaxies is rather low, although we certainly cannot exclude false identifications. At present we cannot distinguish between real cases

Table 14. Excess sources. PACS fluxes (PACS λ) together with the photospheric predictions (S λ) and the significance at each band. The fractional luminosities and the black body temperatures and radii of the dust are also given. *Spitzer* fluxes at 70 μ m are also given.

HIP	SpT	PACS70 (mJy)	S70 (mJy)	χ_{70}	PACS100 (mJy)	S100 (mJy)	χ_{100}	PACS160 (mJy)	S160 (mJy)	χ_{160}	L_d/L_*	T_d (K)	R_d (AU)	MIPS70 (mJy)	Notes
171	G3V		22.90±0.44		11.70± 1.26	11.22±0.21	0.38	12.48± 2.36	4.38±0.08	3.43	≤21.6e-06	≤25	≥ 97.1	44.10±13.63	H,p,c
544	K0V		15.24±0.34		54.12± 1.00	7.47±0.17	47.15	23.03± 2.06	2.92±0.07	9.86	4.8e-05	90	7.5	102.6±7.83	e
4148	K2V	13.66± 1.37	8.98±0.13	3.42	11.33± 1.17	4.40±0.06	5.92	15.64± 1.72	1.72±0.02	8.09	9.4e-06	32	41.2	37.10±6.59	p
7978	F8V	896.20±26.90	17.48±0.99	32.67	897.10±26.90	8.56±0.48	33.03	635.90±31.80	3.35±0.19	19.89	3.1e-04	60	26.6	863.4±58.68	e
13402	K1V		20.72±0.37		51.77± 1.11	10.15±0.18	37.50	36.94± 2.94	3.97±0.07	11.21	1.7e-05	52	17.9	67.70±7.06	e
14954	F8V		26.43±1.17		39.45± 1.75	12.95±0.58	15.14	31.75± 1.16	5.06±0.22	23.01	4.2e-06	40	95.0	42.50±4.76	e, !
15371	G1V	44.50± 2.50	25.78±0.33	7.49	40.40± 2.50	12.63±0.16	11.11	42.60± 2.50	4.93±0.06	15.07	1.0e-05	40	47.7	45.40±4.95	e
17420	K2V	15.99± 1.81	9.36±0.13	3.66	14.79± 0.84	4.58±0.06	12.15	10.65± 1.30	1.79±0.03	6.82	9.2e-06	45	20.7	23.60±5.44	H,p,s
17439	K1V	74.80± 4.10	8.61±0.14	16.14	75.00± 4.20	4.22±0.07	16.85	74.60± 4.70	1.65±0.03	15.52	8.1e-05	48	21.3	88.50±7.46	e
22263	G3V		21.13±0.38		77.60± 2.00	10.35±0.18	33.62	47.00± 3.00	4.04±0.07	14.32	2.9e-05	70	15.4	113.6±8.53	e
27887	K3V	14.60± 1.43	10.01±0.19	3.21	8.05± 0.95	4.90±0.10	3.32	8.02± 1.50	1.92±0.04	4.07	3.8e-06	29	46.2	17.20±4.94	H,p
28103	F1V		56.33±0.31		45.46± 1.42	27.60±0.15	12.58	9.37± 1.84	10.78±0.06	-0.77	6.3e-05	100	18.3	93.90±7.76	p,s
29271	G5V		35.50±0.42		17.80± 1.30	17.40±0.21	0.31	14.35± 2.00	6.80±0.08	3.78	≤29.7e-06	≤22	≥147.3	42.60±10.50	H,e,c
32480	G0V	264.00± 4.10	22.33±0.27	58.94	252.30± 3.18	10.94±0.13	75.90	182.09± 3.77	4.27±0.05	47.17	6.9e-05	60	28.5	262.8±18.29	e
42438	G1.5Vb		18.12±0.25		17.31± 0.80	8.88±0.12	10.54	6.73± 2.04	3.47±0.05	1.60	1.1e-05	99	7.8	41.20±4.16	p,s
43726	G3V		13.48±0.26		15.77± 0.76	6.60±0.13	12.07	6.09± 1.42	2.58±0.05	2.47	1.6e-05	99	7.9	32.50±4.13	p,s
49908	K8V		55.55±2.11		22.50± 0.90	24.59±1.03	-2.33	16.00± 1.70	9.61±0.40	3.16	≤21.6e-06	≤22	≥ 56.6	38.70±4.69	H,e,c
51459	F8V		31.14±0.53		19.71± 1.42	15.26±0.26	3.13	9.17± 2.79	5.96±0.10	1.15	9.1e-07	50	38.6	33.80±4.43	H
51502	F2V		16.57±0.22		47.25± 2.00	8.12±0.11	19.57	72.45± 2.22	3.17±0.04	31.21	1.3e-05	30	145.0	39.60±3.79	e, !
62207	G0V		13.45±0.11		55.06± 2.39	6.59±0.05	20.28	44.49± 3.17	2.57±0.02	13.22	2.1e-05	66	18.3	55.70±5.20	e
65721	G5V		42.07±0.36		40.73± 0.66	20.61±0.17	30.48	26.97± 1.39	8.05±0.07	13.61	3.8e-06	45	66.1	79.00±8.09	p
71181	K3V	15.06± 1.30	9.98±0.16	3.91	8.79± 1.00	4.89±0.08	3.90	1.63± 1.63	1.91±0.03	-0.17	8.0e-06	70	7.9	29.20±8.04	H,p,s
72848	K2V		21.45±1.06		19.60± 2.00	10.51±0.52	4.55	13.30± 1.12	4.11±0.20	8.21	2.8e-06	40	34.2	33.50±6.41	H,e
73100	F7V		14.42±0.23		13.84± 0.81	7.06±0.11	8.37	12.46± 2.27	2.76±0.04	4.27	2.7e-06	30	144.8	24.70±3.17	p,c, !
85235	K0V		12.83±0.19		34.70± 1.18	6.29±0.09	24.08	28.00± 2.52	2.46±0.04	10.13	2.0e-05	45	24.6	58.00±4.92	e
92043	F6V	59.00± 3.50	48.70±0.68	2.94	30.20± 2.40	23.90±0.33	2.63	21.90± 3.80	9.34±0.13	3.31	7.0e-07	30	213.3	69.80±8.93	H,e,c
103389	F7V	44.00± 2.30	13.45±0.23	13.28	26.30± 1.70	6.59±0.11	11.59	7.70± 2.50	2.57±0.04	2.05	1.7e-05	90	13.6	46.60±4.93	p,s, !
107350	G0V		12.51±0.17		15.10± 1.30	6.13±0.08	6.90	4.40± 2.30	2.39±0.03	0.87	1.2e-05	100	8.1	28.40±3.15	p,s
107649	G2V	284.00± 1.50	18.38±0.20	177.0	311.00± 1.00	9.01±0.10	301.9	211.00± 1.50	3.52±0.04	138.3	1.0e-04	55	28.7	278.2±21.46	e
109378	G0		9.51±0.13		8.50± 1.00	4.66±0.07	3.84	12.40± 1.60	1.82±0.03	6.61	5.4e-06	22	160.2	7.90 ±2.26	H,p,c, !
114948	F7V		14.08±0.19		40.80± 1.60	6.90±0.09	21.19	13.30± 2.20	2.69±0.04	4.82	2.7e-05	90	13.1	68.70±5.51	p,s, !

Column Notes: H = new *Herschel* debris disc, p = point-like object, e= resolved object, c = cold disc, s = steep source, ! = stars of the 20-25 pc subsample

7.2.2. Dust properties

The excess infrared emission from the debris discs originates in small dust grains produced in collisions of large bodies. A common approach to estimate the temperature and the irradiated luminosity of those grains is to assume that they behave as black body grains. This approach also allows us to estimate a representative orbital distance of the black body-like dust (Backman & Paresce 1993). This procedure presents several caveats. Observed SEDs of some discs clearly reveal the presence of dust at multiple temperatures (e.g. Hillenbrand et al. 2008; Lawler et al. 2009). A simple look at the SEDs presented in Figure E.1 suggests a range of temperatures of the dust. This can either be due to its location at a range of distances from the star or to dust at the same distance but with different properties. It has already been mentioned the well known fundamental degeneracy between distance and size of the dust particles, as small grains far from the star can produce the same SED as large grains located close in (Krivov 2010). At this point we note that the distribution of dust over a radial range has directly been proven by spatially resolved imaging in scattered and reemitted radiation (e.g. Ertel et al. 2011).

Nevertheless, the simple black body assumption still provides a reasonable approach for most of the debris discs and for comparison among solar-type stars, although the black body radius underestimates the true one (e.g. Wyatt 2008; Ertel et al. 2012b, and references therein). Based on these, black body temperatures, T_d , have been estimated by fitting a black body for those sources with excesses at several bands. Where the excess is observed only at one band, mainly at $160 \mu\text{m}$, the upper limit of the temperature is given. The fractional luminosity of the dust has been estimated integrating the observed excess fluxes; in those cases with excess at one wavelength, we have used the expression (4) of Beichman et al. (2006) assuming a dust temperature of 50 K. The orbital distance at which the dust would be located is estimated following equation (3) from Backman & Paresce (1993). In general, for those objects previously known as debris discs, the dust properties obtained using the *Herschel* data do not differ significantly from those obtained with *Spitzer* (Beichman et al. 2006; Trilling et al. 2008, e.g.). The calculated values for the mentioned three dust parameters are given in Table 14. L_d/L_\star spans approximately two orders of magnitude, $\sim 7 \times 10^{-7} - 3 \times 10^{-4}$, and are in a few cases very close to the sensitivity limit. The new *Herschel* discs tend to be approximately one order of magnitude fainter than the previously known ones, mean values are $\sim 4 \times 10^{-6}$ against $\sim 4 \times 10^{-5}$, respectively (Table 14). T_d values range $\sim 20 - 100$ K, with the lowest temperatures also mainly related to the new *Herschel* discs, mean value ~ 34 K against ~ 64 K. As expected, the black body radius tends to be larger for the *Herschel* discs, mean distance ~ 82 AU against ~ 38 AU. A short compendium of these results is that the new *Herschel* discs trace fainter and colder debris discs than the previously known discs.

7.2.3. Point-like and extended sources

Most of the known debris discs have been characterised by fitting the observed SEDs. Spatially resolved images help to break the inherent SEDs' degeneracies by showing where most dust is located. More than 30 debris discs are known to be resolved (<http://www.circumstellardisks.org>). Resolved imaging at different wavelengths serves not only to confirm the presence of circumstellar discs, but provides important constraints to their properties, like the dust location and reliable temperatures.

Furthermore, resolved discs display features as warps, clumps, rings, asymmetries, etc., which help in the study of the dynamics of the discs and indirectly prove the presence of planets (Wyatt 2008, and references therein).

The *Herschel* PACS observations reveal a large number of stars associated with extended emission at $100 \mu\text{m}$ and/or $160 \mu\text{m}$. Their 3σ flux contours usually show an elliptical-like shape. The size of the extended sources is estimated by fitting ellipses to the 3σ contours of each source by eye. Column 2 and 3 of Table 15 gives the position angle (measured from North to East) and the elliptical $100 \mu\text{m}$ major and minor diameters. We estimate an uncertainty of $\sim 1''$ (i.e., 1 pixel at $100 \mu\text{m}$). We have preferably chosen that wavelength due to the complexity of the surrounding fields at $160 \mu\text{m}$ in many of the objects. In the case of the HIP 29271, HIP 49908, and HIP 92043 their sizes are given at $160 \mu\text{m}$ because they are cold disc candidates (see subsection 7.2.4). To assess if the 3σ contours truly denote extended emission, we proceed in the following manner. Firstly, we have assumed that the source brightness profile is well approximated by a Gaussian and measured the ratio between the peak flux and the 3σ flux values, assuming that this ratio corresponds to a Gaussian at a distance from the center given by the semiaxes of the ellipses representing the 3σ contours. In this way we have estimated the FWHM of the emission in both axes (column 4 of Table 15). Secondly, we have carried out a two-dimensional Gaussian analysis of the sources using the IDL procedure MPFIT2DPEAK, fitting the observed brightness profiles with a rotated 2-D Gaussian profile weighted by the uncertainties, without applying any prior assumption as regards the shape of the emission (column 5 of Table 15). Both methods yield quite consistent results within the uncertainties. Thirdly, once we have the gaussian sizes we need to evaluate whether they reflect truly extended emission. FWHM values of the *Herschel* PACS PSFs are $\sim 7''$ and $12''$ at $100 \mu\text{m}$ and $160 \mu\text{m}$, respectively, but small variations of the PSF due to the brightness of the sources and the observing strategy are known to exist (Kennedy et al. 2012). In order to assess if the sources are resolved, a Monte-Carlo simulation has been carried out taking as reference HIP 544 and HIP 72848, two relatively faint sources with small FWHM values, which in the case of HIP 72848 is only resolved in one direction. The standard star α Boo is taken as representative of a pure point-like PSF. The $100 \mu\text{m}$ PACS image of α Boo has been rotated so that the new x and y axes correspond to the axes of the extended emission, and its PSF has been scaled to the flux of each star. The new α Boo PSF has been inserted in a grid of 2627 and 1568 locations in the cleanest areas of the HIP 544 and HIP 72484 images. For each position the x and y FWHM values have been estimated using a 2D Gaussian fit. This provides the FWHM distribution of point sources with the same flux as the problem objects over a noisy background. No additional noise has been added to the images because the telescope thermal noise and sky confusion, already included in the frames, are much larger than the Poisson contribution for such faint artificial sources. The distributions of the FWHM values obtained with both Monte-Carlo simulations are approximately Gaussian. Thus, by using both Gaussian statistics and the empirical distributions constructed above we can estimate the probability that a point source randomly provides the FWHM values listed in Table 15. The result is that the probability of false positives seems below 0.1%. Since HIP 544 and HIP 72484 are among the most unfavourable cases, we conclude that the extended nature of all objects identified as such in Table 15 is fairly secure. We point out that Kennedy et al. (2012) also claim to have resolved a disc with a FWHM of $8''.2 \times 6''.9$.

Table 15. Stars associated with extended emission. Column 2 gives the position angles on the sky (from North to East). Column 3 gives the elliptical diameters (major,minor) of the 3σ contours. Column 4 (FWHM_c) gives the x and y FWHM values assuming the 3σ contours are Gaussian, while column 5 (FWHM_G) is a 2D Gaussian fit to the whole detected flux. See text for details. The last column gives the wavelength at which the sizes have been estimated.

HIP	Position Angle	Observed diameters (arcsec)	FWHM_c (arcsec)	FWHM_G (arcsec)	Band
544	102°	18.0,16.0	8.8,7.8	8.67±0.10,8.28±0.10	100 μm
7978	51°	39.0,28.0	15.7,11.3	15.5±0.02,9.02±0.02	100 μm
13402	50°	19.0,14.0	9.2,6.7	8.20±0.10,7.61±0.02	100 μm
14954(!)	30°	18.0,14.0	9.4,7.3	9.89±0.10,7.80±0.10	100 μm
15371	98°	39.0,18.0	24.5,11.6	20.00±1.0,12.20±0.36	160 μm
17439	105°	26.0,14.0	13.1,7.1	13.35±0.14,8.68±0.10	100 μm
22263	5°	21.0,16.0	10,7.6	10.20±0.10,8.41±0.09	100 μm
29271	70°	16.0,10.0	14.3,8.9	12.00±1.22,10.00±0.73	160 μm
32480	107°	34.0,20.0	16.0,9.4	17.76±0.07,10.15±0.04	100 μm
49908	50°	18.0,10.0	15.5,8.6	13.00±0.94,11.00±0.60	160 μm
51502(!)	0°	16.0,16.0	8.3,8.3	9.08±0.12,8.10±0.11	100 μm
62207	130°	24.0,14.0	13.4,7.8	13.13±0.19,8.40±0.11	100 μm
72848	75°	21.0,12.0	12.7,7.2	11.07±0.33,6.64±0.20	100 μm
85235	0°	18.0,16.0	10.2,9.0	10.01±0.23,9.21±0.21	100 μm
92043	170°	16.0,10.0	19.1,11.9	14.00±1.10,10.00±0.79	160 μm
107649	125°	17.5,8.0	16.1,11.2		100 μm

(!): Stars of the 20-25 pc subsample

The number of sources listed in Table 15 associated with extended emission is 16, i.e., ~52% out of the 31 excess sources. This represents a huge increase of resolved discs with respect to the 3 sources in our sample previously resolved with *Spitzer* or any other facility (HIP 7978, HIP 32480, HIP 107649). Disc size values in Table 15 are upper limits, since proper deconvolution is required to estimate more realistically the true extension of the debris discs and their structure. This has already been done for some of the sources for which a deeper observational analysis (Liseau et al. 2010; Eiroa et al. 2011; Marshall et al. 2011) or highly detailed modelling (Löhne et al. 2012) has been carried out. Similar work is in progress for a few more sources (Marshall et al., Stapelfeldt et al., Faramaz et al., in preparation).

7.2.4. Cold disc candidates

Some of the identified debris disc sources in Table 14 show an excess at 160 μm but little or no excess at all at 100 μm . These sources are HIP 171, HIP 29271, HIP 49908, HIP 73100, HIP 92043, and HIP 109378. We note that the 100 and 160 μm source positions agree within the astrometric errors. The infrared excesses have been attributed to a new class of cold, debris discs, characterized by low temperatures, $\lesssim 30$ K, and low fractional luminosities (Eiroa et al. 2011). While it cannot be excluded that they suffer from background contamination, i.e., they might not be true circumstellar discs, the probability that one or more of these discs are real is large (section 7.2.1). If true, the nature of these faint, cold discs cannot be explained by simply invoking the “classical” collisional models of debris discs. Alternative scenarios have been explored by Krivov et al. (2013, submitted). They argued that such discs might be composed of nearly unstirred primordial grains with sizes somewhere in the millimeter to kilometer range, which would imply that planetesimal formation has stopped before “cometary” or “asteroidal” sizes were reached, at least in the outer regions of the systems. Discs of this kind would experience low-velocity collisions without any significant production of small, warm grains. As a result, a bulk of the material would have a nearly black body temperature as suggested by the observed SEDs.

7.2.5. Steep SED sources

Some stars in Table 14 show an SED with the largest excess at 70 μm and a decrease with the wavelength at 100 and 160 μm . The stars with this behaviour are: HIP 28103, HIP 42438, HIP 43726, HIP 71181, HIP 103389, HIP 107350 and HIP 114948 (Figure E.1). In some of these stars, the observed flux at 160 μm does not exceed the photosphere, i.e., the significance of the observed fluxes is ≤ 3 , and the spectral index of the excess is steeper than the one corresponding to a black body in the Rayleigh-Jeans regime. The IR excesses are already noticeable in the wavelength range of the IRS instrument of *Spitzer* in all cases. All are point-like sources at 100 μm , which implies FWHM sizes $\leq 90 - 140$ AU, depending on the distance to the star. The morphology of the excess with well defined start- and end-wavelengths suggests, in principle, that the dust is confined in a well defined narrow ring.

Ertel et al. (2012a) made a detailed analysis of this behaviour and demonstrated that the particular SED of the discs provides strong constraints on the dust properties. They showed that the naively expected narrow ring shape of the disc is not very well constrained by the modelling, and found that the steep decrease of the SED is inconsistent with a power-law exponent of the grain size distribution of -3.5 , expected from a standard equilibrium collisional cascade (Dohnanyi 1969). In contrast, a steeper grain size distribution or, alternatively, an upper grain size in the range of few tens of micrometers would be implied. This suggests a strong underabundance of large (millimeter-sized) grains to be present in the discs. Donaldson et al. (2012) recently presented another debris disc showing a similar behaviour, namely HD 3003. This disc, however, is significantly younger and more massive than the discs found in our survey and challenges the scenarios suggested by Ertel et al. (2012) to explain the phenomenon. An alternative scenario of enhanced stirring of the planetesimal disk by the companion star of HD 3003 has been proposed.

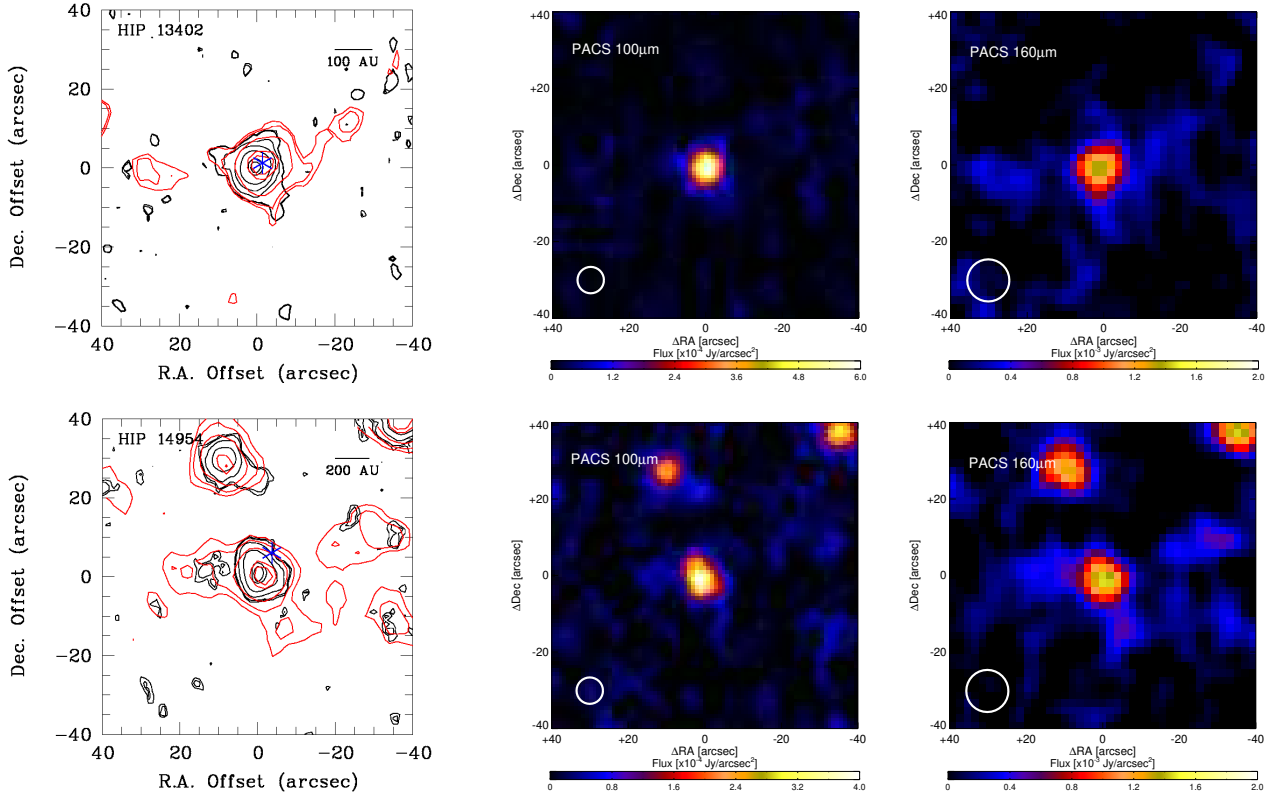


Fig. 10. Contours plots (left) and PACS 100 μm (middle) and 160 μm (right) images of two resolved debris disc stars. The identification of the stars are given in the upper-left corner of the contour plots. Position (0,0) refers to the 100 μm peak. The optical position of the stars with respect to the 100 μm peak is indicated by a “star” symbol. North is up and East to the left. Black contours correspond to 100 μm and red contours to 160 μm . HIP 13402: contours are 5%, 10%, 20%, 40%, 80%, 90% of the peak (100 μm), and 10%, 20%, 40%, 80%, 90% of the peak (160 μm). HIP 14954: contours are 10%, 20%, 40%, 80%, 90% of the peak at both bands. For both objects the lowest contour corresponds to 3σ .

7.2.6. Short description of individual objects

As it has already been pointed out, a detailed description of individual stars or groups of stars is beyond the scope of this paper. Detailed observational and/or modelling analysis of some sources have been the subject of previous DUNES works (papers already mentioned), and there are some more papers in preparation. However, in order to partly illustrate here the achieved results, we present a brief description together with the *Herschel* images and contour plots of HIP 13402 and HIP 14954 (Figure 10), two stars associated with resolved emission. The SEDs of these stars are included in Figure E.1.

HIP 13402. This K1 V star is located at a distance of 10.35 pc and is one of the youngest stars in our sample, $\sim 130 - 400$ Myr (Table 4). Previously identified as a debris disc based on the 70 μm *Spitzer* flux (Trilling et al. 2008), the excess is clearly present at 100 and 160 μm but it has a modest fractional luminosity of the dust. The star appears point-like in the 100 μm *Herschel* PACS image but slightly extended at 160 μm , with an observed size $12''.7 \times 11''.4$ (Figure 10). A quadratic subtraction of the stellar PSF gives an intrinsic size of $5''.4 \times 2''.6$, which corresponds to a projected semi-major axis of 28 AU, and therefore slightly larger than the black body radius (Table 14).

HIP 14954. This F8 star is located at a distance of 22.58 pc and is one of the debris discs preserved in the DUNES sample because it was already identified as such with *Spitzer*. The star hosts a gas giant exoplanet and also is the primary component of a physical binary. The age is not well constrained and is in the

range of $\sim 1 - 5.7$ Gyr. The fractional luminosity of the dust is among the modest values of our debris disc sample (Table 14).

8. Discussion

There are many works in the literature searching for potential correlations between the debris disc characteristics and the main properties of their associated stars -like metallicity, spectral type, or age-, the presence of exoplanets around the stars or if the stars are multiple systems (e.g. Habing et al. 2001; Rieke et al. 2005; Beichman et al. 2006; Trilling et al. 2008; Bryden et al. 2009; Rodriguez & Zuckerman 2012). This search is motivated because it might provide helpful hints to deepen in the knowledge of the conditions for the formation and evolution of planetary systems. In the following we revisit these analyses in view of the DUNES discs.

8.1. Debris discs/stellar metallicity

There exists a well established relationship between a high metallicity in solar-type stars and the incidence of extrasolar giant planets orbiting around them (e.g. Santos et al. 2004; Fischer & Valenti 2005), although such trend is not valid in the case of low mass planets, $M_p \lesssim 30 M_\oplus$ (e.g. Ghezzi et al. 2010; Mayor et al. 2011). In the case of debris disc stars, the results from various works do not reveal any correlation between the presence of discs and the metallicity of the stars (e.g. Bryden et al. 2006; Trilling et al. 2008; Moór et al. 2011). The most recent and, to our knowledge, comprehensive study on this issue has

been carried out by Maldonado et al. (2012) who, based on a set of homogeneously determined stellar parameters, analysed the metallicity distribution of different samples of stars. These samples included one of 107 solar-type stars with only debris discs and a control sample of stars without known debris discs and planets. They found that both samples have similar metallicity distributions, but there is a hint pointing out to a deficit of stars with discs at low metallicities or, in other words, stars with discs are slightly more metal rich than stars without discs (Figures 3 and 7 of Maldonado et al. 2012). We have repeated this analysis for the DUNES stars, differentiating those with no detected disc emission and those with associated discs. We have removed from both groups the stars with known exoplanets in order to avoid a potential contamination. The average $[\text{Fe}/\text{H}]$ for the debris disc stars (26 objects) is -0.10 ± 0.18 and a median of -0.09 , while for the non-excess stars the corresponding values are -0.15 ± 0.29 and -0.13 , respectively. Thus, both metallicity distributions are practically undistinguishable. More conclusive statements require further data, in particular concerning the incidence of low-mass planets in debris discs systems, to confirm or unconfirm the mentioned hint, which might shed light on the conditions to form low mass planet and/or planetesimal systems (e.g. Bryden et al. 2006; Greaves et al. 2007; Moro-Martín et al. 2007, Marshall et al. 2013, in preparation; Moro-Martín et al. 2013, in preparation).

8.2. Disc properties/spectral types and bolometric luminosities

Figure 11 (top and middle rows) shows plots of the fractional luminosity of the dust, the black body radius and temperature versus the effective temperature and the bolometric luminosity of the stars. The dust parameters present a large scatter and the plots indicate that none of them are correlated with the effective temperatures and luminosities of the stars, as corroborated by Pearson or Spearman correlation tests. Average values of L_d/L_\star , T_d and R_d grouping the stars by their F, G and K spectral types agree within the high uncertainties involving these parameters. The only parameter that might be weakly correlated with the stars' spectral types is the estimated average black body radius, which might present a decrease with the spectral type: $\langle R_d \rangle = 79 \pm 74$ AU for the F-type stars, 53 ± 54 AU for the G-type, and 28 ± 16 AU for the K-type stars. The lack of a correlation between the fractional luminosity of the dust and spectral type is also seen in *Spitzer* studies (e.g. Trilling et al. 2008). We further note that, excluding η^1 Eri (HIP 7978), the range of L_d/L_\star does not change much, although the disc detectability changes with the spectral type (Figure 8). We also note the fact that the dust temperature does not change with the stars' spectral type is because the dust is located on average at decreasing distances for the later stellar spectral types. Although the relative values provided by the simple black body approach might be useful (Wyatt 2008) to provide a basic view of the discs, it might be misleading because realistic grain properties are not taken into account. A firm interpretation of our debris disc properties and their relation with the stars' characteristics requires detailed modelling, which is beyond the scope of this work.

8.3. Debris discs/stellar ages

Stellar age is one of the main basic stellar quantities but at the same time of the most difficult to reliably determine for main-sequence solar-type field stars. The theoretical Hertzsprung-

Russell diagram is not very useful since isochrones pile-up for these spectral types. There is a handful of age diagnostics used as proxies (Mamajek & Hillenbrand 2008), but they can give conflicting results. However, the use of consistent age estimates circumvent this problem, at least partly (e.g. Rieke et al. 2005). From IRAS, ISO, and *Spitzer* studies it is known that debris discs persist around solar-type stars through very long timescales (Habing et al. 2001; Decin et al. 2003; Moór et al. 2006; Hillenbrand et al. 2008). The rate of debris discs and their dust luminosity seem to be relatively large up to ages ≤ 400 -500 Myr. For older stars, there is a small but not quite obvious decline up to ages of several Gyr (Trilling et al. 2008; Wyatt 2008). For all ages, the scatter is large.

Figure 11 shows in the bottom panels the dust fractional luminosity, the black body radius and temperature of the excess sources as a function of the stellar ages. We have used our own reduced spectra (Martínez-Arnáiz et al. 2010; Maldonado et al. 2010, 2012) to estimate ages in a consistent manner using the $\text{Ca II } R'_{\text{HK}}$ activity index (Mamajek & Hillenbrand 2008). Again there is a large scatter in L_d/L_\star for the stars in the sample, in particular for ages larger than ~ 3 Gyr where the bulk of the stars is concentrated. With respect to R_d and T_d , although the values present a scatter, the plots suggest a weak correlation of R_d and an anticorrelation of T_d with the stellar age. These trends hold for the FGK stars as a whole and individually for each F, G and K spectral types. In fact, a Pearson correlation test shows that the probability of R_d and T_d to be correlated with the age of all FGK debris disc stars are $\sim 97\%$ and larger than 99% , respectively. The apparent correlation between R_d and stellar age might be a hint for dynamical inward-out stirring of debris discs.

Table 16. Multiplicity of the excess sources. The separation refers to the angular distance to the closest identified companion. Column 4 with the black body radius of the dust is included with the purpose of a direct comparison. The column "Status" informs if the stars are true physical systems (Y), projected but no true binaries (N) or lack of sufficient information (?).

HIP	Separation	Proj. dist. (AU)	R_d (AU)	Status
171	0'83	10.1	≥ 97.1	Y
544				?
13402				?
14954	3'3	74.5	95.0	Y
15371	310''	3729	47.7	Y
29271	3'05			?
32480	36'2			N
49908	165''			N
51459	120''	1534	38.6	Y
65721	286'4			N
72848		0.52	34.2	Y
92043	12'6			?
107350	43'2	795	8.1	Y
107649	55''			N
114948				?

8.4. Debris discs/stellar multiplicity

The number of DUNES stars with an entry in the catalogues of binary and multiple stars CCDM (Catalog of Components of Double and Multiple Stars), WDS (Washington Double Star Catalog, Mason et al. 2011, version 2012), and SB9 (The 9th Catalogue of Spectroscopic Binary Orbits, Pourbaix et al. 2004,

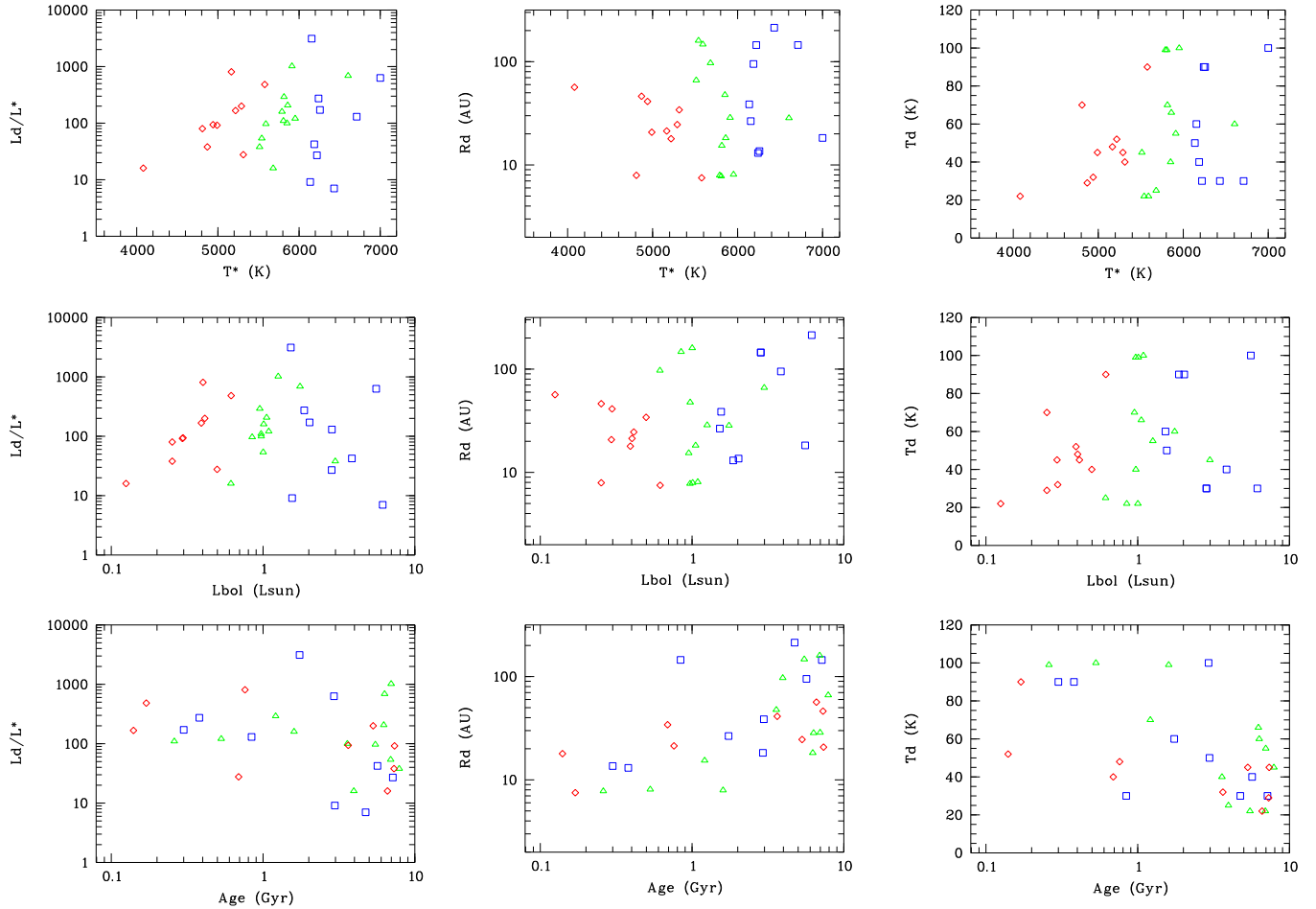


Fig. 11. Dust properties versus stellar effective temperature, bolometric luminosity and ages (based on the own Ca II activity index). Blue squares: F-type stars; green triangles: G-type stars; red diamonds: K-type stars. Units of the fractional luminosity of the dust are 10^{-7} .

version 2012) is 83 which represents $\sim 62\%$ of the sample. Not all entries correspond to real multiple systems. Out of these 83 entries, 15 correspond to stars identified as excess sources. Table 16 lists these stars, where the angular and linear distances with the closest companions are given for the cases where such information is available. In the last column on that table, the stars with true identified physical companions are given. This association is based on the proper motions and distances for HIP 14954, HIP 15371, HIP 51459. The stars HIP 171 and HIP 72848 are spectroscopy binaries with well determined orbital parameters (Bach et al. 2009; Halbwegs et al. 2003; Bonavita & Desidera 2007). HIP 107350 is accompanied by a substellar object with a mass in the brown dwarf regime (Luhman et al. 2007). HIP 29271 has a companion candidate (Eggenberger et al. 2007) but no further information. The optical companions of HIP 32480, HIP 49908, HIP 65721 and HIP 107649 have proper motions very different from the associated stars, so that they most likely are no real physical companions. There is no information to our knowledge, beyond the entry in one of the mentioned catalogues, for HIP 544, HIP 13402 and HIP 114948. As a summary, we can firmly identify 6 multiple systems out of 31 debris disc stars. This implies a rate of $\sim 20\%$, close to the one found by Rodriguez & Zuckerman (2012). Concerning the stellar or dust properties, the binary stars do not have any significant trend. We note that our numbers are not statistically significant enough to confirm or deny the claim by Rodriguez & Zuckerman (2012) of a lower

fractional disc luminosity for multiple systems than for single stars.

The comparison of the binary separation and the location of the dust (columns 3 and 4 of Table 16) is informative to assess if the dust resides in stable orbits. The discs around HIP 15371, HIP 51459 and HIP 107350 are clearly circumstellar since all the binary systems are very wide, while the discs around HIP 171 and HIP 7248 are circumbinary. These discs are located in stable orbits (e.g. Trilling et al. 2007; Rodriguez & Zuckerman 2012, for a comparison with other debris discs). The only questionable case is HIP 14954, where the black body radius and binary separation are similar and place the dust in an unstable location (Rodriguez & Zuckerman 2012). In order to assess stability issues of the debris discs versus the binarity of the stars, a specific study using realistic grain properties informing on plausible dust locations and temperatures is required.

8.5. Debris discs/planets

The number of known stars hosting exoplanets in the DUNES sample is 21. This figure includes HIP 107350 with a companion of mass $M_p = 16 M_J$, i.e., in the brown dwarf mass regime although it is listed in the Extrasolar Planets Encyclopaedia (<http://exoplanet.eu>). Six of these stars - HIP 7978, HIP 14954, HIP 27887, HIP 65721, HIP 107350, and HIP 109378 - have debris disc detected with *Herschel*. A further star, HIP 40693 has a warm disc (Beichman et al. 2005) but no excess in our

images. HIP 27887 and HIP 109378 are new debris disc detections by *Herschel*. If we consider the 20 pc DUNES sample, the number of stars hosting planets is 16, out of which 4 have debris discs (HIP 107350 is not included). Thus, the incidence rate of debris discs among exoplanet hosts is $25\% \pm 5\%$, i.e., only marginally larger than the fraction of discs around stars irrespective of whether they host a planet. HIP 7978, HIP 107350 and HIP 109378 have been studied by Liseau et al. (2010), Ertel et al. (2012a) and Eiroa et al. (2011), respectively. All DUNES and DEBRIS stars hosting exoplanets, including the disc non-detections, currently are the subject of a detailed treatment in two papers in preparation (Marshall et al., and Moro-Martín et al.).

9. Summary and conclusions

The purpose of this paper has been to present the observational results of the *Herschel* Open Time Key Project DUNES. The stellar sample consisted of 124 main-sequence, nearby (distances less than 20 pc), solar-type FGK stars, plus 9 stars with previously known debris discs or exoplanets, located at distances between 20 and 25 pc. Infrared excesses have been detected around a total of 31 stars out of the 133 stars and 25 stars out of the 124 stars in the 20 pc subsample. This represents a total increase of 10 new debris discs with respect to the ones previously known in the whole sample, and an increase in the incidence of debris discs in the 20 pc subsample from $12.1\% \pm 5\%$ to $20.2\% \pm 2\%$, i.e., around 1.7 times larger. The gain in incidence rate varies with the spectral type, being larger for the K-type stars. The achieved mean sensitivity is a function of stellar spectral type and distance, and the 3σ mean upper limit of the fractional luminosity of the dust for non-excess sources is $L_d/L_\star \sim 2.0 \times 10^{-6}$, with the lowest values $L_d/L_\star \lesssim 4.0 \times 10^{-7}$ corresponding to the closest stars. This is a gain of around one order of magnitude against the detection limit of *Spitzer*. Among the debris disc stars, a few of them show L_d/L_\star , a few times larger than the EKB value, albeit these disks are larger and colder than the predicted EKB dust disk.

The number of stars with spatially resolved emission is 16, which is a rate of 52% among the identified debris discs, and a huge gain with respect to the previously known resolved sources (3 objects). In addition, few sources show excess emission at $160 \mu\text{m}$ and very faint or no excess at $100 \mu\text{m}$ which is attributed to a new class of cold and faint debris discs. Although it cannot be excluded that some of these sources suffer from coincidental alignment with background galaxies, the probability that some of these cold disc candidates are true debris discs is very large. In addition, we have found that some discs show far-IR spectral indexes steeper than the black body Rayleigh-Jeans index. Both types of cold and steep-SED debris discs cannot easily be accommodated to the classical equilibrium collisional cascade scenario of debris discs.

An analysis of the debris disc parameters with stellar properties shows a weak trend of a correlation of the black body dust radii (the location of the dust) and an anticorrelation of the dust temperatures with the stellar age. This trend holds for all FGK spectral types as a whole, and for each F, G and K spectral types separately. No other correlation is found with the (possible) exception of a hint showing a decrease of the average black body dust radii from the F to the K spectral type stars. In-depth observational and modelling analysis of the DUNES debris discs will be published elsewhere.

The DUNES survey results provide a legacy value useful to the broad community, accomplishing in that way one of the rules for *Herschel* Key Programmes.

Acknowledgements. C. Eiroa, J. Maldonado, J. P. Marshall, G. Meeus and B. Montesinos were supported by the Spanish grants AYA2008-01727 and AYA2011-26202 A. Bayo was partly supported by the Marie Curie Actions of the European Commission (FT7-COFUND). J. Sanz was supported by Spanish grants AYA2008-02038 and AYA2011-30147-C03-03. A. V. Krivov and T. Löhne acknowledge support by the German DFG, grants Kr 2164/10-1 and Lo 1715/1-1. NASA support for this work (D. Ardila, Ch. Beichman, G. Bryden, W. Danchi, A. Roberge, K. Stapelfeldt) was provided through an award issued by JPL/Caltech.

References

- Allen, D. A. & Cragg, T. A. 1983, MNRAS, 203, 777
 Augereau, J. C., Nelson, R. P., Lagrange, A. M., Papaloizou, J. C. B., & Mouillet, D. 2001, A&A, 370, 447
 Aumann, H. H., Beichman, C. A., Gillett, F. C., et al. 1984, ApJ, 278, L23
 Aumann, H. H. & Probst, R. G. 1991, ApJ, 368, 264
 Avrett, E. H. 2003, in Astronomical Society of the Pacific Conference Series, Vol. 286, Current Theoretical Models and Future High Resolution Solar Observations: Preparing for ATST, ed. A. A. Pevtsov & H. Uitenbroek, 419
 Bach, K., Lee, J., Demarque, P., & Kim, Y.-C. 2009, ApJ, 703, 362
 Backman, D. E., Dasgupta, A., & Stencel, R. E. 1995, ApJ, 450, L35
 Backman, D. E. & Paresce, F. 1993, in Protostars and Planets III, ed. E. H. Levy & J. I. Lunine, 1253–1304
 Bakos, G. Á., Sahu, K. C., & Németh, P. 2002, ApJS, 141, 187
 Beichman, C. A., Bryden, G., Gautier, T. N., et al. 2005, ApJ, 626, 1061
 Beichman, C. A., Bryden, G., Stapelfeldt, K. R., et al. 2006, ApJ, 652, 1674
 Beichman, C. A., Lisse, C. M., Tanner, A. M., et al. 2011, ApJ, 743, 85
 Berta, S., Magnelli, B., Lutz, D., et al. 2010, A&A, 518, L30
 Berta, S., Magnelli, B., Nordon, R., et al. 2011, A&A, 532, A49
 Bertone, E., Buzzoni, A., Chávez, M., & Rodríguez-Merino, L. H. 2004, AJ, 128, 829
 Bonavita, M. & Desidera, S. 2007, A&A, 468, 721
 Brott, I. & Hauschildt, P. H. 2005, in ESA Special Publication, Vol. 576, The Three-Dimensional Universe with Gaia, ed. C. Turon, K. S. O’Flaherty, & M. A. C. Perryman, 565
 Bryden, G., Beichman, C. A., Carpenter, J. M., et al. 2009, ApJ, 705, 1226
 Bryden, G., Beichman, C. A., Trilling, D. E., et al. 2006, ApJ, 636, 1098
 Carter, B. S. 1990, MNRAS, 242, 1
 Castelli, F. & Kurucz, R. L. 2003, in IAU Symposium, Vol. 210, Modelling of Stellar Atmospheres, ed. N. Piskunov, W. W. Weiss, & D. F. Gray, 20P
 Cox, A. N. 2000, Allen’s astrophysical quantities
 Decin, G., Dominik, C., Waters, L. B. F. M., & Waelkens, C. 2003, ApJ, 598, 636
 Dohnanyi, J. S. 1969, J. Geophys. Res., 74, 2531
 Dommanget, J. & Nys, O. 2002, VizieR Online Data Catalog, 1274, 0
 Donaldson, J. K., Roberge, A., Chen, C. H., et al. 2012, ApJ, 753, 147
 Eggenberger, A., Udry, S., Chauvin, G., et al. 2007, A&A, 474, 273
 Eggenberger, P., Miglio, A., Carrier, F., Fernandes, J., & Santos, N. C. 2008, A&A, 482, 631
 Eiroa, C., Fedele, D., Maldonado, J., et al. 2010, A&A, 518, L131
 Eiroa, C., Marshall, J. P., Mora, A., et al. 2011, A&A, 536, L4
 Elias, J. H., Frogel, J. A., Hyland, A. R., & Jones, T. J. 1983, AJ, 88, 1027
 Elias, J. H., Frogel, J. A., Matthews, K., & Neugebauer, G. 1982, AJ, 87, 1029
 Ertel, S., Wolf, S., Marshall, J. P., et al. 2012a, A&A, 541, A148
 Ertel, S., Wolf, S., Metchev, S., et al. 2011, A&A, 533, A132
 Ertel, S., Wolf, S., & Rodmann, J. 2012b, A&A, 544, A61
 ESA, ed. 1997, ESA Special Publication, Vol. 1200, The HIPPARCOS and TYCHO catalogues. Astrometric and photometric star catalogues derived from the ESA HIPPARCOS Space Astrometry Mission
 Fischer, D. A. & Valenti, J. 2005, ApJ, 622, 1102
 Flower, P. J. 1996, ApJ, 469, 355
 Fruchter, A. S. & Hook, R. N. 2002, PASP, 114, 144
 Fuhrmann, K. 2008, MNRAS, 384, 173
 Gautier, III, T. N., Rieke, G. H., Stansberry, J., et al. 2007, ApJ, 667, 527
 Ghezzi, L., Cunha, K., Smith, V. V., et al. 2010, ApJ, 720, 1290
 Glass, I. S. 1975, MNRAS, 171, 19P
 Gray, R. O., Corbally, C. J., Garrison, R. F., et al. 2006, AJ, 132, 161
 Gray, R. O., Corbally, C. J., Garrison, R. F., McFadden, M. T., & Robinson, P. E. 2003, AJ, 126, 2048
 Greaves, J. S., Fischer, D. A., Wyatt, M. C., Beichman, C. A., & Bryden, G. 2007, MNRAS, 378, L1
 Griffin, M. J., Abergel, A., Abreu, A., et al. 2010, A&A, 518, L3

- Gustafsson, B., Edvardsson, B., Eriksson, K., et al. 2008, *A&A*, 486, 951
- Habing, H. J., Dominik, C., Jourdain de Muizon, M., et al. 2001, *A&A*, 365, 545
- Halbwachs, J. L., Mayor, M., Udry, S., & Arenou, F. 2003, *A&A*, 397, 159
- Hillenbrand, L. A., Carpenter, J. M., Kim, J. S., et al. 2008, *ApJ*, 677, 630
- Holmberg, J., Nordström, B., & Andersen, J. 2009, *A&A*, 501, 941
- Jewitt, D., Moro-Martín, A., & Lacerda, P. 2009, *The Kuiper Belt and Other Debris Disks*, ed. H. A. Thronson, M. Stiavelli, & A. Tielens, 53
- Kennedy, G. M., Wyatt, M. C., Sibthorpe, B., et al. 2012, *MNRAS*, 426, 2115
- Koerner, D. W., Kim, S., Trilling, D. E., et al. 2010, *ApJ*, 710, L26
- Koornneef, J. 1983, *A&AS*, 51, 489
- Kóspál, Á., Ardila, D. R., Moór, A., & Ábrahám, P. 2009, *ApJ*, 700, L73
- Krivov, A. V. 2010, *Research in Astronomy and Astrophysics*, 10, 383
- Lagrange, A.-M., Bonnefoy, M., Chauvin, G., et al. 2010, *Science*, 329, 57
- Lawler, S. M., Beichman, C. A., Bryden, G., et al. 2009, *ApJ*, 705, 89
- Liseau, R., Eiroa, C., Fedele, D., et al. 2010, *A&A*, 518, L132
- Liseau, R., Montesinos, B., Olofsson, G., et al. 2013, *A&A*, 549, L7
- Löhne, T., Augereau, J.-C., Ertel, S., et al. 2012, *A&A*, 537, A110
- Luhman, K. L., Patten, B. M., Marengo, M., et al. 2007, *ApJ*, 654, 570
- Luyten, W. J. 1979, *LHS catalogue. A catalogue of stars with proper motions exceeding 0^o5 annually*
- Maldonado, J., Eiroa, C., Villaver, E., Montesinos, B., & Mora, A. 2012, *A&A*, 541, A40
- Maldonado, J., Martínez-Arnáiz, R. M., Eiroa, C., Montes, D., & Montesinos, B. 2010, *A&A*, 521, A12+
- Mamajek, E. E. & Hillenbrand, L. A. 2008, *ApJ*, 687, 1264
- Marshall, J. P., Löhne, T., Montesinos, B., et al. 2011, *A&A*, 529, A117
- Martínez-Arnáiz, R., Maldonado, J., Montes, D., Eiroa, C., & Montesinos, B. 2010, *A&A*, 520, A79+
- Mason, B. D., Wycoff, G. L., Hartkopf, W. I., Douglass, G. G., & Worley, C. E. 2011, *VizieR Online Data Catalog*, 1, 2026
- Matthews, B. C., Sibthorpe, B., Kennedy, G., et al. 2010, *A&A*, 518, L135
- Mayor, M., Marmier, M., Lovis, C., et al. 2011, *ArXiv e-prints*
- Moór, A., Ábrahám, P., Derekas, A., et al. 2006, *ApJ*, 644, 525
- Moór, A., Pascucci, I., Kóspál, Á., et al. 2011, *ApJS*, 193, 4
- Moro-Martín, A., Carpenter, J. M., Meyer, M. R., et al. 2007, *ApJ*, 658, 1312
- Moro-Martín, A. & Malhotra, R. 2005, *ApJ*, 633, 1150
- Mouillet, D., Larwood, J. D., Papaloizou, J. C. B., & Lagrange, A. M. 1997, *MNRAS*, 292, 896
- Mustill, A. J. & Wyatt, M. C. 2009, *MNRAS*, 399, 1403
- Ott, S. 2010, in *Astronomical Society of the Pacific Conference Series*, Vol. 434, *Astronomical Data Analysis Software and Systems XIX*, ed. Y. Mizumoto, K.-I. Morita, & M. Ohishi, 139
- Phillips, N. M., Greaves, J. S., Dent, W. R. F., et al. 2010, *MNRAS*, 403, 1089
- Pilbratt, G. L., Riedinger, J. R., Passvogel, T., et al. 2010, *A&A*, 518, L1
- Poglitsch, A., Waelkens, C., Geis, N., et al. 2010, *A&A*, 518, L2
- Pourbaix, D., Tokovinin, A. A., Batten, A. H., et al. 2004, *A&A*, 424, 727
- Quillen, A. C. & Thorndike, S. 2002, *ApJ*, 578, L149
- Rieke, G. H., Su, K. Y. L., Stansberry, J. A., et al. 2005, *ApJ*, 620, 1010
- Rodriguez, D. R. & Zuckerman, B. 2012, *ApJ*, 745, 147
- Santos, N. C., Israelian, G., & Mayor, M. 2004, *A&A*, 415, 1153
- Selby, M. J., Hepburn, I., Blackwell, D. E., et al. 1988, *A&AS*, 74, 127
- Sibthorpe, B., Ivison, R. J., Massey, R. J., et al. 2012, *MNRAS*, L3
- Skiff, B. A. 2009, *VizieR Online Data Catalog*, 1, 2023
- Smith, B. A. & Terrile, R. J. 1984, *Science*, 226, 1421
- Sousa, S. G., Santos, N. C., Mayor, M., et al. 2008, *A&A*, 487, 373
- Su, K. Y. L., Rieke, G. H., Stansberry, J. A., et al. 2006, *ApJ*, 653, 675
- Takeda, Y., Ohkubo, M., Sato, B., Kambe, E., & Sadakane, K. 2005, *PASJ*, 57, 27
- Tanner, A., Beichman, C., Bryden, G., Lisse, C., & Lawler, S. 2009, *ApJ*, 704, 109
- Thebault, P., Kral, Q., & Ertel, S. 2012, *A&A*, 547, A92
- Trilling, D. E., Bryden, G., Beichman, C. A., et al. 2008, *ApJ*, 674, 1086
- Trilling, D. E., Stansberry, J. A., Stapelfeldt, K. R., et al. 2007, *ApJ*, 658, 1289
- Valenti, J. A. & Fischer, D. A. 2005, *ApJS*, 159, 141
- van Leeuwen, F. 2007, *A&A*, 474, 653
- van Leeuwen, F. 2008, *VizieR Online Data Catalog*, 1311, 0
- Vitense, C., Krivov, A. V., Kobayashi, H., & Löhne, T. 2012, *A&A*, 540, A30
- Vitense, C., Krivov, A. V., & Löhne, T. 2010, *A&A*, 520, A32+
- Wright, C. O., Egan, M. P., Kraemer, K. E., & Price, S. D. 2003, *AJ*, 125, 359
- Wyatt, M. C. 2008, *ARA&A*, 46, 339
- Wyatt, M. C., Kennedy, G., Sibthorpe, B., et al. 2012, *MNRAS*, 424, 1206
- ³ Centro de Astrobiología (INTA-CSIC), ESAC Campus, P.O.Box 78, E-28691 Villanueva de la Cañada, Madrid, Spain
- ⁴ Institut d'Astrophysique et de Gophysique, Université de Lige, 17 Alle du Six Aot, B-4000 Sart Tilman, Belgium
- ⁵ UJF-Grenoble 1 / CNRS-INSU, Institut de Planétologie et d'Astrophysique de Grenoble (IPAG), UMR 5274, Grenoble, F-38041, France
- ⁶ European Space Observatory, Alonso de Cordova 3107, Vitacura Casilla 19001, Santiago 19, Chile
- ⁷ Max-Planck Institut für Astronomie, Königstuhl, 69117, Germany
- ⁸ Jet Propulsion Laboratory, California Institute of Technology, 4800 Oak Grove Drive, Pasadena, CA 91109, USA
- ⁹ NASA Goddard Space Flight Center, Exoplanets and Stellar Astrophysics, Code 667, Greenbelt, MD 20771, USA
- ¹⁰ Instituto Nacional de Astrofísica, Óptica y Electrónica, Luis Enrique Erro 1, Sta. Ma. Tonantzintla, Puebla, México
- ¹¹ ESA Astrophysics & Fundamental Physics Missions Division, ESTEC/SRE-SA, Keplerlaan 1, NL-2201 AZ Noordwijk, The Netherlands
- ¹² Astrophysikalisches Institut und Universitätssternwarte, Friedrich-Schiller-Universität, Schillergäßchen 2-3, 07745 Jena, Germany
- ¹³ Department of Earth and Space Sciences, Chalmers University of Technology, Onsala Space Observatory, Se-439 92 Onsala, Sweden
- ¹⁴ Georg-August-Universität Göttingen, Institut für Astrophysik, Friedrich-Hund-Platz 1, 37077 Göttingen, Germany
- ¹⁵ LESIA, Observatoire de Paris, 92195 Meudon France
- ¹⁶ Christian-Albrechts-Universität zu Kiel, Institut für Theoretische Physik und Astrophysik, Leibnizstr. 15, 24098 Kiel, Germany
- ¹⁷ NASA Herschel Science Center, California Institute of Technology, 1200 E. California Blvd., Pasadena, CA 91125, USA
- ¹⁸ NASA ExoPlanet Science Institute California Institute of Technology, 1200 E. California Blvd., Pasadena, CA 91125, USA
- ¹⁹ ISDEFE at ESAC, E-28691 Villanueva de la Cañada, Madrid, Spain
- ²⁰ Universidad Complutense de Madrid, Facultad de Ciencias Físicas, Dpt. Astrofísica, av. Complutense s/n. 28040 Madrid, Spain
- ²¹ Department of Astronomy, Stockholm University, AlbaNova University Center, Roslagstullsbacken 21, SE-106 91 Stockholm, Sweden
- ²² Steward Observatory, University of Arizona, 933 North Cherry Avenue, Tucson, AZ 85721, USA
- ²³ Rutherford Appleton Laboratory, Chilton OX11 0QX, UK
- ²⁴ Department of Physics and Astrophysics, Open University, Walton Hall, Milton Keynes MK7 6AA, UK
- ²⁵ Calar Alto Observatory, Centro Astronómico Hispano-Alemán, c/ Jesús Durbán Remón, 2-2, 04004, Almería, Spain
- ²⁶ Nagoya University, Japan.
- ²⁷ Max-Planck-Institut für Kernphysik, Saupfercheckweg 1, D-69117 Heidelberg, Germany
- ²⁸ Kapteyn Astronomical Institute, Postbus 800, 9700 AV Groningen, The Netherlands
- ²⁹ Herschel Science Center, ESAC/ESA, P.O. BOX 78, 28691 Villanueva de la Cañada, Madrid, Spain
- ³⁰ Observatoire de la Côte d'Azur, Boulevard de l'Observatoire, B.P. 4229, 06304 Nice Cedex 4, France.
- ³¹ Institute of Space and Astronautical Science (ISAS), Japan Aerospace Exploration Agency (JAXA), 3-1-1, Yoshinodai, Chuo-ku, Sagami-hara, Kanagawa, 252-5210, Japan
- ³² Institut de Ciències de l'Espai (CSIC-IEEC), Campus UAB, Facultat de Ciències, Torre C5, parell, 2a pl., E-08193 Bellaterra, Barcelona, Spain
- ³³ ESA-ESAC, Science Archives Team, P-O- Box 78, E-28691 Villanueva de la Cañada, Madrid, Spain

¹ Universidad Autónoma de Madrid, Dpto. Física Teórica, Módulo 15, Facultad de Ciencias, Campus de Cantoblanco, E-28049 Madrid, Spain

² ESA-ESAC Gaia SOC. P.O. Box 78 E-28691 Villanueva de la Cañada, Madrid, Spain

Appendix A: DUNES Virtual Observatory tool

The achievement of the DUNES objectives requires a detailed knowledge of the properties and environment of the targets to be studied. There exists a huge amount of astrophysical data and information about the DUNES objects, distributed in a number of archives and services. Gathering information in a wide variety of types and formats from a large number of heterogeneous astronomical data services is a tedious, very time consuming task even for a modest data set. With this aim we have developed a Virtual Observatory⁹ (VO) application for accessing, visualizing and downloading the information on DUNES targets available in astronomical archives and services. Given a list of objects, identified by their names or coordinates, a real-time exploration of Vizier¹⁰ using VO protocols is performed to gather photometric data as well as physical parameters. This information can be complemented with searches of images, spectra and catalogues in all the Virtual Observatory services. Moreover, ad hoc access to other non VO-compliant services of interest (like NStED or Spitzer/FEPS) is also provided. The obtained information can be downloaded in ASCII, VOTable (standard format for tabular data in the Virtual Observatory) or HTML format. For heavy queries, the tool implements a batch mode informing the user via e-mail when the search is complete. The message includes a link to the data through which the information can be downloaded.

In addition, one of the goals of the DUNES consortium is to provide the astronomical community with a legacy VO-compliant archive, as also requested by rules of the *Herschel* OTKPs. The DUNES Archive System¹¹ is designed to ensure that other research groups gain easy access to both *Herschel* reduced data and ancillary data (photometry and physical parameters gathered from VO services), as well as to the DUNES VO discovery tool, the DUNES project web page as well as to a section including news on the archive. A HelpDesk to pose questions to archive staff is also available.

Appendix B: Stellar fluxes and parameters

Table 3, with several subtables, presents the magnitudes and fluxes of the DUNES stars which have been used to trace their spectral energy distributions. Optical, near-IR, WISE, AKARI, IRAS and *Spitzer* data are included.

Table 4 gives some relevant parameters of the stars. T_{eff} , $\log g$ and $[\text{Fe}/\text{H}]$ are average values of photometric and spectroscopic estimates mainly from Gray et al. (2003); Santos et al. (2004); Takeda et al. (2005); Valenti & Fischer (2005); Gray et al. (2006); Fuhrmann (2008); Sousa et al. (2008); Holmberg et al. (2009). Rotational velocity values are taken from Martínez-Arnáiz et al. (2010). Bolometric luminosities and stellar radii have been estimated from the absolute magnitudes and bolometric corrections using the measurements by Flower (1996). The activity index $\log R'_{\text{HK}}$ has been taken from Martínez-Arnáiz et al. (2010) while we have derived the X-ray luminosities based on ROSAT, XMM and *Chandra* data. The table also provides ages based on the $\log R'_{\text{HK}}$ index and on the X-Ray luminosities as estimated by Maldonado et al. (2010). There is a wide range of age estimates in the literature using different tracers for the DUNES stars. Stellar ages of our targets are difficult to estimate

⁹ The VO is a project designed to provided the astronomical community with the data access and the research tools necessary to enable the exploration of the digital, multi-wavelength universe resident in the astronomical data archives. <http://www.ivoa.net>

¹⁰ http://vizier.u-strasbg.fr/c_gi-bin/VizieR

¹¹ <http://sdc.cab.inta-csic.es/dunes>

on the basis of isochrones given that the stars are located on the main-sequence (see Figure 2) and that they are sensitive to T_{eff} and metallicity (Holmberg et al. 2009). Thus, we have opted to give in Table 4 the age estimates based on our own coherent data set and procedure.

Appendix C: Prediction of photospheric fluxes at the PACS and SPIRE wavelengths.

C.1. Models

The behaviour of three families of model atmospheres was studied in order to choose the best option for the photospheric work of the project: PHOENIX/GAIA (Brott & Hauschildt, 2005), ATLAS9 (Castelli & Kurucz 2003) and MARCS (Gustafsson et al. 2008). It was found that for $T_{\text{eff}} \geq 5000$ K the three sets of models are virtually identical. In the interval 4000–5000 K the models start to show some differences which are more pronounced towards lower temperatures and shorter wavelengths, the models being identical for $\lambda > 4 \mu\text{m}$. For lower temperatures –only seven DUNES stars have T_{eff} below 4000 K– the three sets of models present larger discrepancies, with ATLAS9 being more different when compared with the other two families.

The PHOENIX/GAIA set of models was finally chosen because of its finer grid in effective temperatures, sampling of the individual model spectra and overall behaviour. The models were computed in LTE, the opacity treated with the opacity sampling formalism, and more than 300 million lines were included. The synthetic spectra have a variable amount of wavelength points, between 50,000 and 55,000, cover the interval 0.001–50 μm , v_{turb} was set to 2 km/s, the mixing length parameter is 1.5 and the geometry is plane parallel, or spherical in those cases where that one is not correct.

Due to their extremely large resolution, the synthetic spectra were smoothed with a gaussian filter with FWHM=0.005 after taking the decimal logarithm of the wavelengths in angstroms. Following that, the wavelength scale was put back in physical units.

A grid of 1980 spectra (55 temperatures \times 6 gravities \times 6 metallicities) was available. The ranges covered are 3000 K $< T_{\text{eff}} < 9800$ K, $3.0 < \log g < 5.5$ (step 0.5 dex) and $-2.0 < [\text{Fe}/\text{H}] < +0.5$ (step 0.5 dex).

In general, the synthetic spectrum for a given star is not contained in the grid, therefore, an interpolation in three dimensions had to be done. Since the PHOENIX/GAIA models only run up to $\lambda = 40 \mu\text{m}$, an extension up to 4 mm using the Rayleigh-Jeans approximation was attached to the original model.

C.2. Normalization of the models to the observed SED

The normalization of the model photosphere to the observed SED was done using the procedure outlined by Bertone et al. (2004). The monochromatic fluxes of the SED, $s(\lambda)$ (in units of Jy), were compared with those of the synthetic model, $m(\lambda)$ (in the same units), at the corresponding wavelengths, deriving a residual function:

$$X(\lambda_i) = \ln s(\lambda_i) - \ln m(\lambda_i) + k \quad (\text{C.1})$$

The offset constant is such that

$$\sum_i X(\lambda_i) = 0 \quad (\text{C.2})$$

so $k = \langle \ln m(\lambda) - \ln s(\lambda) \rangle$.

Five subsets of the full SED were chosen to carry out five normalizations, namely, VI+nIR, BVI+nIR, VI+nIR+WISE, nIR+WISE and VI+nIR+WISE. The near infrared photometry (nIR) consists of 2MASS JHK_s (only magnitudes with quality flags “A” or “B” were considered), plus additional JHKL points, when available. WISE band W1 (3.35 μm) was used in most of the cases despite of being nominally saturated¹² because PSF photometry was carried out on the images and therefore the values provided in the all-sky release turned out to be usable (Stapelfeldt, private communication), only the brightest targets showed unacceptable values of W1 magnitudes; WISE W2 (4.60 μm) photometry was never used; its flux level, when looking at the SED as a whole, always deviates from the overall behaviour; WISE W3 (11.56 μm) was always used unless it was brighter than the saturation magnitude; WISE W4 (22.09 μm) was also always used unless the shape of the SED indicated that an excess could start around that wavelength.

Since each normalization was done with a different number of points (e.g. degrees of freedom), a reduced χ^2 was computed for each one in order to make a comparison of all of them. The selected normalization was that with the least reduced χ^2 and was used to predict the fluxes at the PACS and SPIRE wavelengths. The uncertainties in the individual photospheric fluxes were estimated by computing the total σ of the normalization, in logarithmic units; in this calculation the observed flux at each wavelength involved in the normalization process was compared with its corresponding predicted flux. The result is that the normalized model $\log S(\lambda)$ can be allowed to move up and down a quantity $\pm\sigma$. That value of σ was then translated into individual –linear– uncertainties of the fluxes at the relevant *Herschel* wavelengths.

Appendix D: Spurious sources

There is a number of objects whose fluxes seemingly denote an excess, which can in a first instance be attributed to a circumstellar disc, but whose morphologies and surrounding fields suggest they are not true debris discs associated with the stars. Very likely, these stars are affected by coincidental alignment or contamination from a structured background. In the following, we briefly describe these cases and show their PACS images and contour plots in Figures D.1 and D.2. Table D.1 lists these sources together with their PACS and predicted photospheric fluxes. The significance of the “apparent” excesses is also given, as well as the *Spitzer* MIPS 70 μm fluxes.

HIP 29568. The 160 μm flux has a significance of $\chi_{160} = 3.00$ (Table D.1), being a cold disc candidate. However, the image shows a lot of background structure (Figure D.1) which makes the flux estimate doubtful.

HIP 38784. This is a faint star which apparently shows a small excess at 160 μm . However, reduced images from HIPE versions 7.2 (Figure D.1) and 4.2 are not quite consistent, as neither are the individual scans likely due to the faintness of the source.

HIP 40843. This star was identified by *Spitzer* as an excess source. However, the positional offset between the star and the peak of the PACS image is large. Both the 100 and 160 μm images are extended but practically in perpendicular directions (Figure D.1). The fluxes of the table correspond to the whole extended emission. However, given the position of the star and the different orientations at 100 and 160 μm , we consider it a case of coincidental alignment of a background galaxy. In fact, there is

a very faint, secondary 100 μm peak embedded in the extended emission. This peak is at the position α (2000.0) = 8:20:03.78, δ (2000.0) = 27:13:4.6, i.e., and offset of 1'4 wrt the optical positions on the star, and of 8'1 wrt the main 100 μm peak. A 2D gaussian fit supports the presence of two peaks.

HIP 71908. The star lies on top of an emission strip at both 100 and 160 μm (Fig D.2), which prevents us from estimating an enough accurate flux in the red band. This star is located at the galactic plane. The marginal 100 μm significance, $\chi_{100} = 3.13$, is likely not real.

HIP 85295. There is an offset between the 100 μm peak, which coincides with the optical position, and the 160 μm peak emission (Fig D.2). At this wavelength, the object seems to be formed by two different ones separated by $\sim 6''$. The western one is close to the 100 μm peak. Thus, the apparent excess emission at 160 μm is likely due to contamination by a background galaxy.

HIP 105312. The 100 μm peak agrees well with the optical position, but the 160 μm emission, which appears resolved, is displaced a bit towards the west. (Figure D.2).

HIP 113576. This is a case of a very clear offset between the 100 and the 160 μm emission, which likely falsifies the presence of an excess (Figure D.2).

Appendix E: SEDs of the excess sources

¹² http://wise2.ipac.caltech.edu/docs/release/allsky/expsup/sec6_3d.html

Table D.1. DUNES stars whose apparent excesses are very likely due to contamination by background galactic extended structures or extragalactic objects. PACS and predicted photospheric fluxes, and the significance of the measured apparent excesses are given. The last column gives *Spitzer* MIPS fluxes at 70 μm .

HIP	SpT	PACS70 (mJy)	S70 (mJy)	χ_{70}	PACS100 (mJy)	S100 (mJy)	χ_{100}	PACS160 (mJy)	S160 (mJy)	χ_{160}	MIPS70 (mJy)
29568	G5V		10.48 \pm 0.19		7.83 \pm 1.16	5.13 \pm 0.10	1.92	8.28 \pm 2.11	2.01 \pm 0.04	3.00	15.3 \pm 2.3
38784	G8V	8.66 \pm 2.65	9.47 \pm 0.10	-0.31	4.19 \pm 0.74	4.64 \pm 0.05	-0.61	5.98 \pm 1.28	1.81 \pm 0.02	3.26	10.6 \pm 3.0
40843	F6V		22.59 \pm 0.13		33.17 \pm 2.76	11.07 \pm 0.06	8.03	53.35 \pm 3.17	4.32 \pm 0.02	15.47	32.5 \pm 5.3
71908	F1Vp		68.58 \pm 4.16		38.54 \pm 1.58	33.60 \pm 2.04	3.13		13.13 \pm 0.80		
85295	K7V		21.14 \pm 0.46		12.94 \pm 1.12	10.36 \pm 0.22	2.30	14.15 \pm 3.29	4.05 \pm 0.09	3.07	13.8 \pm 4.6
105312	G5V	12.44 \pm 1.72	11.86 \pm 0.66	0.34	7.84 \pm 0.76	5.81 \pm 0.32	2.67	9.20 \pm 1.74	2.27 \pm 0.13	3.98	13.6 \pm 5.7
113576	K5/M0V		19.01 \pm 0.97		9.43 \pm 0.79	9.32 \pm 0.48	0.14	12.66 \pm 1.50	3.64 \pm 0.19	6.01	19.1 \pm 2.9

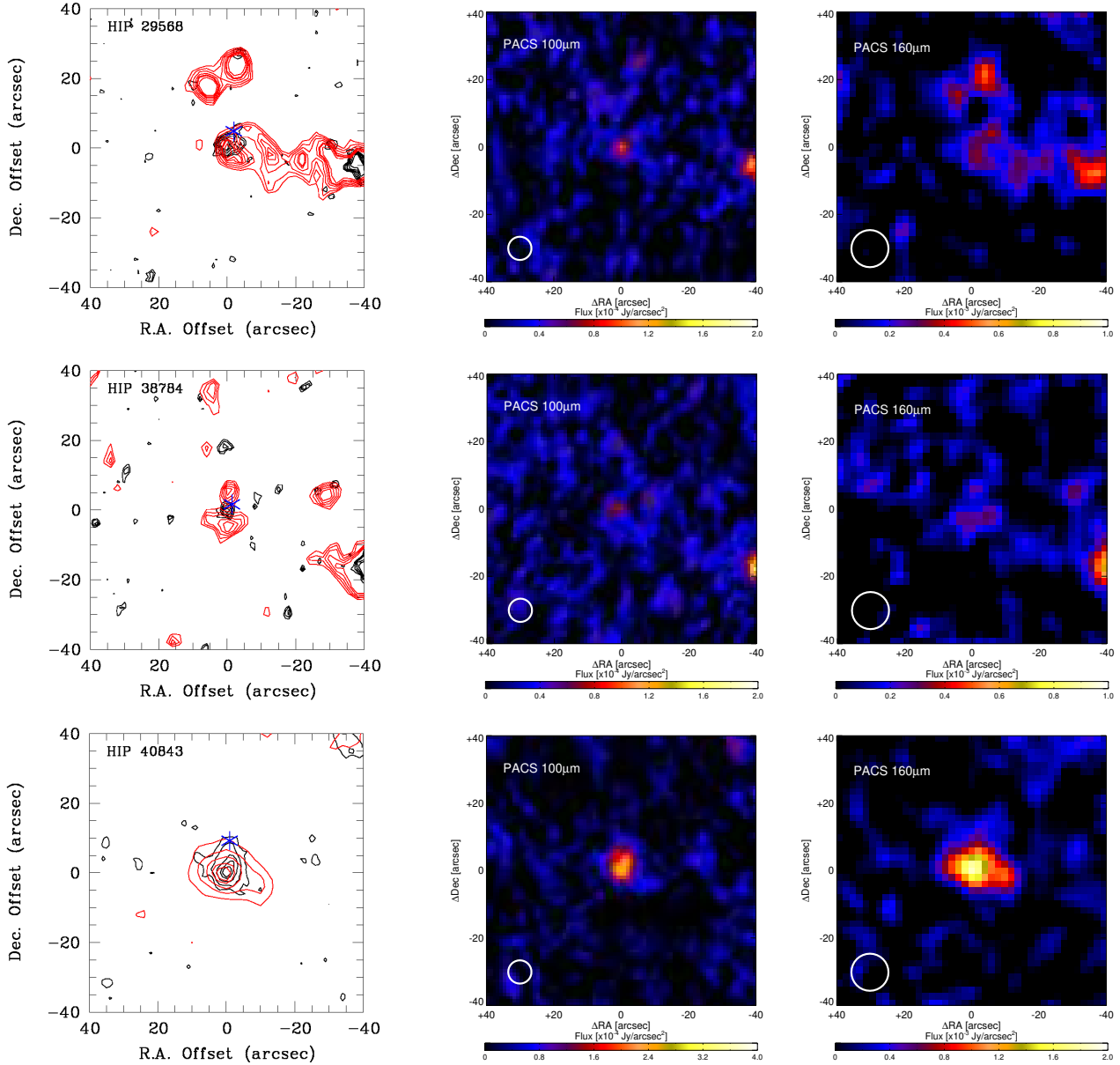


Fig. D.1. Contour plots (left) and PACS 100 μm (middle) and 160 μm (right) images of stars for which contamination impacts the apparent excesses of the stars. The identification of the stars are given in the upper-left corner of the contour plots. Position (0,0) refers to the 100 μm peak. The optical position of the stars with respect to the 100 μm peak is indicated by a “star” symbol. North is up and East to the left. Black contours correspond to 100 μm and red contours to 160 μm . HIP 29568: contours are 40%, 50%, 60%, 70%, 80%, 90% of the peak at both bands. HIP 38784: contours are 50%, 60%, 70%, 80%, 90% of the peak at both bands. HIP 40843: contours 20%, 40%, 60%, 80%, 90% of the peak at both bands.

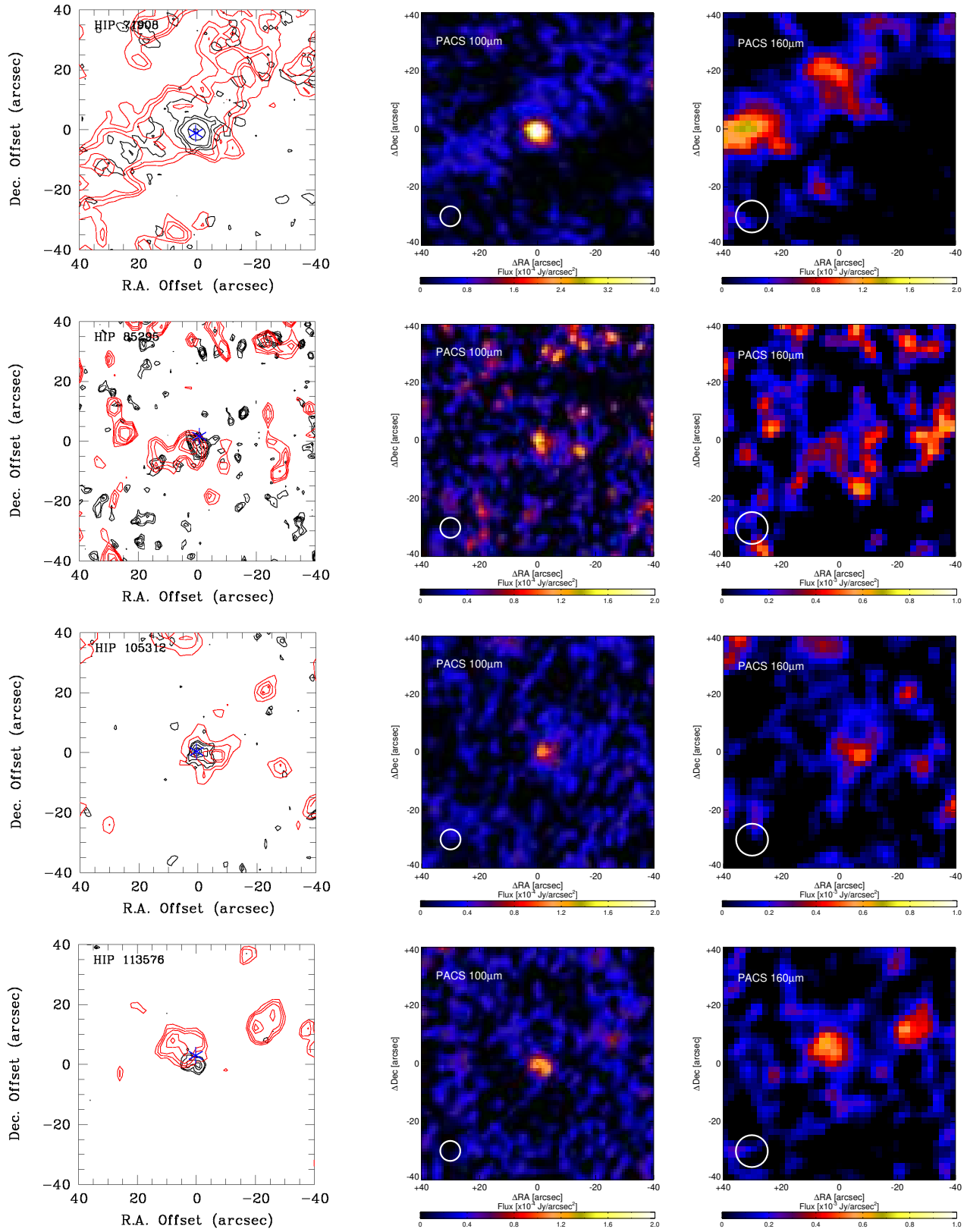


Fig. D.2. The same as D.1. In this case contours are 20%, 40%, 60%, 80%, 90% of the peak at both 100 and 160 μm bands for all the images.

Fig. E.1. SEDs of DUNES stars with excesses.

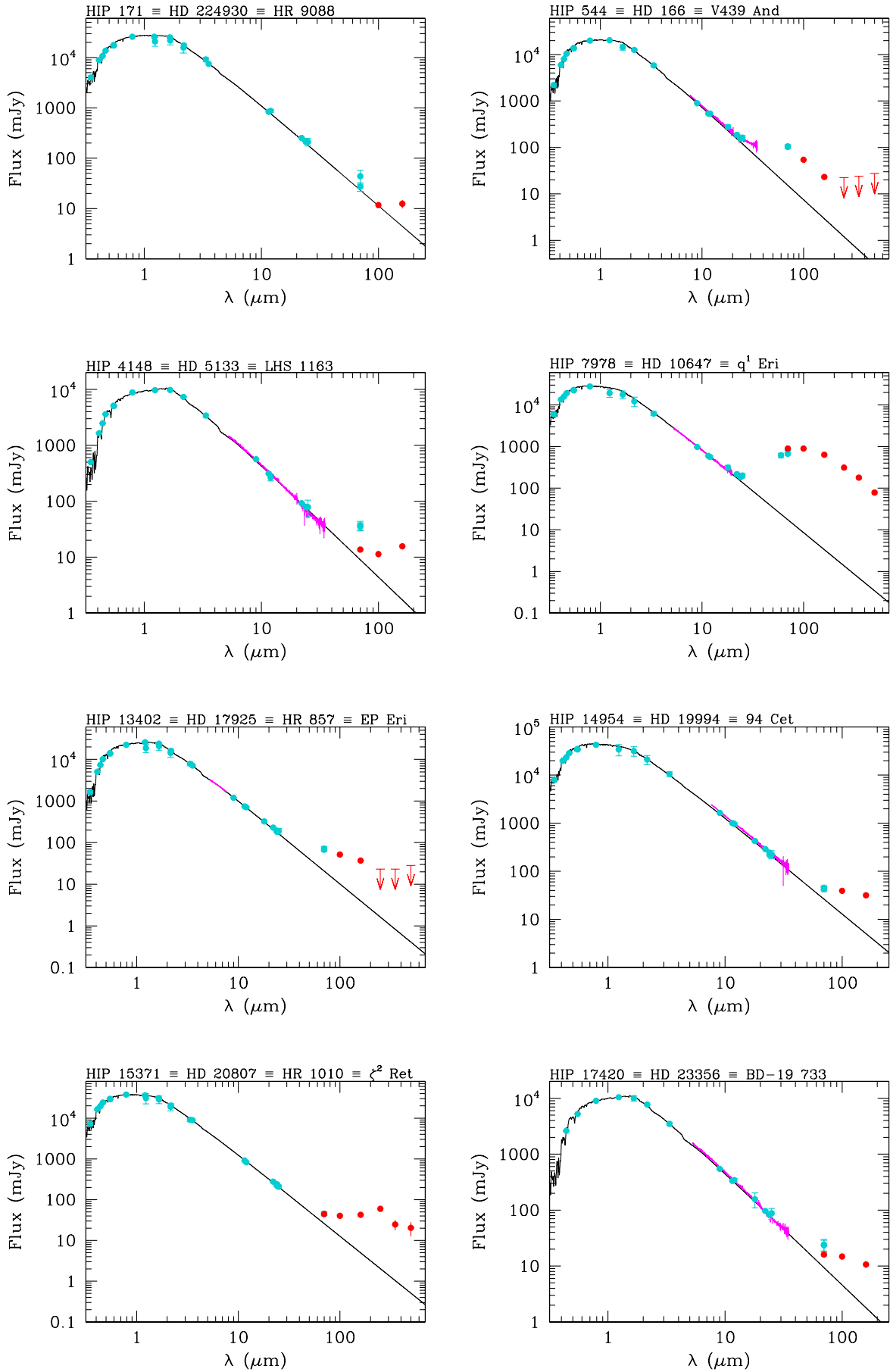


Fig. E.1. SEDs of DUNES stars with excesses (continued).

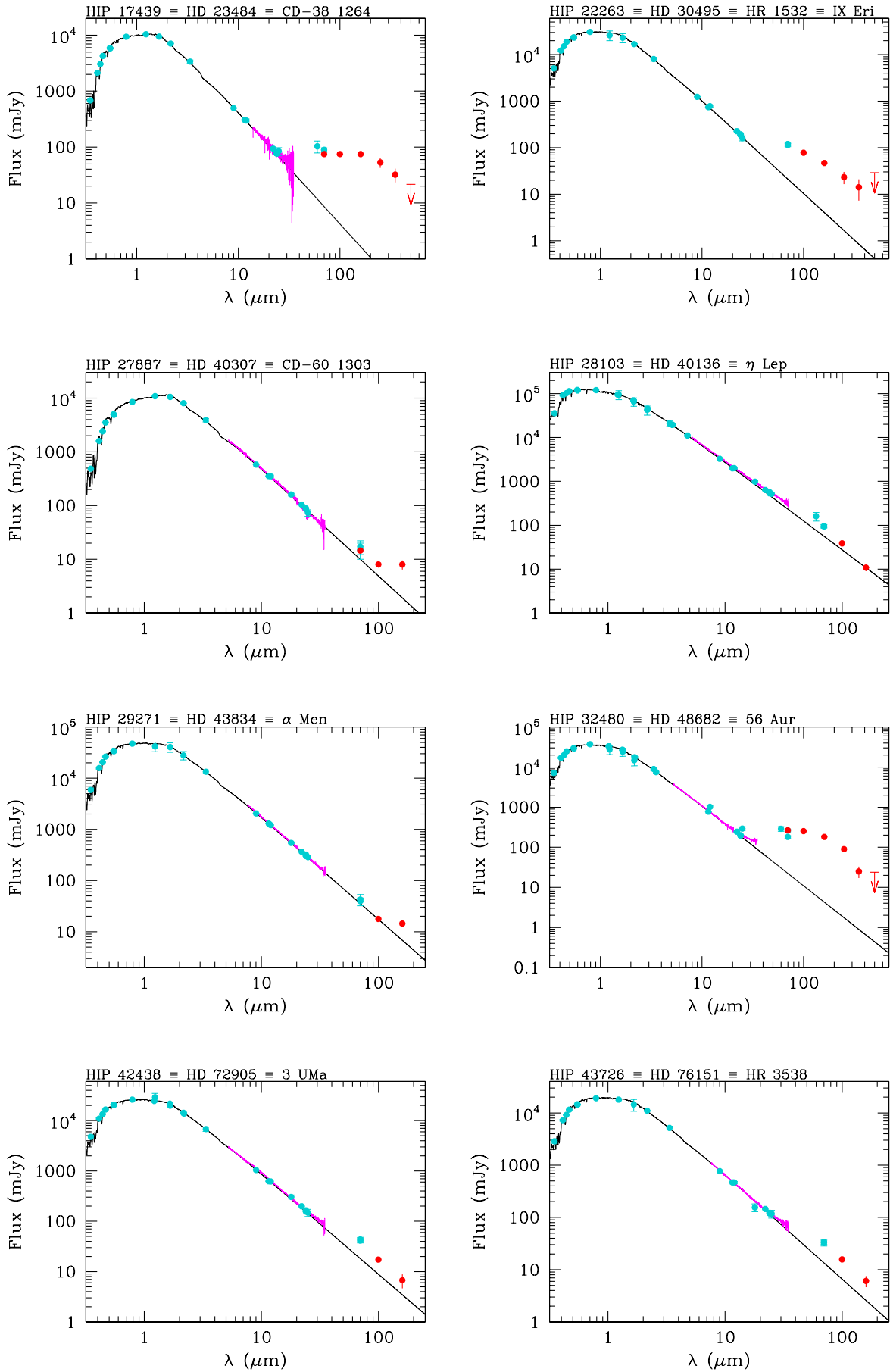


Fig. E.1. SEDs of DUNES stars with excesses (continued).

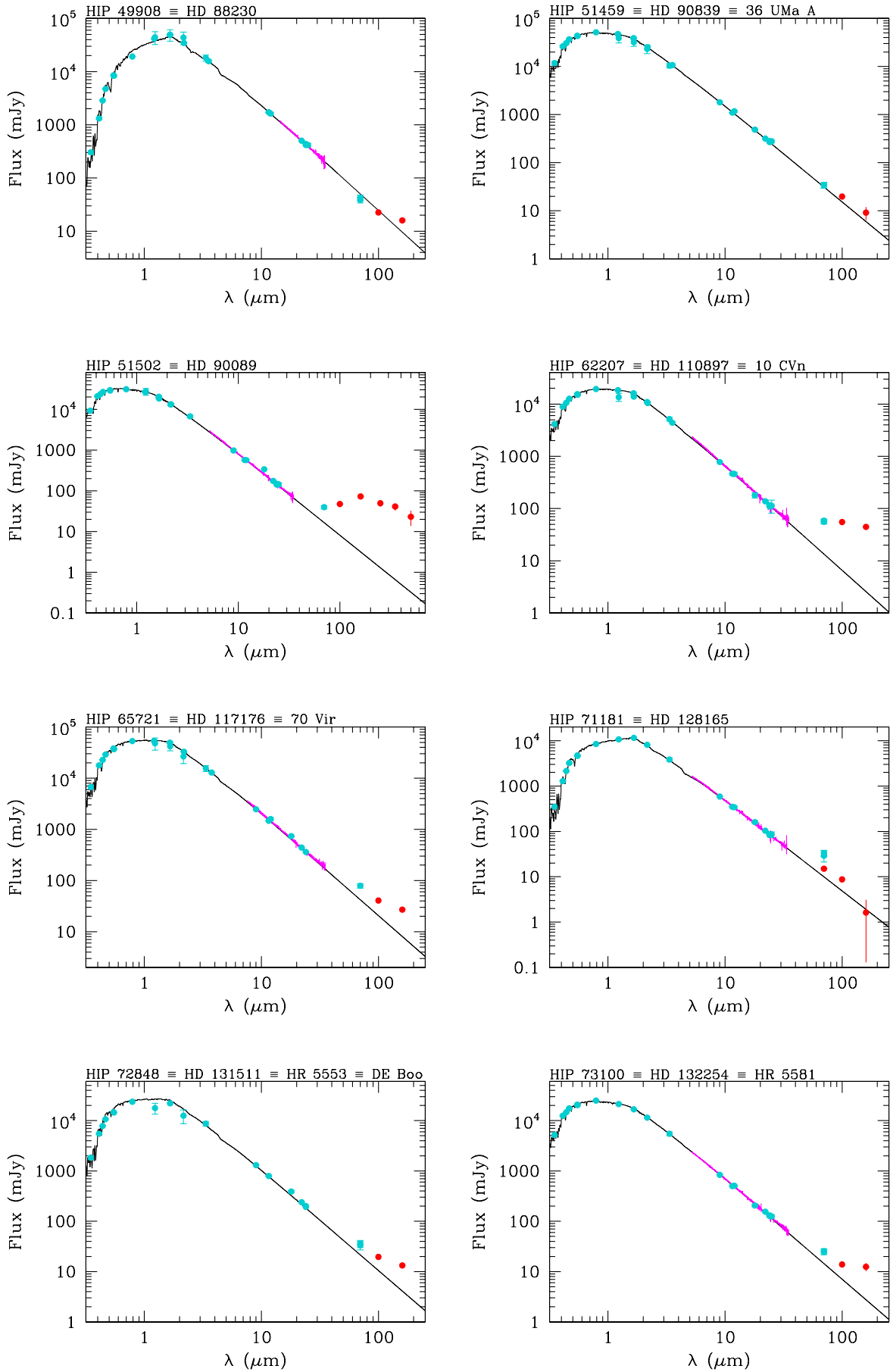


Fig. E.1. SEDs of DUNES stars with excesses (continued).

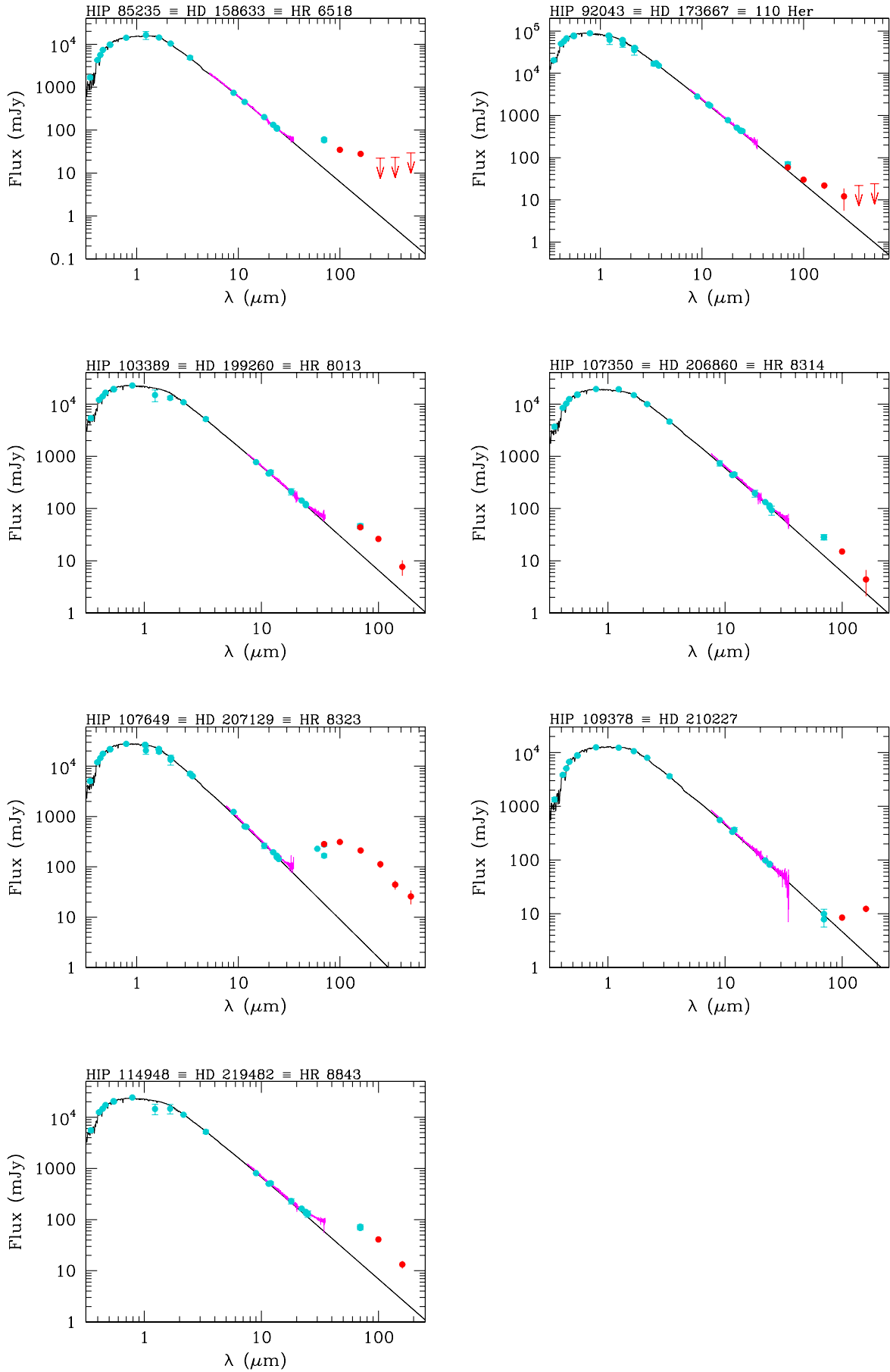


Table 2. Continued.

HIP	HD	Name	SpT	SpT range	ICRS (2000)	Galactic	π (mas)	d(pc)
72603	130819	8 Lib	F3V	F3V - F4IV	14 50 41.181 -15 59 50.05	340.3091 +38.0711	43.52± 0.43	22.98
72848	131511	DE Boo	K2V	K0.5V - K2V	14 53 23.767 +19 09 10.08	023.5506 +60.9355	86.88± 0.46	11.51
73100	132254	LTT 14437	F7V	F5V - F8V	14 56 23.041 +49 37 42.42	084.6437 +57.1726	39.83± 0.26	25.11
73182	131976	BD -20 4123	K5V	M0.5V - M2V	14 57 26.533 -21 24 41.58	338.2393 +32.6833	168.77±21.54	5.93
73184	131977	KX Lib	K4V	K4V - K5V	14 57 28.001 -21 24 55.71	338.2423 +32.6769	171.22± 0.94	5.84
73996	134083	45 Boo	F5V	F5V - F6V	15 07 18.066 +24 52 09.10	036.4509 +59.4794	51.14± 0.31	19.55
77052	140538	ψ Ser	G5V	G2V - G8V	15 44 01.821 +02 30 54.63	009.6985 +41.9676	68.22± 0.66	14.66
78459	143761	ρ CrB	G2V	G0V - G0IV	16 01 02.662 +33 18 12.63	053.4888 +48.9235	58.02± 0.28	17.24
78775	144579	LHS 3152	G8V	G8V - K0V	16 04 56.793 +39 09 23.43	062.3693 +48.2726	68.87± 0.33	14.52
79248	145675	14 Her	K0V	K0IV - K0V	16 10 24.314 +43 49 03.53	069.1704 +46.9449	56.91± 0.34	17.57
80725	148653	CCDM J16289+1825AB	K2V	K1V - K2V	16 28 52.661 +18 24 50.62	035.0885 +39.9946	50.87± 0.80	19.66
82860	153597	19 Dra	F6Vvar	F6V	16 56 01.689 +65 08 05.26	095.6783 +36.4627	65.54± 0.33	15.26
83389	154345	LHS 3260	G8V	G8V - K0V	17 02 36.404 +47 04 54.76	073.0223 +37.6635	53.80± 0.32	18.59
84862	157214	W Her	G0V	G0V - G2V	17 20 39.295 +32 28 21.15	055.8658 +32.3091	69.80± 0.25	14.33
85235	158633	LHS 3287	K0V	G8V - K0V	17 25 00.099 +67 18 24.15	097.5588 +33.1704	78.11± 0.30	12.80
85295	157881	LHS 447	K7V	K5V - M1	17 25 45.233 +02 06 41.12	024.7576 +19.9755	129.86± 0.73	7.70
86036	160269	26 Dra	G0V	G0V - G2V	17 34 59.594 +61 52 28.40	090.9931 +32.6496	70.47± 0.37	14.19
86796	160691	μ Ara	G5V	G3V/VI - G5V	17 44 08.701 -51 50 02.59	340.0607 -11.4981	64.47± 0.31	15.51
88601	165341	70 Oph	K0V SB	K0V	18 05 27.285 +02 30 00.36	029.8934 +11.3670	196.72± 0.83	5.08
88972	166620	HR 6806	K2V	K2V	18 09 37.416 +38 27 28.00	065.3335 +24.2075	90.71± 0.30	11.02
89042	165499	HR 6761	G0V	G0V - G3IV/V	18 10 26.163 -62 00 07.91	332.2098 -19.1639	56.78± 0.52	17.61
91009	234677	BY Dra	K7Vvar	K4V - K6V	18 33 55.773 +51 43 08.91	080.5567 +23.5794	61.15± 0.68	16.35
92043	173667	110 Her	F6V	F5V - F7IV	18 45 39.726 +20 32 46.72	050.7901 +10.4300	52.06± 0.25	19.21
95995	184467	LHS 3466	K1V	K1V - 2V	19 31 07.974 +58 35 09.64	090.2567 +18.0113	58.96± 0.65	16.96
96100	185144	σ Dra	K0V	G9V - K0V	19 32 21.590 +69 39 40.24	101.3033 +21.8770	173.77± 0.18	5.75
96441	185395	13 Cyg	F4V	F3V - F4V	19 36 26.534 +50 13 15.96	082.6677 +13.8470	54.54± 0.15	18.34
97944	188088	V4200 Sgr	K3/K4V	K2V/VI - K4V	19 54 17.745 -23 56 27.85	017.1729 -23.9128	71.18± 0.42	14.05
98959	189567	LHS 484	G2V	G2V - 5V	20 05 32.765 -67 19 15.22	328.4657 -31.9895	56.41± 0.44	17.73
99240	190248	δ Pav	G5IV-Vvar	G8IV	20 08 43.610 -66 10 55.44	329.7673 -32.4165	163.71± 0.17	6.11
99461	191408	LHS 486	K2V	K2V - K2.5V	20 11 11.938 -36 06 04.36	005.2332 -30.9247	166.25± 0.27	6.02
101955	196795	OQ Del	K5V	K5V - M0/1V	20 39 37.710 +04 58 19.34	050.6634 -21.3253	59.80± 3.42	16.72
101997	196761	LHS 3570	G8/K0V	G7.5V - K0V	20 40 11.756 -23 46 25.92	021.2637 -33.7781	69.53± 0.40	14.38
103389	199260	HR 8013	F7V	F6V - F8V	20 56 47.331 -26 17 46.96	019.5852 -38.0955	45.52± 0.38	21.97
104214	201091	61 Cyg A	K5V	K5V	21 06 53.952 +38 44 57.99	082.3197 -05.8181	286.82± 6.78	3.49
104217	201092	61 Cyg B	K7V	K7V - M0V	21 06 55.264 +38 44 31.40	082.3171 -05.8262	285.88± 0.54	3.50
105312	202940	HR 8148	G5V	G5V - G7V	21 19 45.625 -26 21 10.38	021.1811 -43.0983	55.65± 0.62	17.97
106696	205390	NLTT 51629	K2V	K1.5V - K2V	21 36 41.244 -50 50 43.39	346.4153 -46.4331	68.40± 0.58	14.62
107350	206860	HN Peg	G0V	G0IV - G0V	21 44 31.329 +14 46 18.98	069.8594 -28.2693	55.91± 0.45	17.89
107649	207129	HR 8323	G2V	G0V	21 48 15.751 -47 18 13.02	350.8781 -49.1061	62.52± 0.35	15.99
108870	209100	ϵ Ind A	K5V	K3V - K4V	22 03 21.658 -56 47 09.52	336.1926 -48.0449	276.06± 0.28	3.62
109378	210277	LTT 8887	G0	G0V, G8IV/V - G7V	22 09 29.866 -07 32 55.15	052.3504 -46.9651	46.38± 0.48	21.56
109422	210302	τ PsA	F6V	F6V	22 10 08.780 -32 32 54.27	014.1234 -54.8142	54.71± 0.28	18.28
110109	211415	HR 8501	G1V	G0V - G3V	22 18 15.614 -53 37 37.46	339.0111 -51.3872	72.54± 0.36	13.79
113357	217014	51 Peg	G5V	G2IV - G5V	22 57 27.980 +20 46 07.79	090.0626 -34.7273	64.07± 0.38	15.61
113576	217357	LHS 3885	K5/M0V	K5V - M0.5V	23 00 16.122 -22 31 27.65	037.1386 -64.4142	121.69± 0.69	8.22
114948	219482	HR 8843	F7V	F6V - F8V	23 16 57.686 -62 00 04.32	320.6226 -51.7597	48.69± 0.33	20.54
116745	222237	LHS 3994	K3V	K3V	23 39 37.389 -72 43 19.76	310.1686 -43.3827	87.56± 0.51	11.42
120005	79211	CCDM J09144+5241B	K2	K7V, M0V - M0.5V	09 14 24.696 +52 41 11.09	164.9346 +42.6723	156.45± 8.58	6.39

Table 3a. Johnson (BV) and Cousins (I), Strömrgren and 2MASS photometry.

HIP	V	B-V	V-I	$b-y$	m_1	c_1	J	H	K_s	Q
171	5.80	0.69	0.82	0.432	0.184	0.218	4.702±0.214	4.179±0.198	4.068±0.236	CCD
544	6.07	0.75	0.80	0.460	0.290	0.311	4.733±0.019	4.629±0.144	4.314±0.042	EBE
910	4.89	0.49	0.59	0.328	0.130	0.405	4.153±0.268	3.800±0.208	3.821±0.218	DCD
2941	5.57	0.72	0.78	0.435	0.254	0.287	4.437±0.266	3.976±0.224	4.027±0.210	DDC
3093	5.88	0.85	0.83	0.507	0.384	0.335	4.549±0.206	4.064±0.240	3.999±0.036	CDE
3497	6.55	0.66	0.72	0.406	0.192	0.303	5.366±0.024	5.101±0.016	4.945±0.020	AEA
3821	3.46	0.59	0.66	0.372	0.185	0.275	2.109±0.570	2.086±0.504	1.988	DDF
3909	5.17	0.51	0.59	0.332	0.161	0.360	4.412±0.308	4.012±0.280	4.015±0.264	DDD
4148	7.15	0.94	1.00	0.531	0.466	0.269	5.537±0.029	5.049±0.029	4.894±0.031	AAA
7513	4.10	0.54	0.58	0.346	0.176	0.415	3.175±0.210	2.957±0.178	2.859±0.274	CCD
7978	5.52	0.55	0.62	0.350	0.173	0.340	4.791±0.226	4.399±0.234	4.340±0.276	DDD
8768	8.89	1.42	1.80				6.064±0.021	5.405±0.026	5.178±0.020	AAA
10138	6.12	0.81	0.88	0.484	0.337	0.287	4.785±0.248	4.245±0.280	4.125±0.036	DDE
10798	6.33	0.72	0.83	0.442	0.258	0.236	5.056±0.024	4.694±0.044	4.551±0.016	EEA
11452	8.69	1.40	1.66				5.990±0.020	5.332±0.029	5.113±0.018	AAA
11964	8.89	1.39	1.87				5.795±0.018	5.126±0.027	4.885±0.016	AAA
12777	4.10	0.51	0.59	0.325	0.160	0.392	3.031±0.244	2.863±0.206	2.697±0.288	DCD
13402	6.05	0.86	0.91	0.509	0.393	0.300	4.830±0.230	4.230±0.220	4.167±0.242	DDD
14954	5.07	0.58	0.63	0.361	0.185	0.422	4.174±0.280	3.768±0.238	3.748±0.236	DDD
15330	5.53	0.64	0.72	0.404	0.199	0.288	4.462±0.302	4.041±0.268	3.994±0.252	DDD
15371	5.24	0.60	0.67	0.382	0.179	0.298	4.271±0.300	3.874±0.232	3.860±0.228	DDD
15799	6.90	0.84	0.88	0.507	0.355	0.332	5.333±0.021	4.948±0.038	4.767±0.016	AAA
16134	8.39	1.34	1.55	0.771	0.746	0.053	5.888±0.017	5.251±0.024	5.068±0.021	AAA
17420	7.10	0.93	0.97				5.457±0.018	5.025±0.116	4.837±0.020	AEA
17439	6.99	0.87	0.91	0.508	0.400	0.295	5.462±0.019	5.088±0.016	4.934±0.016	AAA
19849	4.43	0.82	0.89	0.484	0.332	0.301	3.013±0.238	2.594±0.198	2.498±0.236	DCD
19884	7.64	1.12	1.23	0.629	0.675	0.172	5.624±0.019	5.098±0.029	4.923±0.020	AAA
22263	5.49	0.63	0.69	0.398	0.213	0.321	4.466±0.254	4.116±0.236	3.999±0.036	DDE
23311	6.22	1.05	1.10	0.602	0.635	0.238	4.389±0.244	3.797±0.214	3.706±0.228	DCD
25110	5.08	0.51	0.58	0.321	0.161	0.431	4.416±0.278	4.201±0.276	3.911±0.020	DDE
27887	7.17	0.94	0.98	0.541	0.462	0.261	5.412±0.019	4.968±0.040	4.793±0.016	AEA
28103	3.71	0.34	0.39	0.218	0.162	0.622	3.063±0.246	2.985±0.232	2.993±0.254	DDD
28442	7.85	1.14	1.23				5.659±0.020	5.070±0.027	4.902±0.018	AAA
29271	5.08	0.71	0.75	0.440	0.265	0.337	3.951±0.232	3.508±0.228	3.446±0.200	DDC
29568	6.37	0.71	0.76	0.430	0.246	0.299	5.129±0.018	4.863±0.036	4.726±0.016	AAA
32439	5.44	0.53	0.60	0.338	0.164	0.346	4.512±0.212	4.262±0.146	4.141±0.034	CBA
32480	5.24	0.58	0.65	0.358	0.184	0.373	4.406±0.274	4.071±0.246	4.132±0.294	DDD
33277	5.74	0.57	0.70	0.377	0.179	0.313	4.913±0.276	4.509±0.204	4.293±0.036	DCE
34017	5.93	0.60	0.74	0.384	0.182	0.328	4.885±0.268	4.612±0.242	4.539±0.075	DDE
34065	5.56	0.62	0.73	0.392	0.180	0.325	4.405±0.224	3.990±0.212	4.037±0.036	DCE
35136	5.54	0.58	0.65	0.374	0.167	0.297	4.655±0.250	4.289±0.220	4.115±0.018	DDE
36439	5.35	0.47	0.54	0.308	0.142	0.390	4.104±0.328	3.937±0.230	4.178±0.015	DDE
38382	5.16	0.60	0.67	0.380	0.196	0.316	4.109±0.248	3.695±0.256	3.730±0.226	DDD
38784	6.55	0.72	0.77	0.450	0.261	0.293	5.235±8.888	4.933±0.038	4.862±0.021	FAA
40693	5.95	0.75	0.79	0.458	0.296	0.312	4.953±0.268	4.364±0.224	4.165±0.036	DDE
40843	5.13	0.49	0.56	0.315	0.149	0.384	4.127±0.222	3.942±0.192	3.868±0.246	DCD
42430	5.05	0.72	0.73	0.447	0.277	0.394	4.048±0.302	3.594±0.248	3.589±0.246	DDD
42438	5.63	0.62	0.66	0.396	0.197	0.293	4.348±0.214	4.282±0.036	4.173±0.036	CEE
43587	5.96	0.87	0.82	0.536	0.357	0.415	4.768±0.244	4.265±0.234	4.015±0.036	DDE
43726	6.01	0.66	0.70	0.413	0.236	0.332	4.871±0.037	4.625±0.276	4.456±0.023	EDA
44897	5.95	0.59	0.66	0.377	0.196	0.323	4.844±0.037	4.601±0.027	4.545±0.020	EAA
45333	5.18	0.61	0.67	0.386	0.182	0.375	4.231±0.246	3.914±0.242	3.782±0.346	DDD
45617	7.20	0.99	0.90	0.585	0.515	0.240	5.382±0.029	4.893±0.023	4.767±0.017	AAA
46580	7.20	1.00	1.07	0.570	0.552	0.231	5.429±0.026	5.002±0.055	4.788±0.023	AAA
47592	4.93	0.53	0.58	0.338	0.164	0.374	4.076±0.338	3.728±0.242	3.722±0.250	DDD
49081	5.37	0.68	0.74	0.418	0.232	0.390	4.267±0.328	4.040±0.258	3.821±0.036	DDE
49908	6.60	1.33	1.29	0.790	0.741	0.032	3.894±0.290	3.298±0.260	2.962±0.288	DDD
51459	4.82	0.54	0.58	0.341	0.171	0.333	4.033±0.218	3.758±0.198	3.644±0.222	DCD
51502	5.25	0.40	0.46	0.265	0.143	0.456	4.416±0.208	4.364±0.036	4.272±0.036	CEE
53721	5.03	0.62	0.69	0.391	0.202	0.343	3.960±0.296	3.736±0.224	3.750±0.340	DDD
54646	8.31	1.26	1.42	0.769	0.755	0.055	5.764±0.020	5.130±0.020	4.979±0.018	AAA

Continued...

Table 3a. Continued.

HIP	V	B-V	V-I	$b-y$	m_1	c_1	J	H	K_s	Q
56452	5.96	0.81	0.88	0.483	0.325	0.238	4.784±0.228	4.138± 0.214	4.022± 0.036	DCE
57507	6.48	0.68	0.74	0.426	0.221	0.280	5.217±0.018	4.935± 0.023	4.798± 0.018	EAA
57939	6.42	0.75	0.88	0.484	0.222	0.155	4.937±0.196	4.500± 0.024	4.373± 0.027	CEA
58345	6.99	1.13	1.22	0.641	0.719	0.159	4.992±0.037	4.617± 0.242	4.525± 0.300	EDD
62145	7.01	0.94	0.98	0.543	0.489	0.283	5.318±8.888	4.900± 0.020	4.780± 0.016	FEA
62207	5.95	0.56	0.65	0.374	0.147	0.284	5.173±0.186	4.667± 0.036	4.465± 0.029	CEA
62523	6.29	0.70	0.74	0.438	0.241	0.334	5.123±0.262	4.705± 0.036	4.645± 0.020	DEA
64792	5.19	0.59	0.64	0.373	0.189	0.384	4.392±0.284	4.107± 0.208	4.033± 0.238	DCD
64797	6.49	0.93	0.97	0.532	0.422	0.296	4.901±0.037	4.584± 0.017	4.381± 0.036	EEE
65026	8.48	1.47	1.89				5.338±0.026	4.721± 0.018	4.494± 0.018	EAA
65721	4.97	0.71	0.77	0.447	0.231	0.352	3.798±0.286	3.457± 0.206	3.500± 0.294	DCD
67275	4.50	0.51	0.51	0.318	0.177	0.439	3.617±0.284	3.546± 0.242	3.507± 0.348	DDD
67422	7.05	1.11	1.16				5.077±0.048	4.561± 0.026	6.333	EAU
67620	6.43	0.70	0.78	0.433	0.241	0.310	5.530±0.308	4.829± 0.042	4.665± 0.017	DAA
68184	6.49	1.04	1.01				5.018±0.260	4.402± 0.206	4.094	DCF
68682	6.27	0.73	0.82	0.451	0.267	0.316	5.388±0.294	4.765± 0.015	4.459± 0.024	DEA
69965	5.87	0.52	0.61	0.338	0.125	0.300	4.956±0.334	4.717± 0.076	4.512± 0.027	DEA
70319	6.25	0.64	0.71	0.405	0.188	0.281	5.053±0.037	4.814± 0.067	4.644± 0.017	EEA
70857	6.88	0.77	0.81	0.472	0.269	0.275	5.425±0.018	5.011± 0.031	4.917± 0.018	EAA
71181	7.24	1.00	1.04	0.571	0.566	0.246	5.436±0.037	4.872± 0.029	4.789± 0.017	EAA
71681	1.35	0.90	0.88				1.454±0.133	1.886± 0.220	2.008± 0.260	BDD
71683	-0.01	0.71	0.69	0.438	0.248	0.373	1.454±0.133	1.886± 0.220	2.008± 0.260	BDD
71908	3.18	0.26	0.26	0.137	0.209	0.782	2.544±0.284	2.471± 0.196	2.425± 0.216	DCC
72567	5.86	0.58	0.67	0.374	0.191	0.321	4.998±0.218	4.688± 0.226	4.458± 0.020	DDA
72603	5.15	0.40	0.48	0.263	0.157	0.494	4.475±0.266	4.266± 0.204	4.297± 0.280	DCD
72848	6.00	0.84	0.92	0.502	0.365	0.296	4.882±0.260	4.165± 0.036	4.316± 0.326	DED
73100	5.63	0.53	0.61	0.338	0.174	0.410	4.685±0.037	4.464± 0.018	4.408± 0.026	EAA
73182	8.01	1.52	2.22	0.944	0.486	0.189	4.550±0.262	3.910± 0.200	3.802± 0.230	DCD
73184	5.72	1.02	1.23	0.617	0.669	0.190	3.663±0.258	3.085± 0.196	3.048± 0.224	DCD
73996	4.93	0.43	0.51	0.287	0.159	0.446	4.246±0.268	4.013± 0.218	3.863± 0.040	DDE
77052	5.86	0.68	0.74	0.424	0.231	0.334	4.593±0.352	4.045± 0.348	4.297± 0.036	DDE
78459	5.39	0.61	0.68	0.394	0.178	0.337	4.088±0.240	3.989± 0.036	3.857± 0.036	DEE
78775	6.66	0.73	0.80	0.456	0.241	0.229	5.182±0.020	4.824± 0.017	4.755± 0.016	AAA
79248	6.61	0.88	0.92	0.537	0.366	0.438	5.158±0.029	4.803± 0.016	4.714± 0.016	AAA
80725	6.98	0.85	0.94				5.387±0.019	4.971± 0.017	4.901± 0.017	AAA
82860	4.88	0.48	0.56	0.327	0.154	0.364	4.020±0.312	3.830± 0.228	3.736± 0.292	DDD
83389	6.76	0.73	0.78	0.449	0.272	0.285	5.411±0.041	5.098± 0.020	5.003± 0.017	AAA
84862	5.38	0.62	0.70	0.404	0.179	0.312	4.160±0.266	3.905± 0.246	3.911± 0.234	DDD
85235	6.44	0.76	0.80	0.463	0.279	0.242	4.969±0.228	4.637± 0.036	4.515± 0.018	DEA
85295	7.54	1.36	1.62	0.783	0.744	0.045	4.934±0.024	4.341± 0.044	4.370± 0.274	AED
86036	5.23	0.60	0.67	0.395	0.189	0.330	4.239±0.292	3.885± 0.226	3.744± 0.290	DDD
86796	5.12	0.69	0.71	0.432	0.244	0.393	4.158±0.284	3.724± 0.206	3.683± 0.246	DCD
88601	4.03	0.86	0.96	0.508	0.390	0.262	2.343±0.296	1.876± 0.244	1.791± 0.304	DDD
88972	6.38	0.88	1.00	0.518	0.406	0.295	4.952±0.278	4.458± 0.192	4.232± 0.021	DCA
89042	5.47	0.59	0.65	0.377	0.182	0.350	4.430±0.306	4.022± 0.244	4.130± 0.266	DDD
91009	8.20	1.27	1.44				5.597±0.023	5.020± 0.016	4.843± 0.021	AAA
92043	4.19	0.48	0.55	0.314	0.150	0.484	3.527±0.242	3.286± 0.176	3.190± 0.256	DCD
95995	6.60	0.86	0.90	0.513	0.373	0.275	5.020±0.043	4.613± 0.036	4.463± 0.015	EAE
96100	4.67	0.79	0.85	0.472	0.321	0.267	3.423±0.270	3.039± 0.214	2.900± 0.324	DCD
96441	4.49	0.40	0.44	0.261	0.157	0.502	3.878±0.284	3.716± 0.234	3.537± 0.296	DDD
97944	6.22	1.02	1.02	0.596	0.591	0.244	4.747±0.254	4.158± 0.240	4.043± 0.252	DDD
98959	6.07	0.65	0.72	0.405	0.194	0.298	5.108±0.266	4.724± 0.076	4.511± 0.026	DEA
99240	3.55	0.75	0.76	0.466	0.292	0.384	2.299±0.272	2.041± 0.240	1.933± 0.272	DDD
99461	5.32	0.87	0.98	0.515	0.362	0.271	3.518±0.300	2.999± 0.422	3.008± 0.602	DDD
101955	7.88	1.24	1.44				5.509±0.021	4.899± 0.016	4.739± 0.018	AAA
101997	6.36	0.72	0.78	0.440	0.257	0.260	5.296±0.266	4.810± 0.044	4.597± 0.016	DAA
103389	5.70	0.51	0.57	0.328	0.164	0.355	5.077±0.272	4.734± 0.076	4.475± 0.036	DEE
104214	5.20	1.07	1.13	0.658	0.679	0.132	3.114±0.268	2.540± 0.198	2.248± 0.318	DCD
104217	6.05	1.31	1.27	0.791	0.675	0.067	3.546±0.278	2.895± 0.218	2.544± 0.328	DDD
105312	6.56	0.74	0.85	0.450	0.247	0.273	5.114±0.017	4.720± 0.076	4.574± 0.021	EEA
106696	7.14	0.88	0.94	0.514	0.401	0.263	5.518±0.035	5.137± 0.053	4.970± 0.021	AAA

Continued...

Table 3a. Continued.

HIP	V	B-V	V-I	$b-y$	m_1	c_1	J	H	K_s	Q
107350	5.96	0.59	0.66	0.377	0.186	0.314	4.793±0.035	4.598± 0.036	4.559± 0.038	EEA
107649	5.57	0.60	0.66	0.383	0.190	0.337	4.720±0.176	4.306± 0.076	4.236± 0.240	CED
108870	4.69	1.06	1.15	0.603	0.618	0.212	2.894±0.292	2.349± 0.214	2.237± 0.240	DCD
109378	6.54	0.77	0.77	0.466	0.285	0.369	5.275±0.024	4.957± 0.031	4.799± 0.020	AAA
109422	4.94	0.49	0.54	0.313	0.167	0.430	3.930±0.302	3.639± 0.262	3.704± 0.292	DDD
110109	5.36	0.61	0.70	0.389	0.178	0.303	4.426±0.260	3.925± 0.248	3.913± 0.272	DDD
113357	5.45	0.67	0.69	0.416	0.233	0.371	4.655±0.296	4.234± 0.270	3.911± 0.021	DDA
113576	7.88	1.38	1.63	0.798	0.700	0.057	5.346±0.021	4.696± 0.076	4.478± 0.016	AEA
114948	5.64	0.52	0.59	0.337	0.161	0.355	5.100±0.250	4.606± 0.228	4.437± 0.015	DDE
116745	7.09	0.99	1.11	0.568	0.526	0.243	5.249±0.018	4.745± 0.061	4.581± 0.029	AEA
120005	7.70	1.42	1.72	0.858	0.626	0.076	4.779±0.174	4.043± 0.206	4.136± 0.020	CCE

Table 3b. Additional near-infrared photometry.

HIP	HR	J	H	K	L	L'	M	Ref.
910	33	3.95	3.68	3.63	3.59	3.58		1
		3.964	3.689	3.636	3.60	3.60		2
		3.966	3.672	3.647	3.611			3, 4
		3.943	3.679	3.639	3.617		3.657	5
3821	219	2.35	2.02	1.96				1
		2.466		2.085	2.065			6
7513	458	3.11		2.84		2.80		1
		3.166		2.874	2.863			6
8768		6.120	5.387	5.240				3
		6.015	5.397	5.206	5.126			7
		6.11	5.39	5.21		5.07		8
10138	637	4.630	4.210	4.140	4.100			9
12777	799	3.34	3.07	2.98	2.96			1
13402	857	4.500	4.110	4.020	3.970			9
15330	1006	4.382	4.036	3.980	3.947			3, 4
		4.423	4.088	4.016				5
		4.340	4.020	3.970	3.940			9
15371	1010	4.130	3.820	3.770	3.730			9
19849	1325	2.962		2.452	2.428			6
23311	1614	4.350	3.900	3.800	3.750			9
25110	1686	4.190	3.970	3.930	3.910			9, 10
28103	2085	3.10	2.95	2.90	2.87			1
		3.101	2.953	2.907	2.878		2.895	5
		3.080	2.940	2.910	2.880			9, 10
32439	2401	4.450	4.200	4.160	4.140			9
32480	2483	4.230	3.970	3.930				2, 10
34017	2643	4.89	4.55	4.52				1
		4.937		4.565	4.624			6
34065	2667	4.455	4.148	4.081				5
35136	2721	4.475	4.180	4.126		4.08		2
		4.48	4.13	4.10				10
38382	3064	3.979	3.685	3.630				11
40693	3259	4.590	4.220	4.170	4.110			9
40843	3262	4.180	3.940	3.920	3.900			9
42438	3391	4.55	4.21	4.19				10
43587	3522	4.59	4.14	4.07	3.98			1
45333	3648	4.060	3.76	3.71				10
		4.060	3.760	3.710	3.690			9
49908		3.98	3.32	3.19	3.110			12
51459	4112	3.84	3.58	3.54				9, 10
51502	4084	4.47	4.28	4.24				10
		4.470	4.280	4.240	4.230			9
57939	4550	4.92	4.44	4.38	4.34	4.34	4.41	1
		4.957	4.466	4.400	4.35	4.38	4.41	2
		4.870	4.455	4.385	4.340			13
		4.89	4.43	4.37	4.34			12
62207	4845	4.91	4.55	4.50				1
		4.815	4.530	4.485	4.500			11
65026		5.25	4.70	4.505				10
65721	5072	3.71	3.32	3.25		3.21		1
		3.759		3.289	3.282			6
67275	5185	3.684		3.393	3.390			6
70319	5384	5.13	4.74	4.68	4.61	4.61	4.62	1
		5.027	4.713	4.662	4.637			11
		5.149	4.788	4.718	4.703		4.708	5
72567	5534	4.79	4.53	4.48				10
72603	5530	4.41	4.19	4.16	4.10		4.13	1
		4.416	4.211	4.155	4.104		4.153	5
		4.40	4.18	4.130				10
		4.350	4.140	4.110	4.100			9
73184	5568	3.83	3.24	3.17	3.08			1

Continued...

Table 3b. Continued

HIP	HR	J	H	K	L	L'	M	Ref.
73996	5634	4.12	3.90	3.88	3.89			1
		4.094	3.907	3.866				
		4.090	3.890	3.860	3.850			9
		4.193		3.912	3.918			6
78459	5968	4.241	3.940	3.877				11
82860	6315	3.900	3.640	3.590	3.570			9
88972	6806	4.77	4.29	4.24	4.16			1
89042	6761	4.410	4.120	4.080	4.010			9
92043	7061	3.32		3.06		3.03		1
		3.300	3.080	3.040	3.010			9
		3.374		3.092	3.090			6
96441	7469	3.75		3.52		3.47		1
		3.803		3.551	3.527			6
98959	7644	4.958	4.617	4.553				5
99240	7665	2.317	1.990	1.924	1.877		1.950	5
		2.326	1.953	1.897	1.870			4
104214	8085	3.10	2.44	2.35				1
104217	8086	3.53	2.83	2.70				1
107649	8323	4.470	4.200	4.140	4.090			9
109422	8447	4.030	3.820	3.780	3.770			9
113357	8729	4.36	4.03	3.97				1

References:

- 1: UKIRT very bright standards: http://www.jach.hawaii.edu/UKIRT/astronomy/calib/phot_cal/bright_stds.html
- 2: UKIRT general standards: http://www.jach.hawaii.edu/UKIRT/astronomy/calib/phot_cal/brtJHK_stds.html
- 3: SAAO infrared standards: <http://www.sao.ac.za/fileadmin/files/links/IRstd.txt>
- 4: Carter (1990)
- 5: Koornneef (1983)
- 6: Selby et al. (1988)
- 7: Elias et al. (1983)
- 8: AAO photometric standards: Allen & Cragg (1983)
- 9: Aumann & Probst (1991)
- 10: Catalogue of Infrared Observations, Gezari et al. (2000): <http://ircatalog.gsfc.nasa.gov/>
- 11: CVF standards: <http://www.iac.es/telescopes/pages/es/inicio/utilidades.php#CVF>
- 12: Glass (1975)
- 13: Elias et al. (1982)

Table 3c. AKARI and WISE fluxes.

HIP	AKARI		WISE		
	9 μm (Jy)	18 μm (Jy)	3.35 μm (W1) (Jy)	11.56 μm (W3) (Jy)	22.09 μm (W4) (Jy)
171			9.15(+0) \pm 8.86(-1)	8.36(-1) \pm 1.16(-2)	2.53(-1) \pm 5.37(-3)
544	1.05(+0) \pm 5.95(-3)	2.73(-1) \pm 2.94(-2)	5.84(+0) \pm 4.42(-1)	5.36(-1) \pm 6.92(-3)	1.86(-1) \pm 3.95(-3)
910	2.00(+0) \pm 3.24(-2)	4.54(-1) \pm 4.68(-2)	1.10(+1) \pm 1.17(+0)	1.04(+0) \pm 1.34(-2)	3.05(-1) \pm 5.89(-3)
2941			9.27(+0) \pm 1.14(+0)	8.20(-1) \pm 1.06(-2)	2.50(-1) \pm 4.37(-3)
3093	1.51(+0) \pm 1.62(-2)	3.49(-1) \pm 1.19(-2)	8.84(+0) \pm 8.15(-1)	7.77(-1) \pm 1.00(-2)	2.27(-1) \pm 4.60(-3)
3497	6.12(-1) \pm 1.77(-2)	1.68(-1) \pm 1.16(-2)	3.29(+0) \pm 2.28(-1)	3.00(-1) \pm 4.15(-3)	9.13(-2) \pm 2.61(-3)
3821	1.03(+1) \pm 6.06(-2)	2.24(+0) \pm 3.53(-2)	2.68(+1) \pm 9.38(-1)	7.91(+0) \pm 2.91(-2)	1.72(+0) \pm 1.58(-2)
3909	1.53(+0) \pm 2.51(-2)	3.23(-1) \pm 2.32(-2)	7.99(+0) \pm 6.26(-1)	7.72(-1) \pm 1.07(-2)	2.34(-1) \pm 5.60(-3)
4148	6.64(-1) \pm 6.69(-3)		3.41(+0) \pm 2.26(-1)	3.13(-1) \pm 4.90(-3)	9.22(-2) \pm 2.38(-3)
7513	4.15(+0) \pm 1.32(-2)	9.26(-1) \pm 3.18(-2)	2.11(+1) \pm 3.90(+0)	2.05(+0) \pm 2.83(-2)	6.05(-1) \pm 1.00(-2)
7978	1.15(+0) \pm 1.88(-2)	3.12(-1) \pm 3.93(-2)	6.20(+0) \pm 5.60(-1)	6.00(-1) \pm 7.74(-3)	2.18(-1) \pm 4.02(-3)
8768	5.43(-1) \pm 2.03(-2)	1.25(-1) \pm 2.23(-2)	2.86(+0) \pm 1.90(-1)	2.74(-1) \pm 3.79(-3)	8.63(-2) \pm 2.31(-3)
10138			7.23(+0) \pm 5.87(-1)	6.56(-1) \pm 7.85(-3)	1.92(-1) \pm 3.88(-3)
10798	8.47(-1) \pm 1.33(-2)	1.79(-1) \pm 2.03(-2)	5.02(+0) \pm 3.94(-1)	4.46(-1) \pm 6.16(-3)	1.33(-1) \pm 2.94(-3)
11452	5.73(-1) \pm 6.70(-3)		2.96(+0) \pm 1.97(-1)	2.74(-1) \pm 3.79(-3)	8.32(-2) \pm 2.07(-3)
11964	7.51(-1) \pm 6.59(-3)	2.23(-1) \pm 3.36(-2)	3.68(+0) \pm 2.61(-1)	3.87(-1) \pm 5.35(-3)	1.23(-1) \pm 2.72(-3)
12777	4.20(+0) \pm 3.99(-2)	9.91(-1) \pm 3.76(-2)	2.12(+1) \pm 1.96(+0)	2.02(+0) \pm 2.05(-2)	6.04(-1) \pm 8.90(-3)
13402	1.42(+0) \pm 2.04(-2)	3.21(-1) \pm 1.68(-2)	7.88(+0) \pm 8.07(-1)	7.40(-1) \pm 9.55(-3)	2.30(-1) \pm 4.46(-3)
14954	1.94(+0) \pm 2.22(-2)	4.23(-1) \pm 1.40(-2)	1.06(+1) \pm 1.16(+0)	1.00(+0) \pm 1.20(-2)	2.89(-1) \pm 5.33(-3)
15330			8.56(+0) \pm 8.37(-1)	7.62(-1) \pm 1.05(-2)	2.26(-1) \pm 4.57(-3)
15371			9.13(+0) \pm 9.94(-1)	9.09(-1) \pm 1.26(-2)	2.77(-1) \pm 5.10(-3)
15799	7.46(-1) \pm 9.75(-3)	2.04(-1) \pm 2.74(-2)	4.11(+0) \pm 3.15(-1)	3.96(-1) \pm 5.11(-3)	1.18(-1) \pm 2.49(-3)
16134	5.64(-1) \pm 5.81(-3)		3.01(+0) \pm 1.97(-1)	2.93(-1) \pm 3.77(-3)	8.80(-2) \pm 2.11(-3)
17420	6.41(-1) \pm 1.45(-2)	1.55(-1) \pm 4.64(-2)	3.48(+0) \pm 2.12(-1)	3.33(-1) \pm 4.91(-3)	9.65(-2) \pm 2.40(-3)
17439	5.87(-1) \pm 7.85(-3)		3.37(+0) \pm 2.42(-1)	3.06(-1) \pm 4.23(-3)	9.40(-2) \pm 1.99(-3)
19849			3.17(+1) \pm 7.13(+0)	2.96(+0) \pm 3.54(-2)	9.15(-1) \pm 1.69(-2)
19884	6.26(-1) \pm 8.36(-3)	1.50(-1) \pm 1.37(-2)	3.35(+0) \pm 2.47(-1)	3.21(-1) \pm 4.14(-3)	9.48(-2) \pm 2.10(-3)
22263	1.46(+0) \pm 8.34(-3)		8.02(+0) \pm 7.62(-1)	7.42(-1) \pm 1.03(-2)	2.26(-1) \pm 4.36(-3)
23311	1.75(+0) \pm 2.28(-2)		9.81(+0) \pm 9.05(-1)	8.98(-1) \pm 1.24(-2)	2.61(-1) \pm 6.02(-3)
25110	1.50(+0) \pm 1.56(-2)	3.70(-1) \pm 3.60(-2)	8.38(+0) \pm 8.11(-1)	7.58(-1) \pm 1.05(-2)	2.30(-1) \pm 5.30(-3)
27887	6.83(-1) \pm 7.21(-3)	1.59(-1) \pm 9.25(-3)	3.91(+0) \pm 2.95(-1)	3.55(-1) \pm 4.57(-3)	1.04(-1) \pm 2.40(-3)
28103	3.89(+0) \pm 1.09(-2)	9.75(-1) \pm 4.59(-2)	2.09(+1) \pm 3.03(+0)	1.99(+0) \pm 2.19(-2)	6.38(-1) \pm 1.12(-2)
28442	6.48(-1) \pm 1.71(-2)	1.64(-1) \pm 4.68(-3)	3.33(+0) \pm 3.35(-1)	3.10(-1) \pm 7.43(-3)	9.51(-2) \pm 4.91(-3)
29271	2.42(+0) \pm 6.54(-3)	5.39(-1) \pm 1.25(-2)	1.33(+1) \pm 1.09(+0)	1.30(+0) \pm 1.20(-2)	3.67(-1) \pm 6.42(-3)
29568	7.76(-1) \pm 1.59(-2)		3.74(+0) \pm 2.55(-1)	3.83(-1) \pm 5.29(-3)	1.15(-1) \pm 2.32(-3)
32439	1.20(+0) \pm 1.14(-2)	2.59(-1) \pm 2.40(-2)	7.03(+0) \pm 6.55(-1)	6.15(-1) \pm 9.06(-3)	1.82(-1) \pm 4.18(-3)
32480	1.60(+0) \pm 5.32(-2)	4.58(-1) \pm 1.73(-2)	8.96(+0) \pm 8.02(-1)	7.74(-1) \pm 1.07(-2)	2.46(-1) \pm 4.75(-3)
33277	1.09(+0) \pm 4.87(-3)	2.51(-1) \pm 7.37(-2)	6.11(+0) \pm 5.35(-1)	5.40(-1) \pm 6.97(-3)	1.62(-1) \pm 3.72(-3)
34017	9.23(-1) \pm 2.63(-2)	2.51(-1) \pm 1.14(-2)	5.17(+0) \pm 4.48(-1)	4.64(-1) \pm 5.55(-3)	1.37(-1) \pm 2.90(-3)
34065	1.39(+0) \pm 2.35(-2)	4.25(-1) \pm 4.81(-2)	8.59(+0) \pm 7.44(-1)	7.13(-1) \pm 9.19(-3)	2.18(-1) \pm 4.41(-3)
35136	1.33(+0) \pm 1.55(-2)	2.55(-1) \pm 3.45(-2)	7.63(+0) \pm 7.88(-1)	6.64(-1) \pm 9.17(-3)	2.00(-1) \pm 4.06(-3)
36439	1.25(+0) \pm 7.20(-3)	2.99(-1) \pm 3.19(-2)	6.33(+0) \pm 5.37(-1)	6.11(-1) \pm 8.45(-3)	1.79(-1) \pm 3.80(-3)
38382	1.89(+0) \pm 3.79(-2)	4.62(-1) \pm 2.60(-2)	1.13(+1) \pm 1.41(+0)	9.71(-1) \pm 1.43(-2)	2.87(-1) \pm 5.83(-3)
38784	6.31(-1) \pm 1.04(-2)	1.53(-1) \pm 8.13(-3)	3.43(+0) \pm 2.34(-1)	3.36(-1) \pm 4.64(-3)	9.85(-2) \pm 2.18(-3)
40693	1.30(+0) \pm 1.34(-2)	4.84(-1) \pm 1.02(-1)	6.91(+0) \pm 5.99(-1)	6.71(-1) \pm 9.27(-3)	2.78(-1) \pm 4.86(-3)
40843		5.30(-1) \pm 3.58(-2)	8.22(+0) \pm 7.81(-1)	8.04(-1) \pm 1.04(-2)	2.30(-1) \pm 4.66(-3)
42430	2.38(+0) \pm 1.93(-2)	5.14(-1) \pm 2.66(-2)	1.19(+1) \pm 7.69(-1)	1.17(+0) \pm 1.29(-2)	3.61(-1) \pm 6.98(-3)
42438	1.23(+0) \pm 1.34(-2)	3.02(-1) \pm 2.65(-2)	6.77(+0) \pm 6.62(-1)	6.26(-1) \pm 8.07(-3)	1.99(-1) \pm 3.66(-3)
43587	1.41(+0) \pm 2.16(-2)	2.90(-1) \pm 1.62(-2)	7.18(+0) \pm 6.42(-1)	6.89(-1) \pm 8.89(-3)	2.06(-1) \pm 4.75(-3)
43726	9.03(-1) \pm 1.23(-2)	1.54(-1) \pm 2.63(-2)	5.17(+0) \pm 4.25(-1)	4.66(-1) \pm 5.15(-3)	1.45(-1) \pm 3.47(-3)
44897	8.67(-1) \pm 1.12(-2)	2.04(-1) \pm 3.18(-2)	4.58(+0) \pm 3.63(-1)	4.31(-1) \pm 5.56(-3)	1.31(-1) \pm 3.01(-3)
45333	1.85(+0) \pm 8.04(-3)	4.12(-1) \pm 3.69(-2)	1.03(+1) \pm 1.05(+0)	9.54(-1) \pm 1.23(-2)	2.82(-1) \pm 5.98(-3)
45617	7.50(-1) \pm 1.46(-2)	1.30(-1) \pm 3.45(-2)	3.51(+0) \pm 2.62(-1)	3.52(-1) \pm 4.87(-3)	1.07(-1) \pm 2.26(-3)
46580	7.33(-1) \pm 1.38(-2)	1.06(-1) \pm 7.80(-4)	3.51(+0) \pm 2.23(-1)	3.57(-1) \pm 4.27(-3)	1.07(-1) \pm 2.37(-3)
47592	1.96(+0) \pm 1.66(-2)	4.70(-1) \pm 2.05(-2)	1.15(+1) \pm 1.24(+0)	1.01(+0) \pm 1.39(-2)	2.97(-1) \pm 6.56(-3)
49081	1.63(+0) \pm 1.92(-2)	3.98(-1) \pm 1.83(-2)	9.35(+0) \pm 9.14(-1)	8.34(-1) \pm 1.08(-2)	2.45(-1) \pm 4.51(-3)
49908			1.80(+1) \pm 2.48(+0)	1.72(+0) \pm 1.43(-2)	5.03(-1) \pm 8.34(-3)
51459	2.12(+0) \pm 1.31(-2)	4.80(-1) \pm 1.20(-2)	1.04(+1) \pm 1.12(+0)	1.10(+0) \pm 1.51(-2)	3.18(-1) \pm 6.45(-3)
51502	1.16(+0) \pm 7.47(-3)	3.34(-1) \pm 1.37(-2)	6.73(+0) \pm 5.46(-1)	5.71(-1) \pm 7.36(-3)	1.75(-1) \pm 3.38(-3)

Continued...

Table 3c. Continued.

HIP	AKARI		WISE		
	9 μ m (Jy)	18 μ m (Jy)	3.35 μ m (W1) (Jy)	11.56 μ m (W3) (Jy)	22.09 μ m (W4) (Jy)
53721	2.07(+0) \pm 1.86(-2)	4.46(-1) \pm 3.82(-2)	1.11(+1) \pm 7.28(-1)	1.10(+0) \pm 1.21(-2)	3.14(-1) \pm 6.08(-3)
54646	6.27(-1) \pm 1.80(-2)	1.73(-1) \pm 9.39(-2)	3.40(+0) \pm 2.48(-1)	3.12(-1) \pm 4.31(-3)	9.22(-2) \pm 2.21(-3)
56452	1.44(+0) \pm 7.13(-3)	4.24(-1) \pm 4.50(-2)	8.25(+0) \pm 8.06(-1)	7.42(-1) \pm 9.57(-3)	2.19(-1) \pm 4.44(-3)
57507	6.91(-1) \pm 1.68(-2)	1.29(-1) \pm 1.16(-2)	3.86(+0) \pm 2.71(-1)	3.44(-1) \pm 4.75(-3)	1.04(-1) \pm 2.58(-3)
57939			5.48(+0) \pm 3.99(-1)	5.19(-1) \pm 6.69(-3)	1.54(-1) \pm 3.41(-3)
58345	1.10(+0) \pm 1.48(-2)	2.97(-1) \pm 3.00(-2)	6.20(+0) \pm 4.97(-1)	5.64(-1) \pm 6.75(-3)	1.70(-1) \pm 3.92(-3)
62145	7.05(-1) \pm 1.07(-2)	1.50(-1) \pm 2.44(-2)	3.98(+0) \pm 2.86(-1)	3.61(-1) \pm 4.66(-3)	1.06(-1) \pm 2.43(-3)
62207	9.17(-1) \pm 2.33(-2)	1.78(-1) \pm 2.06(-2)	5.16(+0) \pm 4.18(-1)	4.64(-1) \pm 6.41(-3)	1.38(-1) \pm 3.05(-3)
62523	7.90(-1) \pm 1.82(-2)		4.20(+0) \pm 2.91(-1)	4.00(-1) \pm 5.53(-3)	1.17(-1) \pm 2.47(-3)
64792	1.67(+0) \pm 2.26(-2)	3.96(-1) \pm 1.64(-2)	9.40(+0) \pm 9.80(-1)	8.56(-1) \pm 1.18(-2)	2.61(-1) \pm 4.56(-3)
64797	1.38(+0) \pm 2.32(-2)	3.65(-1) \pm 1.21(-2)	6.18(+0) \pm 9.02(-1)	4.98(-1) \pm 5.97(-3)	1.56(-1) \pm 3.59(-3)
65026	1.12(+0) \pm 1.67(-2)	3.25(-1) \pm 3.51(-2)	5.45(+0) \pm 4.12(-1)	5.85(-1) \pm 7.54(-3)	1.81(-1) \pm 3.67(-3)
65721	2.91(+0) \pm 3.67(-2)	7.30(-1) \pm 2.42(-2)	1.56(+1) \pm 2.15(+0)	1.47(+0) \pm 9.51(-3)	4.41(-1) \pm 9.34(-3)
67275	2.63(+0) \pm 1.23(-2)	5.59(-1) \pm 1.43(-2)	1.53(+1) \pm 2.42(+0)	1.36(+0) \pm 1.63(-2)	4.00(-1) \pm 8.47(-3)
67422	1.12(+0) \pm 1.43(-2)	2.65(-1) \pm 3.86(-2)	5.53(+0) \pm 6.84(-1)	4.67(-1) \pm 1.16(-2)	1.42(-1) \pm 7.06(-3)
67620	8.42(-1) \pm 2.25(-2)	2.16(-1) \pm 8.64(-2)	4.29(+0) \pm 3.28(-1)	4.03(-1) \pm 5.56(-3)	1.20(-1) \pm 3.20(-3)
68184	1.33(+0) \pm 1.61(-2)	3.19(-1) \pm 3.38(-2)	7.26(+0) \pm 6.36(-1)	6.80(-1) \pm 9.39(-3)	2.01(-1) \pm 3.53(-3)
68682	9.68(-1) \pm 2.26(-2)	2.62(-1) \pm 2.14(-2)	5.38(+0) \pm 4.51(-1)	4.96(-1) \pm 6.39(-3)	1.49(-1) \pm 3.29(-3)
69965		2.69(-1) \pm 4.20(-2)	5.39(+0) \pm 4.58(-1)	4.82(-1) \pm 6.65(-3)	1.42(-1) \pm 3.15(-3)
70319	7.44(-1) \pm 1.17(-2)	1.29(-1) \pm 4.62(-2)	4.25(+0) \pm 3.09(-1)	3.90(-1) \pm 5.02(-3)	1.16(-1) \pm 2.36(-3)
70857	5.91(-1) \pm 9.43(-3)	1.65(-1) \pm 3.97(-2)	3.39(+0) \pm 2.59(-1)	3.13(-1) \pm 4.62(-3)	9.49(-2) \pm 2.27(-3)
71181	6.92(-1) \pm 9.04(-3)	1.59(-1) \pm 8.79(-3)	3.85(+0) \pm 3.34(-1)	3.49(-1) \pm 4.82(-3)	1.03(-1) \pm 2.28(-3)
71681					
71683					
71908	5.08(+0) \pm 1.93(-2)	1.18(+0) \pm 3.31(-2)	2.23(+1) \pm 3.86(+0)	2.58(+0) \pm 2.85(-2)	7.77(-1) \pm 1.50(-2)
72567	9.19(-1) \pm 1.08(-2)	2.80(-1) \pm 3.16(-2)	5.17(+0) \pm 4.00(-1)	4.73(-1) \pm 6.53(-3)	1.42(-1) \pm 2.89(-3)
72603	1.29(+0) \pm 1.59(-2)	3.32(-1) \pm 2.84(-2)	7.21(+0) \pm 6.52(-1)	6.48(-1) \pm 8.36(-3)	1.92(-1) \pm 4.25(-3)
72848	1.53(+0) \pm 1.11(-2)	3.84(-1) \pm 1.88(-2)	8.70(+0) \pm 8.99(-1)	7.96(-1) \pm 1.03(-2)	2.39(-1) \pm 4.40(-3)
73100	9.87(-1) \pm 6.41(-3)	2.03(-1) \pm 9.95(-3)	5.50(+0) \pm 4.67(-1)	5.00(-1) \pm 6.90(-3)	1.55(-1) \pm 2.99(-3)
73182					
73184			1.67(+1) \pm 1.85(-1)	1.65(+0) \pm 1.06(-2)	5.22(-1) \pm 9.14(-3)
73996	1.56(+0) \pm 1.02(-2)	3.44(-1) \pm 1.92(-2)	8.35(+0) \pm 7.63(-1)	8.08(-1) \pm 1.12(-2)	2.40(-1) \pm 4.64(-3)
77052	1.21(+0) \pm 1.07(-2)	3.06(-1) \pm 2.36(-2)	6.84(+0) \pm 6.12(-1)	6.26(-1) \pm 8.65(-3)	1.82(-1) \pm 4.03(-3)
78459	1.57(+0) \pm 5.03(-3)	3.85(-1) \pm 2.86(-2)	8.49(+0) \pm 8.14(-1)	7.96(-1) \pm 1.10(-2)	2.39(-1) \pm 4.62(-3)
78775	7.11(-1) \pm 9.99(-3)	1.35(-1) \pm 2.86(-2)	3.90(+0) \pm 3.09(-1)	3.59(-1) \pm 4.62(-3)	1.06(-1) \pm 2.34(-3)
79248	7.27(-1) \pm 2.94(-2)	1.75(-1) \pm 1.30(-2)	4.02(+0) \pm 3.04(-1)	3.76(-1) \pm 4.85(-3)	1.11(-1) \pm 2.36(-3)
80725	6.40(-1) \pm 1.44(-2)		3.50(+0) \pm 2.45(-1)	3.27(-1) \pm 4.82(-3)	9.39(-2) \pm 2.34(-3)
82860	2.06(+0) \pm 8.52(-3)	4.84(-1) \pm 7.03(-3)	1.13(+1) \pm 1.15(+0)	1.09(+0) \pm 1.41(-2)	3.14(-1) \pm 4.91(-3)
83389	5.73(-1) \pm 5.17(-3)	9.64(-2) \pm 7.25(-3)	3.05(+0) \pm 2.14(-1)	2.86(-1) \pm 3.95(-3)	8.47(-2) \pm 2.03(-3)
84862	1.68(+0) \pm 7.42(-3)	3.93(-1) \pm 2.39(-2)	9.38(+0) \pm 9.61(-1)	8.64(-1) \pm 1.19(-2)	2.55(-1) \pm 4.69(-3)
85235	8.69(-1) \pm 4.33(-3)	1.99(-1) \pm 7.31(-3)	4.86(+0) \pm 4.13(-1)	4.54(-1) \pm 5.85(-3)	1.33(-1) \pm 2.45(-3)
85295		3.22(-1) \pm 2.19(-2)	6.82(+0) \pm 6.29(-1)	6.85(-1) \pm 8.83(-3)	2.05(-1) \pm 4.54(-3)
86036	1.93(+0) \pm 7.07(-3)	4.62(-1) \pm 1.19(-2)	1.05(+1) \pm 1.16(+0)	1.01(+0) \pm 1.30(-2)	2.97(-1) \pm 5.20(-3)
86796	2.08(+0) \pm 2.16(-2)	5.24(-1) \pm 4.59(-3)	1.02(+1) \pm 5.25(-1)	1.19(+0) \pm 8.77(-3)	3.01(-1) \pm 5.55(-3)
88601	1.03(+1) \pm 1.16(-1)	2.27(+0) \pm 3.59(-2)	3.38(+1) \pm 6.22(-1)	5.96(+0) \pm 4.39(-2)	1.51(+0) \pm 2.08(-2)
88972	1.14(+0) \pm 1.32(-2)	3.15(-1) \pm 3.48(-2)	6.54(+0) \pm 5.25(-1)	5.94(-1) \pm 7.65(-3)	1.73(-1) \pm 3.67(-3)
89042	1.37(+0) \pm 1.15(-2)	3.22(-1) \pm 3.43(-2)	7.88(+0) \pm 6.90(-1)	7.60(-1) \pm 9.80(-3)	2.06(-1) \pm 4.36(-3)
91009	7.07(-1) \pm 1.12(-2)	1.32(-1) \pm 1.34(-2)	3.58(+0) \pm 2.47(-1)	3.63(-1) \pm 4.68(-3)	1.14(-1) \pm 2.30(-3)
92043	3.34(+0) \pm 8.22(-3)	7.70(-1) \pm 4.36(-2)	1.69(+1) \pm 1.92(+0)	1.84(+0) \pm 1.69(-2)	5.15(-1) \pm 7.12(-3)
95995	8.83(-1) \pm 8.39(-3)	2.28(-1) \pm 9.66(-3)	5.07(+0) \pm 4.16(-1)	4.72(-1) \pm 6.09(-3)	1.37(-1) \pm 2.78(-3)
96100			2.36(+1) \pm 2.81(+0)	2.23(+0) \pm 1.64(-2)	6.63(-1) \pm 9.17(-3)
96441	2.20(+0) \pm 1.53(-2)	5.44(-1) \pm 1.30(-2)	1.24(+1) \pm 1.14(+0)	1.19(+0) \pm 1.53(-2)	3.62(-1) \pm 7.33(-3)
97944		3.45(-1) \pm 2.32(-2)	8.44(+0) \pm 9.03(-1)	7.98(-1) \pm 1.18(-2)	2.35(-1) \pm 5.63(-3)
98959	8.98(-1) \pm 1.48(-2)		4.79(+0) \pm 4.02(-1)	4.60(-1) \pm 6.35(-3)	1.34(-1) \pm 2.72(-3)
99240			4.31(+1) \pm 1.26(+1)	5.54(+0) \pm 3.57(-2)	1.50(+0) \pm 1.80(-2)
99461			1.72(+1) \pm 1.36(+0)	2.17(+0) \pm 1.80(-2)	5.42(-1) \pm 9.49(-3)
101955	7.86(-1) \pm 1.26(-2)	2.29(-1) \pm 1.69(-2)	4.16(+0) \pm 3.22(-1)	4.08(-1) \pm 5.64(-3)	1.21(-1) \pm 3.46(-3)
101997	8.39(-1) \pm 5.28(-3)		4.13(+0) \pm 3.16(-1)	4.13(-1) \pm 5.70(-3)	1.21(-1) \pm 3.22(-3)
103389	9.16(-1) \pm 7.03(-3)	2.09(-1) \pm 2.90(-2)	5.15(+0) \pm 3.65(-1)	4.66(-1) \pm 5.58(-3)	1.43(-1) \pm 3.41(-3)

Continued...

Table 3c. Continued.

HIP	AKARI		WISE		
	9 μm (Jy)	18 μm (Jy)	3.35 μm (W1) (Jy)	11.56 μm (W3) (Jy)	22.09 μm (W4) (Jy)
104214					
104217					
105312	$8.93(-1) \pm 1.05(-2)$	$2.01(-1) \pm 3.55(-2)$	$4.90(+0) \pm 4.02(-1)$	$4.44(-1) \pm 6.13(-3)$	$1.34(-1) \pm 3.08(-3)$
106696	$5.88(-1) \pm 1.25(-2)$	$1.90(-1) \pm 2.43(-2)$	$3.25(+0) \pm 2.04(-1)$	$2.91(-1) \pm 3.75(-3)$	$8.57(-2) \pm 2.37(-3)$
107350	$8.70(-1) \pm 1.01(-2)$	$1.93(-1) \pm 2.91(-2)$	$4.62(+0) \pm 3.32(-1)$	$4.37(-1) \pm 6.04(-3)$	$1.33(-1) \pm 3.30(-3)$
107649	$1.24(+0) \pm 1.72(-2)$	$2.62(-1) \pm 3.06(-2)$	$7.07(+0) \pm 5.93(-1)$	$6.35(-1) \pm 8.19(-3)$	$1.96(-1) \pm 4.50(-3)$
108870					
109378	$6.55(-1) \pm 3.44(-3)$		$3.65(+0) \pm 2.42(-1)$	$3.35(-1) \pm 4.94(-3)$	$9.83(-2) \pm 2.45(-3)$
109422	$1.69(+0) \pm 3.42(-2)$	$3.95(-1) \pm 1.84(-3)$	$7.65(+0) \pm 3.17(-1)$	$1.17(+0) \pm 1.83(-2)$	$2.63(-1) \pm 5.81(-3)$
110109	$1.74(+0) \pm 1.42(-2)$	$4.17(-1) \pm 2.61(-2)$	$9.88(+0) \pm 9.20(-1)$	$8.93(-1) \pm 1.23(-2)$	$2.66(-1) \pm 5.39(-3)$
113357	$1.49(+0) \pm 4.61(-3)$	$3.23(-1) \pm 1.52(-2)$	$8.60(+0) \pm 8.56(-1)$	$7.80(-1) \pm 1.08(-2)$	$2.25(-1) \pm 4.56(-3)$
113576	$1.02(+0) \pm 7.00(-3)$	$2.09(-1) \pm 6.30(-2)$	$5.21(+0) \pm 4.18(-1)$	$5.20(-1) \pm 7.19(-3)$	$1.59(-1) \pm 3.81(-3)$
114948	$9.52(-1) \pm 7.55(-3)$	$2.27(-1) \pm 2.70(-2)$	$5.19(+0) \pm 4.21(-1)$	$5.00(-1) \pm 6.45(-3)$	$1.64(-1) \pm 3.47(-3)$
116745	$8.22(-1) \pm 1.24(-2)$	$2.56(-1) \pm 3.42(-2)$	$4.54(+0) \pm 2.01(-1)$	$4.16(-1) \pm 6.51(-3)$	$1.30(-1) \pm 2.87(-3)$
120005			$9.30(+0) \pm 6.68(-1)$		

Table 3d. IRAS and *Spitzer*/MIPS fluxes.

HIP	IRAS						MIPS	
	12 μm (Jy)	%	25 μm (Jy)	%	60 μm (Jy)	%	24 μm (Jy)	70 μm (Jy)
171	1.25(+0)	7	2.96(-1)	17			2.12(-1) \pm 4.32(-3)	4.41(-2) \pm 1.36(-2)
544	7.67(-1)	6	2.27(-1)	12			1.55(-1) \pm 3.16(-3)	1.03(-1) \pm 7.83(-3)
910	1.50(+0)	7	2.43(-1)	20			2.49(-1) \pm 5.08(-3)	3.75(-2) \pm 4.48(-3)
2941	1.27(+0)	7	2.57(-1)	15			1.99(-1) \pm 4.05(-3)	2.58(-2) \pm 1.19(-2)
3093	1.03(+0)	8	2.57(-1)	14			1.92(-1) \pm 3.92(-3)	1.49(-2) \pm 5.69(-3)
3497	4.22(-1)	6	9.48(-2)	18			7.54(-2) \pm 1.54(-3)	5.20(-3) \pm 4.41(-3)
3821	7.61(+0)	5	1.75(+0)	6			1.11(+0) \pm 2.27(-2)	1.22(-1) \pm 1.07(-2)
3909	1.12(+0)	7	3.09(-1)	25			1.89(-1) \pm 3.85(-3)	2.43(-2) \pm 3.50(-3)
4148	3.79(-1)	13	1.10(-1)	33			7.83(-2) \pm 1.60(-3)	3.71(-2) \pm 6.59(-3)
7513	3.12(+0)	5	7.27(-1)	7			5.01(-1) \pm 1.02(-2)	5.57(-2) \pm 6.33(-3)
7978	8.14(-1)	6	2.82(-1)	13	8.15(-1)	13	1.85(-1) \pm 3.77(-3)	8.63(-1) \pm 5.87(-2)
8768	3.49(-1)	9					6.90(-2) \pm 1.41(-3)	2.47(-2) \pm 7.97(-3)
10138	9.15(-1)	5	1.84(-1)	13			1.54(-1) \pm 3.14(-3)	6.90(-3) \pm 6.82(-3)
10798	6.74(-1)	7	1.50(-1)	21			1.06(-1) \pm 2.17(-3)	1.45(-2) \pm 2.78(-3)
11452	3.85(-1)	9					6.18(-2) \pm 1.26(-3)	
11964	4.94(-1)	5	1.55(-1)	13			9.93(-2) \pm 2.03(-3)	9.60(-3) \pm 8.82(-3)
12777	2.54(+0)	6	5.52(-1)	14			4.06(-1) \pm 8.28(-3)	5.40(-2) \pm 6.43(-3)
13402	1.01(+0)	5	2.65(-1)	16			1.84(-1) \pm 3.76(-3)	6.77(-2) \pm 7.06(-3)
14954	1.39(+0)	6	3.16(-1)	19			2.18(-1) \pm 4.45(-3)	4.25(-2) \pm 4.76(-3)
15330	1.07(+0)	4	2.83(-1)	9			1.85(-1) \pm 3.77(-3)	3.00(-2) \pm 4.66(-3)
15371	1.18(+0)	5	2.92(-1)	10			2.22(-1) \pm 4.52(-3)	4.54(-2) \pm 4.95(-3)
15799	5.40(-1)	9	1.26(-1)	21			9.74(-2) \pm 1.99(-3)	1.27(-2) \pm 4.68(-3)
16134	3.87(-1)	8	1.34(-1)	20			7.14(-2) \pm 1.46(-3)	1.05(-2) \pm 4.46(-3)
17420	4.94(-1)	7	1.23(-1)	22			8.22(-2) \pm 1.68(-3)	2.36(-2) \pm 5.44(-3)
17439	4.28(-1)	6	1.18(-1)	16	1.36(-1)	24	7.59(-2) \pm 1.55(-3)	8.85(-2) \pm 7.46(-3)
19849	4.97(+0)	6	1.14(+0)	9			7.20(-1) \pm 1.47(-2)	8.26(-2) \pm 6.68(-3)
19884	4.58(-1)	6	1.15(-1)	15			7.84(-2) \pm 1.60(-3)	1.21(-2) \pm 3.30(-3)
22263	1.12(+0)	5	2.24(-1)	12			1.86(-1) \pm 3.80(-3)	1.14(-1) \pm 8.53(-3)
23311	1.31(+0)	5	2.79(-1)	12			2.14(-1) \pm 4.37(-3)	2.57(-2) \pm 5.20(-3)
25110	1.11(+0)	5	2.45(-1)	9			1.82(-1) \pm 3.71(-3)	3.26(-2) \pm 5.46(-3)
27887	5.03(-1)	5	1.03(-1)	14			8.85(-2) \pm 1.81(-3)	1.72(-2) \pm 4.94(-3)
28103	2.88(+0)	4	7.26(-1)	5	2.12(-1)	22	5.36(-1) \pm 1.09(-2)	9.39(-2) \pm 7.76(-3)
28442	4.72(-1)	6	1.16(-1)	15			7.95(-2) \pm 1.62(-3)	7.50(-3) \pm 3.93(-3)
29271	1.74(+0)	3	4.01(-1)	5			3.03(-1) \pm 6.17(-3)	4.26(-2) \pm 1.05(-2)
29568	5.67(-1)	5	1.42(-1)	12			9.11(-2) \pm 1.86(-3)	1.53(-2) \pm 2.34(-3)
32439	8.87(-1)	5	2.18(-1)	13			1.47(-1) \pm 3.01(-3)	1.58(-2) \pm 2.72(-3)
32480	1.46(+0)	6	4.12(-1)	10	3.81(-1)	13	1.93(-1) \pm 3.94(-3)	2.63(-1) \pm 1.83(-2)
33277	7.90(-1)	6					1.30(-1) \pm 2.66(-3)	1.31(-2) \pm 1.01(-2)
34017	6.90(-1)	7					1.12(-1) \pm 2.29(-3)	1.44(-2) \pm 4.02(-3)
34065	1.42(+0)	4	3.33(-1)	7			1.69(-1) \pm 3.44(-3)	2.05(-2) \pm 2.77(-3)
35136	9.62(-1)	5	2.52(-1)	12			1.64(-1) \pm 3.34(-3)	2.89(-2) \pm 4.63(-3)
36439	8.86(-1)	5	2.14(-1)	14			1.46(-1) \pm 2.98(-3)	1.44(-2) \pm 2.96(-3)
38382	1.28(+0)	8	2.84(-1)	19			2.46(-1) \pm 5.02(-3)	1.34(-2) \pm 4.30(-3)
38784	4.61(-1)	6	9.72(-2)	23			8.09(-2) \pm 1.65(-3)	1.06(-2) \pm 2.99(-3)
40693	9.67(-1)	6	3.41(-1)	11			2.30(-1) \pm 4.69(-3)	1.51(-2) \pm 2.42(-3)
40843	1.14(+0)	18	2.74(-1)	22			1.87(-1) \pm 3.82(-3)	3.25(-2) \pm 5.27(-3)
42430	1.78(+0)	4	3.80(-1)	7	1.52(-1)	25	2.93(-1) \pm 5.98(-3)	3.11(-2) \pm 6.07(-3)
42438	8.85(-1)	7	2.08(-1)	16			1.56(-1) \pm 3.19(-3)	4.12(-2) \pm 4.16(-3)
43587	9.81(-1)	5	2.41(-1)	26			1.69(-1) \pm 3.45(-3)	1.98(-2) \pm 4.41(-3)
43726	6.68(-1)	5	1.64(-1)	17			1.19(-1) \pm 2.43(-3)	3.25(-2) \pm 4.13(-3)
44897	5.91(-1)	8					1.06(-1) \pm 2.17(-3)	1.87(-2) \pm 4.00(-3)
45333	1.45(+0)	5	3.36(-1)	8			2.39(-1) \pm 4.88(-3)	2.39(-2) \pm 5.25(-3)
45617	5.23(-1)	8					8.62(-2) \pm 1.76(-3)	2.50(-3) \pm 1.04(-2)
46580	4.74(-1)	7	1.74(-1)	27			8.51(-2) \pm 1.74(-3)	
47592	1.48(+0)	6	3.57(-1)	10			2.42(-1) \pm 4.93(-3)	1.46(-2) \pm 1.14(-2)
49081	1.22(+0)	6	2.47(-1)	18			1.96(-1) \pm 4.00(-3)	
49908	2.30(+0)	6	5.85(-1)	7			4.19(-1) \pm 8.55(-3)	3.87(-2) \pm 4.69(-3)
51459	1.68(+0)	4	3.91(-1)	7			2.67(-1) \pm 5.45(-3)	3.38(-2) \pm 4.43(-3)
51502	8.15(-1)	5	2.01(-1)	10			1.41(-1) \pm 2.88(-3)	3.96(-2) \pm 3.79(-3)

Continued...

Table 3d. Continued.

HIP	IRAS			MIPS				
	12 μm (Jy)	%	25 μm (Jy)	%	60 μm (Jy)	%	24 μm (Jy)	70 μm (Jy)
53721	1.59(+0)	5	3.10(-1)	9			2.54(-1) \pm 5.18(-3)	3.14(-2) \pm 4.17(-3)
54646	6.44(-1)	8					7.55(-2) \pm 1.54(-3)	1.80(-2) \pm 1.04(-2)
56452	1.13(+0)	7	2.74(-1)	18			1.79(-1) \pm 3.66(-3)	2.32(-2) \pm 2.95(-3)
57507	4.82(-1)	10					8.28(-2) \pm 1.69(-3)	1.19(-2) \pm 3.59(-3)
57939							1.26(-1) \pm 2.57(-3)	1.07(-2) \pm 2.31(-3)
58345	8.48(-1)	7	1.95(-1)	29			1.40(-1) \pm 2.86(-3)	9.00(-3) \pm 8.02(-3)
62145							8.95(-2) \pm 1.83(-3)	2.89(-2) \pm 2.01(-2)
62207	6.59(-1)	8	1.59(-1)	28			1.11(-1) \pm 2.25(-3)	5.57(-2) \pm 5.20(-3)
62523	5.60(-1)	9	1.53(-1)	28			9.55(-2) \pm 1.95(-3)	1.35(-2) \pm 3.62(-3)
64792	1.29(+0)	6	2.67(-1)	14			2.16(-1) \pm 4.40(-3)	1.91(-2) \pm 5.75(-3)
64797	1.04(+0)	8	2.77(-1)	21			1.53(-1) \pm 3.12(-3)	4.68(-2) \pm 1.65(-2)
65026	6.73(-1)	8	2.01(-1)	17			1.51(-1) \pm 3.08(-3)	2.51(-2) \pm 1.01(-2)
65721	2.28(+0)	7	5.37(-1)	10			3.62(-1) \pm 7.38(-3)	7.90(-2) \pm 8.09(-3)
67275	1.97(+0)	7	4.85(-1)	15			3.28(-1) \pm 6.69(-3)	3.32(-2) \pm 6.78(-3)
67422	8.36(-1)	6	1.78(-1)	15			7.67(-2) \pm 1.56(-3)	3.11(-2) \pm 1.04(-2)
67620	6.11(-1)	7	1.84(-1)	24			9.70(-2) \pm 1.98(-3)	8.60(-3) \pm 3.45(-3)
68184	9.48(-1)	5	2.10(-1)	11			1.69(-1) \pm 3.44(-3)	1.81(-2) \pm 6.71(-3)
68682	7.43(-1)	6	1.91(-1)	21			1.20(-1) \pm 2.45(-3)	1.61(-2) \pm 1.40(-2)
69965	6.03(-1)	8	2.43(-1)	20			1.11(-1) \pm 2.26(-3)	1.95(-2) \pm 9.29(-3)
70319	5.27(-1)	7					9.57(-2) \pm 1.95(-3)	1.16(-2) \pm 6.35(-3)
70857	4.40(-1)	5	1.11(-1)	14			7.81(-2) \pm 1.59(-3)	6.50(-3) \pm 4.62(-3)
71181	4.88(-1)	6	1.20(-1)	14			8.32(-2) \pm 1.70(-3)	2.92(-2) \pm 8.04(-3)
71681							1.55(+1) \pm 3.16(-1)	1.01(+0) \pm 6.68(-1)
71683							2.85(+1) \pm 5.82(-1)	3.39(+0) \pm 7.02(-1)
71908	4.07(+0)	15	8.21(-1)	15			6.70(-1) \pm 1.37(-2)	
72567	6.63(-1)	6	1.07(-1)	21			1.16(-1) \pm 2.36(-3)	1.08(-2) \pm 2.89(-3)
72603	1.07(+0)	7						
72848	1.13(+0)	11	2.81(-1)	17			1.93(-1) \pm 3.93(-3)	3.35(-2) \pm 6.41(-3)
73100	7.30(-1)	4	1.75(-1)	8			1.27(-1) \pm 2.59(-3)	2.47(-2) \pm 3.17(-3)
73182							2.63(-1) \pm 5.36(-3)	1.60(-2) \pm 3.19(-3)
73184							3.96(-1) \pm 8.08(-3)	4.73(-2) \pm 4.37(-3)
73996	1.12(+0)	5	2.47(-1)	11			1.96(-1) \pm 4.00(-3)	3.32(-2) \pm 5.84(-3)
77052	8.47(-1)	6	2.32(-1)	15			1.50(-1) \pm 3.07(-3)	1.11(-2) \pm 5.25(-3)
78459	1.10(+0)	5	2.65(-1)	8			1.97(-1) \pm 4.01(-3)	2.96(-2) \pm 5.76(-3)
78775	4.86(-1)	6	1.25(-1)	15			7.88(-2) \pm 1.61(-3)	8.70(-3) \pm 3.55(-3)
79248	5.53(-1)	6	1.21(-1)	13			9.05(-2) \pm 1.85(-3)	1.06(-2) \pm 2.60(-3)
80725	4.49(-1)	7					7.75(-2) \pm 1.58(-3)	3.73(-2) \pm 1.76(-2)
82860	1.51(+0)	4	3.58(-1)	5			2.69(-1) \pm 5.49(-3)	4.47(-2) \pm 6.01(-3)
83389	3.89(-1)	7	1.08(-1)	22			6.82(-2) \pm 1.39(-3)	1.10(-2) \pm 9.03(-3)
84862	1.23(+0)	4	2.75(-1)	8			2.10(-1) \pm 4.29(-3)	2.46(-2) \pm 4.33(-3)
85235	6.15(-1)	5	1.52(-1)	11			1.08(-1) \pm 2.20(-3)	5.80(-2) \pm 4.92(-3)
85295	1.02(+0)	7	1.57(-1)	20			1.70(-1) \pm 3.46(-3)	1.38(-2) \pm 4.59(-3)
86036	1.37(+0)	3	3.02(-1)	5			2.50(-1) \pm 5.09(-3)	2.74(-2) \pm 4.77(-3)
86796	1.54(+0)	7	4.49(-1)	14			2.60(-1) \pm 5.30(-3)	3.10(-2) \pm 8.07(-3)
88601	7.64(+0)	5	1.80(+0)	6			1.24(+0) \pm 2.54(-2)	1.44(-1) \pm 1.68(-2)
88972	8.53(-1)	3	1.86(-1)	9			1.43(-1) \pm 2.91(-3)	8.60(-3) \pm 3.65(-3)
89042	9.96(-1)	5	2.20(-1)	12			1.68(-1) \pm 3.42(-3)	1.71(-2) \pm 3.59(-3)
91009	5.52(-1)	6	1.33(-1)	13			9.39(-2) \pm 1.92(-3)	6.40(-3) \pm 5.32(-3)
92043	2.47(+0)	4	6.02(-1)	5			4.35(-1) \pm 8.87(-3)	6.98(-2) \pm 8.93(-3)
95995	6.46(-1)	3	1.56(-1)	8			1.14(-1) \pm 2.33(-3)	1.27(-2) \pm 5.37(-3)
96100	3.39(+0)	3	7.74(-1)	4			5.40(-1) \pm 1.10(-2)	7.32(-2) \pm 7.23(-3)
96441	1.63(+0)	6	3.10(-1)	14			2.78(-1) \pm 5.67(-3)	3.68(-2) \pm 4.05(-3)
97944	1.19(+0)	6	2.94(-1)	18			1.98(-1) \pm 4.03(-3)	
98959	6.83(-1)	7	1.46(-1)	15			1.02(-1) \pm 2.07(-3)	1.90(-2) \pm 3.63(-3)
99240	7.00(+0)	5	1.67(+0)	6	2.28(-1)	19	1.19(+0) \pm 2.43(-2)	1.39(-1) \pm 1.07(-2)
99461	2.71(+0)	5	6.30(-1)	9			4.42(-1) \pm 9.02(-3)	4.85(-2) \pm 1.08(-2)
101955	6.02(-1)	6	1.98(-1)	24			1.02(-1) \pm 2.08(-3)	1.15(-2) \pm 7.04(-3)
101997	5.05(-1)	8					1.01(-1) \pm 2.06(-3)	7.40(-3) \pm 3.73(-3)
103389	7.12(-1)	9					1.16(-1) \pm 2.37(-3)	4.66(-2) \pm 4.93(-3)

Continued...

Table 3d. Continued.

HIP	IRAS						MIPS	
	12 μm (Jy)	%	25 μm (Jy)	%	60 μm (Jy)	%	24 μm (Jy)	70 μm (Jy)
104214							$9.58(-1) \pm 1.95(-2)$	$6.42(-2) \pm 1.27(-2)$
104217							$7.42(-1) \pm 1.51(-2)$	$8.33(-2) \pm 1.32(-2)$
105312	5.35(-1)	9	1.51(-1)	21			$1.10(-1) \pm 2.25(-3)$	$1.36(-2) \pm 5.67(-3)$
106696	4.79(-1)	9	1.25(-1)	25			$7.27(-2) \pm 1.48(-3)$	$1.92(-2) \pm 5.26(-3)$
107350	6.46(-1)	7	1.30(-1)	20			$1.07(-1) \pm 2.18(-3)$	$2.84(-2) \pm 3.15(-3)$
107649	8.97(-1)	6	2.00(-1)	12	3.01(-1)	14	$1.55(-1) \pm 3.16(-3)$	$2.78(-1) \pm 2.15(-2)$
108870	5.68(+0)	5	1.37(+0)	5	1.79(-1)	23	$9.76(-1) \pm 1.99(-2)$	$1.11(-1) \pm 9.47(-3)$
109378	5.28(-1)	9					$8.19(-2) \pm 1.67(-3)$	$7.90(-3) \pm 2.26(-3)$
109422	1.20(+0)	5	2.97(-1)	12			$2.13(-1) \pm 4.35(-3)$	$1.06(-2) \pm 5.65(-3)$
110109	1.31(+0)	5	3.15(-1)	10			$2.23(-1) \pm 4.55(-3)$	$2.81(-2) \pm 5.72(-3)$
113357	1.08(+0)	6	2.45(-1)	13			$1.86(-1) \pm 3.79(-3)$	$2.81(-2) \pm 4.88(-3)$
113576	6.71(-1)	9	2.63(-1)	23			$1.27(-1) \pm 2.60(-3)$	$1.91(-2) \pm 2.90(-3)$
114948	7.39(-1)	6	1.81(-1)	14			$1.33(-1) \pm 2.72(-3)$	$6.87(-2) \pm 5.51(-3)$
116745	5.89(-1)	6	1.22(-1)	18			$1.02(-1) \pm 2.09(-3)$	$1.72(-2) \pm 2.49(-3)$
120005							$1.87(-1) \pm 3.81(-3)$	$2.13(-2) \pm 2.71(-3)$

Notes: IRAS data are from the Faint Source Catalogue, except those in italics that are from the Point Source catalogue.

Table 4. Stellar parameters of the DUNES sources.

HIP	SpT	T_{eff} (K)	$\log g$ (cm/s^2)	[Fe/H] (dex)	$v \sin i$ (km/s)	Lbol (L_{\odot})	Lx/Lbol (log)	AgeX (Gyr)	$\log R'_{\text{HK}}$	Age (Ca II) (Gyr)
171	G3V	5681	4.86	-0.52	1.8	0.614	-5.9	3.12	-4.851	3.96
544	K0V	5577	4.58	0.12	3.4	0.616	-4.4	0.32	-4.328	0.17
910	F5V	6160	4.01	-0.38	3.8	3.151	-7.6	12.53	-4.788	3.04
2941	K1V+...	5509	4.23	-0.14	1.6:	1.258			-4.903	4.83
3093	K0V	5204	4.45	0.16	1.15	0.529	-6.0	4.53	-4.991	6.43
3497	G3V	5670	4.48	-0.24	3.0:	1.012	-7.6	<15	-4.853	4.00
3821	G0V SB	5932	4.42	-0.23	3.3	1.209	-6.2	3.62	-4.991	6.43
3909	F7IV-V	6271	4.47	-0.05	3.0	1.697	-5.9	1.55	-4.78	2.93
4148	K2V	4940	4.70	-0.15	2.0:	0.297	-5.2	1.79	-4.83	3.64
7513	F8V	6155	4.13	0.10	9.0	3.363	-6.6	2.90	-5.035	7.26
7978	F8V	6155	4.48	-0.04	5.61	1.523	-5.4	0.96	-4.675	1.74
8768	K5/M0V	3865				0.077	-4.6	2.03	-4.59	
10138	K0V	5165	4.56	-0.22		0.406	-5.7	3.57	-4.68	1.79
10798	G8V	5371	4.62	-0.46	3.0:	0.435			-4.997	6.54
11452	K7V:	3921				0.210				
11964	K7V SB	3790				0.092	-2.8	0.18	-3.997	
12777	F7V	6314	4.31	0.03	9.0	2.250	-6.0	1.44	-5.071	7.92
13402	K1V	5217	4.57	0.10	6.3	0.392	-4.3	0.40	-4.3	0.14
14954	F8V	6187	4.24	0.21	8.5	3.848	-6.0	1.17	-4.95	5.67
15330	G2V	5716	4.57	-0.22	2.7	0.761	-5.4	1.32	-4.86	4.11
15371	G1V	5851	4.51	-0.23	0.3	0.972	-6.7	7.83	-4.827	3.59
15799	K0V	5087	4.43	0.12	1.2	0.535	-4.3	0.36	-4.773	2.84
16134	K5V	3995	*	-0.13	2.0	0.136	-4.6	1.44	-4.35	
17420	K2V	4990	4.52	-0.12	9.9	0.294	-5.0	1.35	-5.04	
17439	K1V	5166	4.44	0.05	2.9	0.402	-4.9	0.93	-4.534	0.76
19849	K1V	5150	4.52	-0.24	1.0	0.416	-5.6	2.69	-4.872	4.30
19884	K5V	4473	*	0.06	1.0	0.203	-5.2	2.54	-4.905	
22263	G3V	5814	4.47	0.01	2.9	0.951	-4.8	0.44	-4.61	1.21
23311	K3V	4827	4.69	0.3	1.1	0.276	-5.9	5.09	-5.29	
25110	F6V	6307	4.17	0.10	7.7:	3.224	-5.9	1.21	-5.216	
27887	K3V	4870	4.49	-0.29	3.0:	0.252	-5.9	6.65	-5.037	2.60
28103	F1V	7000	4.12	-0.11	15.7	5.562	-5.8	0.64	-4.78	
28442	K3/K4V	4330				0.290			-4.932	
29271	G5V	5591	4.46	0.08		0.847	-6.1	3.37	-4.94	5.49
29568	G5V	5633	4.48	-0.01	6.0:	0.692	-4.5	0.36	-4.39	0.28
32439	F8V	6191	4.36	-0.26	5.0:	1.710	-5.9	1.65	-5.024	7.05
32480	G0V	6086	4.35	0.09	5.0:	1.752	-5.8	1.38	-4.985	6.32
33277	G0V	5891	4.36	-0.13	4.0:	1.251			-4.938	5.45
34017	G4V	5887	4.34	-0.12	4.0:	1.298			-4.943	5.54
34065	G3V...	5826	4.41	-0.17	4.0:	1.372			-4.981	6.24
35136	G0V	5917	4.26	-0.35	4.0:	1.444	-8.2	>15	-4.927	5.25
36439	F6V	6309	4.16	-0.32	10.0	2.357			-5.306	
38382	G2V	5860	4.25	-0.13	4.8	1.973			-4.883	4.49
38784	G8V	5502	4.52	-0.08	2.0:	0.638	-5.8	3.03	-4.837	3.75
40693	K0V	5405	4.46	-0.04	3.1	0.595	-5.9	3.27	-4.991	6.43
40843	F6V	6241	4.16	-0.23	3.9	2.371			-5.187	
42430	G3/G5V	5526	3.93	0.31	3.8	3.208	-6.1	1.55	-5.031	7.18
42438	G1.5Vb	5807	4.42	-0.11	9.8	0.970	-4.5	0.31	-4.38	0.26
43587	G8V	5295	4.47	0.36	2.3	0.602	-6.7	11.19	-5.099	8.43
43726	G3V	5789	4.51	0.09	1.6	1.009	-5.3	0.89	-4.659	1.60
44897	F9V	5980	4.45	0.03	4.0:	1.258	-4.7	0.37	-4.608	1.20
45333	F9V	5907	4.01	0.00	4.0:	2.705			-5.073	7.96
45617	K3V	4639	4.39	-0.22	6.1	0.485	-5.3	1.56	-4.51	
46580	K3V	4868	4.8	-0.04	1.7	0.241	-4.6	0.91	-4.27	
47592	G0V	6160	4.33	-0.06	6.0:	1.934	-6.6	4.75	-4.862	4.14
49081	G1V	5759	4.34	0.19	2.2	1.375			-4.969	6.02
49908	K8V	4081	4.71	-0.16	2.6	0.125	-5.0	3.21	-5	
51459	F8V	6137	4.33	-0.10	2.0:	1.554	-5.6	1.03	-4.783	2.97
51502	F2V	6710	4.32	-0.26	56.2	2.840	-4.9	0.30	-4.55	
53721	G0V	5908	4.37	0.03	3.2	1.600	-8.3	>15	-4.909	4.93

Continued...

Table 4. Continued.

HIP	SpT	T_{eff} (K)	$\log g$ (cm/s^2)	[Fe/H] (dex)	$v \sin i$ (km/s)	Lbol L_{\odot}	Lx/Lbol (log)	AgeX (Gyr)	$\log R'_{\text{HK}}$	Age (Ca II) (Gyr)
54646	K8V	3783	5.0	-1.5	2.7	0.166	-4.9	2.40	-4.86	
56452	K0V	5189	4.68	-0.32	4.0	0.368	-6.2	7.78	-4.907	4.90
57507	G5V	5559	4.47	-0.26	3.0:	0.690			-4.924	5.20
57939	G8Vp	5052	4.70	-1.27	4.0:	0.228	-6.4	13.30	-4.896	4.71
58345	K4V	4510	4.57	0.16	4.0:	0.218	-5.2	2.30	-4.868	
62145	K3V	5018	4.40	0.08	4.8	0.359	-4.7	0.80	-4.79	
62207	G0V	5860	4.33	-0.53	3.0:	1.055			-4.981	6.24
62523	G7V	5643	4.52	0.08	2.9	0.758	-5.1	0.82	-4.43	0.37
64792	G0Vs	6118	4.32	0.16	7.0	2.092	-4.4	0.16	-4.443	0.41
64797	K2V	4952	4.55	-0.15		0.330	-5.0	1.25	-4.63	1.36
65026	K0	3752				0.120	-4.9	2.74	-4.5226	6
65721	G5V	5513	3.94	-0.07	2.7	2.989	-7.0	5.57	-5.069	7.89
67275	F7V	6376	4.21	0.26	15.0	3.062	-5.1	0.37	-4.731	2.32
67422	K2	4729	5.09	-0.35	5.2	0.320	-4.9	1.06	-4.771	
67620	G5V	5751	4.52	0.05	3.0:	0.869	-5.4	1.26	-4.703	2.02
68184	K3V	4757	4.58	0.10		0.296	-6.1	7.18	-5.12	
68682	G8V	5509	4.39	0.00	2.0:	0.801			-4.869	4.25
69965	F7Vw	6120	4.39	-0.64	2.8	1.181			-4.641	1.45
70319	G1V	5666	4.49	-0.32	2.0:	0.812			-4.957	5.80
70857	G5	5371	4.53	-0.39	1.0:	0.646	-5.4	1.59	-4.91	4.95
71181	K3V	4809	4.67	-0.09	4.3	0.252	-5.2	2.25	-4.97	
71681	K1V	5178	4.56	0.15	1.1	0.444	-6.0	4.27	-4.923	5.18
71683	G2V	5801	4.33	0.19	2.7	1.483	-7.1	10.40	-5.059	7.70
71908	F1Vp	7645	4.24		14.0	11.263				
72567	G2V	6059	4.58	0.00	7.0:	1.223	-5.1	0.65	-4.34	0.19
72603	F3V	6598	4.18	-0.10	3.2	3.595	-5.1	0.29	-4.58	1.01
72848	K2V	5313	4.57	0.10	4.0	0.498	-4.8	0.70	-4.52	0.69
73100	F7V	6220	4.15	-0.03	6.0:	2.831	-5.9	1.15	-5.03	7.16
73182	K5V	4683	3.70	-0.24	1.0:	0.027	-5.4	5.40	-5.19	
73184	K4V	4744	4.76	0.10	1.0	0.204	-5.7	4.74	-4.63	
73996	F5V	6435	4.19	0.05	44.0	3.222	-5.4	0.49	-4.85	3.95
77052	G5V	5659	4.45	0.06	2.0:	0.844	-5.3	1.10	-4.8	3.20
78459	G2V	5833	4.29	-0.20	1.6	1.742			-5.039	7.33
78775	G8V	5214	4.71	-0.49	2.0:	0.443			-4.97	6.04
79248	K0V	5336	4.48	0.43	1.6	0.653	-6.5	7.45	-5.175	
80725	K2V	5040	4.53			0.636	-5.2	1.18	-4.69	1.89
82860	F6Vvar	6306	4.39	-0.11	9.0	2.072	-5.1	0.44	-4.737	2.39
83389	G8V	5488	4.56	-0.07	2.0:	0.617	-6.2	5.57	-4.843	3.84
84862	G0V	5712	4.32	-0.29	3.0:	1.241	-7.4		-4.963	5.91
85235	K0V	5290	4.63	-0.39	3.0:	0.413			-4.93	5.31
85295	K7V	4059	4.68	-0.03	3.0:	0.106	-4.9	2.30	-4.72	
86036	G0V	5980	4.40	0.00	4.0:	1.342	-5.0	0.56	-4.69	1.89
86796	G5V	5787	4.29	0.29	3.4	1.821	-7.8	>15	-5.101	
88601	K0V SB	5312	4.54	0.05	13.0	0.594	-5.2	1.01	-4.586	1.05
88972	K2V	5000	4.47	-0.05	1.5	0.355	-6.0	5.79	-4.955	5.76
89042	G0V	5921	4.27	-0.17	3.5	1.672			-4.935	5.40
91009	K7Vvar	4200	4.50	0.05	8.5	0.232	-3.2	0.12	-3.66	
92043	F6V	6431	4.08	0.04	18.0	6.141	-5.3	0.30	-4.898	4.74
95995	K1V	5027	4.42	-0.22	3.0	0.682			-5.047	7.48
96100	K0V	5276	4.56	-0.18	8.0:	0.427	-5.6	2.69	-4.832	3.67
96441	F4V	6954	4.04	-0.03	4.3	4.147	-5.4	0.39	-5.234	
97944	K3/K4V	4687	4.40	-0.20	4.0:	0.770	-4.7	0.49	-4.582	
98959	G2V	5735	4.46	-0.22	2.0:	1.000			-4.857	4.06
99240	G5IV-V	5597	4.29	0.30	3.2	1.246	-6.4	4.53	-5.092	8.30
99461	K2V	4964	4.48	-0.44	1.8	0.286	-6.1	8.04	-4.988	6.37
101955	K5V	4181			5.6	0.331	-5.0	1.20	-4.972	
101997	G8/K0V	5427	4.51	-0.27	2.0:	0.540			-4.948	5.63
103389	F7V	6257	4.36	-0.14	13.4	2.025	-4.7	0.26	-4.402	0.30
104214	K5V	4394	4.59	-0.25	2.0:	0.144	-5.6	6.18	-4.764	
104217	K7V	4002	4.57	-0.39	1.9	0.092	-5.6	8.45	-4.891	

Continued...

Table 4. Continued.

HIP	SpT	T_{eff} (K)	$\log g$ (cm/s^2)	[Fe/H] (dex)	$v \sin i$ (km/s)	L_{bol} L_{\odot}	L_x/L_{bol} (log)	AgeX (Gyr)	$\log R'_{\text{HK}}$	Age (Ca II) (Gyr)
105312	G5V	5479	4.45	-0.36	1.6:	0.690			-4.988	6.37
106696	K2V	5053	4.62	-0.18	1.9	0.306	-5.1	1.56	-4.702	2.01
107350	G0V	5952	4.44	-0.07	9.7	1.090	-4.4	0.24	-4.48	0.53
107649	G2V	5912	4.44	-0.01	3.0:	1.258	-5.7	1.40	-5.02	6.98
108870	K5V	4629	4.36	-0.06	2.0:	0.215	-5.5	3.66	-4.851	
109378	G0	5540	4.39	0.22	1.8	1.002			-5.101	
109422	F6V	6339	4.15	0.08	13.6	2.801			-4.823	3.53
110109	G1V	5870	4.45	-0.19	2.2	1.144	-5.6	1.32	-4.918	5.09
113357	G5V	5791	4.36	0.20	2.6	1.368	-7.1	13.58	-5.074	7.98
113576	K5/M0V	3746	5.0	-1.5	3.0:	0.124			-4.63	
114948	F7V	6249	4.31	-0.21	9.0:	1.867	-4.4	0.18	-4.434	0.38
116745	K3V	4750	4.51	-0.30		0.221	-5.5	3.44	-4.959	
120005	K2	3769	4.71	-0.40	2.9	0.086	-4.1	1.01	-4.42	

Table 5. PACS AORs.

HIP	PACS	Scan	X-Scan	Time [s]
171	100/160	1342212800	1342212801	900
544	100/160	1342213512	1342213513	1440
910	100/160	1342199875	1342199876	360
2941	100/160	1342212844	1342212845	540
3093	70/160	1342213242	1342213243	180
3093	100/160	1342213244	1342213245	540
3497	70/160	1342212704	1342212705	540
3497	100/160	1342212706	1342212707	1440
3821	100/160	1342213227	1342213228	1080
3909	100/160	1342211150	1342211151	540
4148	70/160	1342212840	1342212841	360
4148	100/160	1342212842	1342212843	1440
7513	100/160	1342223326	1342223327	360
7978	70/160	1342212838	1342212839	360
7978	100/160	1342187141		4714
7978	100/160	1342187139	1342187140	720
8768	70/160	1342213645	1342213646	180
8768	100/160	1342213647	1342213648	1440
10138	70/160	1342214175	1342214176	180
10138	100/160	1342214177	1342214178	720
10798	100/160	1342214185	1342214186	1440
11452	70/160	1342223328	1342223329	180
11452	100/160	1342223330	1342223331	1440
11964	70/160	1342221280	1342221281	180
11964	100/160	1342221282	1342221283	1440
12777	100/160	1342204215	1342204216	360
13402	100/160	1342215731	1342215732	1440
14954	100/160	1342216129	1342216130	1440
15330	100/160	1342204268	1342204269	720
15371	70/160	1342191104	1342191105	1440
15371	100/160	1342191102	1342191103	1440
15799	70/160	1342216117	1342216118	180
15799	100/160	1342216119	1342216120	1440
16134	100/160	1342216121	1342216122	1440
17420	70/160	1342223592	1342223593	180
17420	100/160	1342223594	1342223595	1440
17439	70/160	1342222499	1342222500	540
17439	100/160	1342222501	1342222502	1440
19849	100/160	1342204321	1342204322	900
19884	70/160	1342204264	1342204265	180
19884	100/160	1342204266	1342204267	1440
22263	100/160	1342193112	1342193113	1440
23311	100/160	1342193117	1342193118	360
25110	100/160	1342219019	1342219020	720
27887	70/160	1342203666	1342203667	180
27887	100/160	1342203668	1342203669	1440
28103	100/160	1342205198	1342205199	360
28442	70/160	1342196115	1342196116	180
28442	100/160	1342196117	1342196118	1440
29271	100/160	1342216043	1342216044	720
29568	100/160	1342204431	1342204432	1440
32439	100/160	1342196732	1342196733	1080
32480	70/160	1342219021	1342219022	180
32480	100/160	1342206334	1342206335	1440
33277	70/160	1342206326	1342206327	180
33277	100/160	1342206328	1342206329	1260
34017	100/160	1342205194	1342205195	1080
34065	100/160	1342203710	1342203711	720
35136	100/160	1342219422	1342219423	720
36439	100/160	1342195614	1342195615	1080
38382	100/160	1342196123	1342196124	360

Continued...

Table 5. Continued.

HIP	PACS	Scan	X-Scan	On-source time [s]
38784	70/160	1342196753	1342196754	180
38784	100/160	1342196755	1342196756	1440
40693	100/160	1342196125	1342196126	900
40843	100/160	1342196743	1342196744	540
42430	100/160	1342198541	1342198542	360
42438	100/160	1342196747	1342196748	1440
43587	100/160	1342208504	1342208505	720
43726	100/160	1342208478	1342208479	1440
44897	70/160	1342209375	1342209376	180
44897	100/160	1342209377	1342209378	1440
45333	100/160	1342206669	1342206670	540
45617	70/160	1342206315	1342206316	180
45617	100/160	1342206317	1342206318	1440
46580	70/160	1342209466	1342209467	180
46580	100/160	1342209465	1342209468	1440
47592	70/160	1342198545	1342198546	180
47592	100/160	1342198547	1342198548	360
49081	100/160	1342210618	1342210619	360
49908	100/160	1342210610	1342210611	1440
51459	100/160	1342210608	1342210609	360
51502	100/160	1342197013	1342197014	1440
53721	100/160	1342198845	1342198846	360
54646	70/160	1342212025	1342212026	180
54646	100/160	1342212027	1342212028	1440
56452	100/160	1342201166	1342201167	720
57507	70/160	1342212828	1342212829	180
57507	100/160	1342212830	1342212831	1440
57939	100/160	1342212048	1342212049	1440
58345	100/160	1342212826	1342212827	1080
62145	70/160	1342221293	1342221294	180
62145	100/160	1342221295	1342221296	1440
62207	100/160	1342212391	1342212392	1440
62523	100/160	1342212485	1342212486	1440
64792	100/160	1342212812	1342212813	720
64797	70/160	1342212808	1342212809	180
64797	100/160	1342212810	1342212811	1440
65026	70/160	1342198907	1342198908	180
65026	100/160	1342198909	1342198910	720
65721	100/160	1342213093	1342213094	1440
67275	100/160	1342213081	1342213082	360
67422	70/160	1342213085	1342213086	180
67422	100/160	1342213087	1342213088	1440
67620	70/160	1342213844	1342213845	180
67620	100/160	1342213846	1342213847	1080
68184	100/160	1342213225	1342213226	1440
68682	70/160	1342213594	1342213595	180
68682	100/160	1342213596	1342213597	1440
69965	70/160	1342224194	1342224195	180
69965	100/160	1342224196	1342224197	1080
70319	70/160	1342213806	1342213807	180
70319	100/160	1342213808	1342213809	1440
70857	70/160	1342197701	1342197702	180
70857	100/160	1342197703	1342197704	1440
71181	70/160	1342209500	1342209501	180
71181	100/160	1342209502	1342209503	1440
71681	100/160	1342224848	1342224849	360
71908	100/160	1342205980	1342205981	360
72567	100/160	1342213798	1342213799	1440
72603	70/160	1342214582	1342214583	180
72603	100/160	1342214584	1342214585	1440
72848	100/160	1342212768	1342212769	1440

Continued...

Table 5. Continued.

HIP	PACS	Scan	X-Scan	On-source time [s]
73100	100/160	1342209640	1342209641	1440
73184	100/160	1342204172	1342204173	720
73996	100/160	1342213796	1342213797	540
77052	100/160	1342204162	1342204163	900
78459	100/160	1342215376	1342215377	540
78775	70/160	1342205163	1342205164	180
78775	100/160	1342205165	1342205166	1440
79248	100/160	1342205996	1342205997	1440
80725	70/160	1342205157	1342205158	180
80725	100/160	1342205159	1342205160	1440
82860	100/160	1342220101	1342220102	1440
83389	70/160	1342193509	1342193510	540
83389	100/160	1342193511	1342193512	1440
84862	100/160	1342193515	1342193516	1080
85235	100/160	1342220099	1342220100	1440
85295	100/160	1342193057	1342193058	360
86036	100/160	1342195413	1342195414	540
86796	100/160	1342215572	1342215573	360
88601	100/160	1342207023	1342207024	360
88972	70/160	1342195696	1342195697	180
88972	100/160	1342195698	1342195699	1080
89042	100/160	1342207067	1342207068	720
91009	70/160	1342196781	1342196782	180
91009	100/160	1342196783	1342196784	1440
92043	70/160	1342216399	1342216400	180
92043	100/160	1342192775	1342192776	360
95995	70/160	1342197677	1342197678	180
95995	100/160	1342197679	1342197680	1260
96100	100/160	1342197771	1342197772	360
96441	100/160	1342196779	1342196780	360
97944	100/160	1342209045	1342209046	720
98959	70/160	1342208851	1342208852	180
98959	100/160	1342208853	1342208854	1440
99240	70/160	1342187075	1342187076	288
99240	100/160	1342195466	1342195467	1152
99461	100/160	1342196779	1342196780	360
101955	70/160	1342196787	1342196788	180
101955	100/160	1342196789	1342196790	1080
101997	70/160	1342193526	1342193527	180
101997	100/160	1342193528	1342193529	1440
103389	70/160	1342193157	1342193158	180
103389	100/160	1342193159	1342193160	1440
104214	100/160	1342195781	1342195782	360
105312	70/160	1342194063	1342194064	180
105312	100/160	1342194065	1342194066	1260
106696	70/160	1342196105	1342196106	180
106696	100/160	1342196107	1342196108	1260
107350	100/160	1342195779	1342195780	1440
107649	70/160	1342193163	1342193164	180
107649	100/160	1342193165	1342193166	1440
108870	100/160	1342192760	1342192761	1440
109378	100/160	1342211126	1342211127	1440
109422	100/160	1342196797	1342196798	360
110109	100/160	1342187145	1342187146	1364
113357	100/160	1342187255		1364
113576	100/160	1342198523	1342198524	900
114948	100/160	1342196803	1342196804	1440
116745	100/160	1342196805	1342196806	1440
120005	100/160	1342209360	1342209361	1440

Table 10. Optical and PACS100 equatorial positions (J2000) and the positional offset.

HIP	ICRS(2000)	PACS100	Offset(arcsec)
171	00 02 10.16 +27 04 56.1	00 02 10.57 +27 04 56.0	5.5
544	00 06 36.78 +29 01 17.4	00 06 36.79 +29 01 15.8	1.6
910	00 11 15.86 -15 28 04.7	00 11 15.88 -15 28 03.4	1.3
2941	00 37 20.70 -24 46 02.2	00 37 20.54 -24 46 03.9	2.8
3093	00 39 21.81 +21 15 01.7	00 39 21.84 +21 14 58.9	2.8
3497	00 44 39.27 -65 38 58.3	00 44 39.18 -65 38 58.8	0.7
3821	00 49 06.29 +57 48 54.7	00 49 06.51 +57 48 54.3	1.8
3909	00 50 07.59 -10 38 39.6	00 50 07.60 -10 38 40.8	1.2
4148	00 53 01.14 -30 21 24.9	00 53 01.33 -30 21 27.7	3.7
7513	01 36 47.84 +41 24 19.7	01 36 47.76 +41 24 19.4	0.9
7978	01 42 29.32 -53 44 27.0	01 42 29.52 -53 44 26.2	1.9
8768	01 52 49.17 -22 26 05.5	01 52 49.23 -22 26 06.7	1.5
10138	02 10 25.93 -50 49 25.4	02 10 26.00 -50 49 25.0	0.8
10798	02 18 58.50 -25 56 44.5	02 18 58.48 -25 56 41.7	2.8
11452	02 27 45.86 +04 25 55.7	02 27 45.85 +04 25 54.7	1.0
11964	02 34 22.57 -43 47 46.9	02 34 22.48 -43 47 44.6	2.5
12777	02 44 11.99 +49 13 42.4	02 44 12.05 +49 13 45.1	2.8
13402	02 52 32.13 -12 46 11.0	02 52 32.18 -12 46 10.2	1.1
14954	03 12 46.44 -01 11 46.0	03 12 46.44 -01 11 50.1	4.1
15330	03 17 46.16 -62 34 31.2	03 17 45.79 -62 34 29.3	3.2
15371	03 18 12.82 -62 30 22.9	03 18 13.12 -62 30 24.4	2.6
15799	03 23 35.26 -40 04 35.0	03 23 35.31 -40 04 35.4	0.7
16134	03 27 52.41 -19 48 16.1	03 27 52.31 -19 48 17.8	2.2
17420	03 43 55.34 -19 06 39.2	03 43 55.40 -19 06 39.6	0.9
17439	03 44 09.17 -38 16 54.4	03 44 09.26 -38 16 54.6	1.1
19849	04 15 16.32 -07 39 10.3	04 15 16.21 -07 39 11.1	1.8
19884	04 15 56.90 -53 18 35.3	04 15 57.00 -53 18 35.7	1.0
22263	04 47 36.29 -16 56 04.0	04 47 36.42 -16 56 04.9	2.1
23311	05 00 49.00 -05 45 13.2	05 00 48.73 -05 45 13.7	4.1
25110	05 22 33.53 +79 13 52.1	05 22 34.22 79 13 52.2	1.9
27887	05 54 04.24 -60 01 24.5	05 54 03.72 -60 01 24.0	3.9
28103	05 56 24.29 -14 10 03.7	05 56 24.31 -14 10 01.7	2.0
28442	06 00 19.52 -31 01 43.4	06 00 19.40 -31 01 53.8	10.5
29271	06 10 14.47 -74 45 11.0	06 10 14.53 -74 45 11.1	0.3
29568	06 13 45.29 -23 51 43.0	06 13 45.38 -23 51 40.2	3.1
32439	06 46 14.15 +79 33 53.3	06 46 14.44 +79 33 51.0	2.4
32480	06 46 44.34 +43 34 38.7	06 46 44.23 +43 34 38.8	1.2
33277	06 55 18.67 +25 22 32.5	06 55 18.68 +25 22 32.7	0.2
34017	07 03 30.46 +29 20 13.5	07 03 30.49 +29 20 15.6	2.1
34065	07 03 57.32 -43 36 28.9	07 03 56.77 -43 36 28.4	6.0
35136	07 15 50.14 +47 14 23.9	07 15 50.18 +47 14 24.5	0.7
36439	07 29 55.96 +49 40 20.9	07 29 55.88 +49 40 19.6	1.5
38382	07 51 46.30 -13 53 52.9	07 51 46.30 -13 53 54.9	2.0
38784	07 56 17.23 +80 15 56.0	07 56 17.50 +80 15 56.4	0.8
40693	08 18 23.95 -12 37 55.8	08 18 24.10 -12 37 57.9	3.0
40843	08 20 03.86 +27 13 03.8	08 20 03.88 +27 12 56.6	7.1
42430	08 39 07.90 -22 39 42.8	08 39 08.10 -22 39 45.3	3.7
42438	08 39 11.70 +65 01 15.3	08 39 11.74 +65 01 15.3	0.3
43587	08 52 35.81 +28 19 50.9	08 52 35.89 +28 19 52.0	1.5
43726	08 54 17.95 -05 26 04.1	08 54 17.91 -05 26 04.3	0.6
44897	09 08 51.07 +33 52 56.0	09 08 50.84 +33 52 55.7	2.9
45333	09 14 20.54 +61 25 23.9	09 14 20.92 +61 25 22.8	2.9
45617	09 17 53.46 +28 33 37.9	09 17 53.35 +28 33 38.6	1.6
46580	09 29 54.82 +05 39 18.5	09 29 54.82 +05 39 19.9	1.4
47592	09 42 14.42 -23 54 56.0	09 42 14.26 -23 54 54.8	2.5
49081	10 01 00.66 +31 55 25.2	10 01 00.68 +31 55 23.7	1.5
49908	10 11 22.14 +49 27 15.3	10 11 21.87 +49 27 17.2	3.2
51459	10 30 37.58 +55 58 49.9	10 30 37.24 +55 58 50.9	3.0
51502	10 31 04.66 +82 33 30.9	10 31 05.98 +82 33 32.5	3.0
53721	10 59 27.97 +40 25 48.9	10 59 28.01 +40 25 48.9	0.5
54646	11 11 05.17 +30 26 45.7	11 11 05.58 +30 26 47.6	5.6

Continued...

Table 10. Continued.

HIP	ICRS(2000)	PACS100	Offset
56452	11 34 29.49 -32 49 52.8	11 34 29.45 -32 49 55.1	2.4
57507	11 47 15.81 -30 17 11.4	11 47 16.04 -30 17 11.2	3.0
57939	11 52 58.77 +37 43 07.2	11 52 58.36 +37 43 08.9	5.2
58345	11 57 56.21 -27 42 25.4	11 57 56.37 -27 42 24.2	2.4
62145	12 44 14.55 +51 45 33.5	12 44 14.46 +51 45 34.1	1.0
62207	12 44 59.41 +39 16 44.1	12 44 59.33 +39 16 44.3	1.0
62523	12 48 47.05 +24 50 24.8	12 48 47.17 +24 50 26.2	2.2
64792	13 16 46.52 +09 25 27.0	13 16 46.63 +09 25 28.6	2.3
64797	13 16 51.05 +17 01 01.9	13 16 51.11 +17 01 02.5	1.0
65026	13 19 45.66 +47 46 40.9	13 19 45.66 +47 46 38.3	2.6
65721	13 28 25.81 +13 46 43.6	13 28 25.72 +13 46 45.3	2.1
67275	13 47 15.74 +17 27 24.9	13 47 15.95 +17 27 24.2	3.1
67422	13 49 04.00 +26 58 47.7	13 49 04.07 +26 58 45.9	2.0
67620	13 51 20.33 -24 23 25.3	13 51 20.10 -24 23 22.8	4.0
68184	13 57 32.06 +61 29 34.3	13 57 32.19 +61 29 33.7	1.1
68682	14 03 32.35 +10 47 12.4	14 03 32.37 +10 47 12.3	0.3
69965	14 19 00.90 -25 48 55.5	14 19 00.88 -25 48 56.1	0.7
70319	14 23 15.28 +01 14 29.6	14 23 15.29 +01 14 31.5	1.9
70857	14 29 22.30 +80 48 35.5	14 29 23.25 +80 48 33.6	3.0
71181	14 33 28.87 +52 54 31.6	14 33 28.81 +52 54 32.9	1.4
71681	14 39 35.08 -60 50 13.8	14 39 35.54 -60 50 09.7	5.3
71683	14 39 36.50 -60 50 02.3	14 39 36.05 -60 50 04.9	4.2
71908	14 42 30.42 -64 58 30.5	14 42 30.22 -64 58 27.3	3.4
72567	14 50 15.81 +23 54 42.6	14 50 15.79 +23 54 44.4	1.8
72603	14 50 41.18 -15 50 50.1	14 50 41.06 -15 50 49.9	1.7
72848	14 53 23.77 +19 09 10.1	14 53 23.94 +19 09 09.0	2.6
73100	14 56 23.04 +49 37 42.4	14 56 23.14 +49 37 42.0	1.1
73182	14 57 26.54 -21 24 41.5	14 57 26.42 -21 24 37.0	4.8
73184	14 57 28.00 -21 24 55.7	14 57 27.86 -21 24 53.0	3.3
73996	15 07 18.07 +24 52 09.1	15 07 18.20 +24 52 10.3	2.1
77052	15 44 01.82 +02 30 54.6	15 44 01.98 +02 30 54.8	2.4
78459	16 01 02.66 +33 18 12.6	16 01 02.60 +33 18 14.3	1.9
78775	16 04 56.79 +39 09 23.4	16 04 56.75 +39 09 22.0	1.5
79248	16 10 24.31 +43 49 03.5	16 10 24.34 +43 49 03.8	0.4
80725	16 28 52.67 +18 24 50.6	16 28 52.58 +18 24 47.6	3.3
82860	16 56 01.69 +65 08 05.3	16 56 02.03 +65 08 07.6	3.1
83389	17 02 36.41 +47 04 54.8	17 02 36.38 +47 04 55.3	0.6
84862	17 20 39.57 +32 28 03.9	17 20 39.42 +32 28 04.1	1.9
85235	17 25 00.10 +67 18 24.1	17 25 00.20 +67 18 26.0	2.0
85295	17 25 45.23 +02 06 41.1	17 25 45.23 +02 06 41.5	0.4
86036	17 34 59.59 +61 52 28.4	17 34 59.30 +61 52 28.5	2.1
86796	17 44 08.70 -51 50 02.6	17 44 08.66 -51 50 01.9	0.8
88601	18 05 27.29 +02 30 00.4	18 05 27.27 +02 29 59.4	1.0
88972	18 09 37.42 +38 27 28.0	18 09 37.36 +38 27 27.4	0.9
89042	18 10 26.16 -62 00 07.9	18 10 26.10 -62 00 08.5	0.7
91009	18 33 55.77 +51 43 08.9	18 33 55.87 +51 43 09.3	1.0
92043	18 45 39.73 +20 32 46.7	18 45 39.62 +20 32 48.3	2.2
95995	19 31 07.97 +58 35 09.6	19 31 07.92 +58 35 12.2	2.6
96100	19 32 21.59 +69 39 40.2	19 32 21.01 +69 39 40.2	3.0
96441	19 36 26.53 +50 13 16.0	19 36 26.58 +50 13 16.4	0.6
97944	19 54 17.75 -23 56 27.9	19 54 17.96 -23 56 27.5	2.9
98959	20 05 32.76 -67 19 15.2	20 05 32.60 -67 19 16.5	1.6
99240	20 08 43.61 -66 10 55.4	20 08 43.53 -66 10 58.1	2.7
99461	20 11 11.94 -36 06 04.4	20 11 12.28 -36 06 03.5	4.2
101955	20 39 37.71 +04 58 19.3	20 39 37.69 +04 58 20.1	0.9
101997	20 40 11.76 -23 46 25.9	20 40 11.53 -23 46 24.9	3.3
103389	20 56 47.33 -26 17 47.0	20 56 47.46 -26 17 45.5	2.3
104214	21 06 53.94 +38 44 57.9	21 06 54.11 +38 44 58.2	2.0
104217	21 06 55.26 +38 44 31.4	21 06 55.44 +38 44 31.5	2.1
105312	21 19 45.62 -26 21 10.4	21 19 45.52 -26 21 07.1	3.6
106696	21 36 41.24 -50 50 43.4	21 36 41.41 -50 50 43.5	1.6

Continued...

Table 10. Continued.

HIP	ICRS(2000)	PACS100	Offset
107350	21 44 31.33 +14 46 19.0	21 44 31.27 +14 46 19.4	1.0
107649	21 48 15.75 -47 18 13.0	21 48 15.88 -47 18 11.4	2.1
108870	22 03 21.66 -56 47 09.5	22 03 21.72 -56 47 09.9	0.6
109378	22 09 29.87 -07 32 55.2	22 09 30.07 -07 32 54.1	3.2
109422	22 10 08.78 -32 32 54.3	22 10 08.87 -32 32 53.3	1.5
110109	22 18 15.62 -53 37 37.5	22 18 15.94 -53 37 35.8	3.3
113357	22 57 27.98 +20 46 07.8	22 57 28.27 +20 46 05.4	4.7
113576	23 00 16.12 -22 31 27.6	23 00 16.21 -22 31 26.8	1.5
114948	23 16 57.69 -62 00 04.3	23 16 57.44 -62 00 05.8	2.3
116745	23 39 37.39 -72 43 19.8	23 39 37.23 -72 43 19.5	0.8
120005	09 14 24.70 +52 41 11.0	09 14 24.64 +52 41 11.5	0.7

Table 12. Continued.

HIP	SpT	PACS70 (mJy)	S70 (mJy)	χ_{70}	PACS100 (mJy)	S100 (mJy)	χ_{100}	PACS160 (mJy)	S160 (mJy)	χ_{160}	L_d/L_\star	MIPS70 (mJy)
101955	K5V	9.22 ± 2.68	12.00 ± 0.17	-1.03	5.79 ± 0.87	5.88 ± 0.08	-0.10	<5.4	2.30 ± 0.03		4.4e-06	11.50 ± 7.043
101997	G8/K0V	10.41 ± 1.66	11.62 ± 0.28	-0.72	5.59 ± 0.95	5.69 ± 0.14	-0.10	<4.2	2.22 ± 0.05		2.3e-06	7.40 ± 3.73
104214	K5V		101.17 ± 2.17		48.31 ± 2.68	49.57 ± 1.06	-0.44	21.63 ± 3.70	19.36 ± 0.42	0.61	1.4e-06	64.20 ± 12.66
104217	K7V		83.70 ± 4.38		38.62 ± 2.43	41.01 ± 2.15	-0.74	18.16 ± 3.81	16.02 ± 0.84	0.55	2.0e-06	83.30 ± 13.15
106696	K2V	10.59 ± 1.93	8.35 ± 0.14	1.16	3.81 ± 0.79	4.09 ± 0.07	-0.35	5.55 ± 1.70	1.60 ± 0.03	2.33	3.2e-06	19.20 ± 5.26
108870	K5V		125.77 ± 2.91		58.92 ± 1.75	61.63 ± 1.42	-1.20	23.42 ± 1.95	24.07 ± 0.56	-0.32	6.2e-07	111.3 ± 9.47
109422	F6V		24.01 ± 0.72		10.57 ± 1.80	11.77 ± 0.35	-0.65	<8.4	4.60 ± 0.14		1.3e-06	10.60 ± 5.65
110109	G1V		24.71 ± 0.83		10.14 ± 1.55	12.11 ± 0.41	-1.23	<8.4	4.73 ± 0.16		1.4e-06	28.10 ± 5.72
113357	G5V		21.88 ± 0.24		11.49 ± 2.67	10.72 ± 0.12	0.29	<15.0	4.19 ± 0.05		2.8e-06	28.10 ± 4.88
116745	K3V		12.22 ± 0.23		5.21 ± 0.86	5.99 ± 0.11	-0.90	<4.2	2.34 ± 0.04		2.9e-06	17.20 ± 2.46
120005	K2		27.63 ± 0.48		11.20 ± 1.19	13.54 ± 0.24	-1.93	5.05 ± 1.76	5.29 ± 0.09	-0.14	3.5e-06	21.30 ± 2.71